January 2018

The Impact Of Stellar Convection Criteria On Population Iii Supernovae Nucleosynthesis

Jacob Teffs

THE IMPACT OF STELLAR CONVECTION CRITERIA ON POPULATION III
SUPERNOVAE NUCLEOSYNTHESIS

by

Jacob Joseph Teffs

Bachelor of Science, University of Central Arkansas, 2012

A Dissertation

Submitted to the Graduate Faculty

of the

University of North Dakota

in partial fulfillment of the requirements
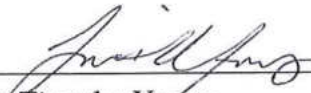

for the degree of

Doctor of Philosophy

Grand Forks, North Dakota

August

2018

This dissertation, submitted by Jacob Teffs in partial fulfillment of the requirements for the Degree of Doctor of Philosophy from the University of North Dakota, has been read by the Faculty Advisory Committee under whom the work has been done and is hereby approved.

_____
Dr. Timothy Young

_____
Dr. Graeme Dewar

_____
Dr. Kanishka Marasinghe

_____
Dr. Wayne Barkhouse

_____
Dr. Travis Desell

This dissertation is being submitted by the appointed advisory committee as having met all of the requirements of the School of Graduate Studies at the University of North Dakota and is hereby approved.

_____
Dr. Grant McGimpsey
Dean of the School of Graduate Studies

_____
July 11, 2018
Date

ii

PERMISSION

Title   The Impact of Stellar Convection Criteria on Population III Supernovae
                  Nucleosynthesis

Department   Physics and Astrophysics

Degree   Doctor of Philosophy

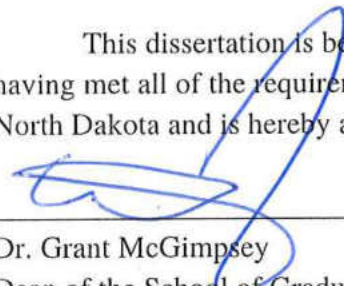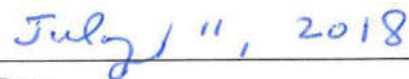   In presenting this dissertation in partial fulfillment of the requirements for a
graduate degree from the University of North Dakota, I agree that the library of this
University shall make it freely available for inspection. I further agree that permission
for extensive copying for scholarly purposes may be granted by the professor who
supervised my dissertation work or, in their absence, by the chairperson of the
department or the dean of the School of Graduate Studies. It is understood that any
copying or publication or other use of this dissertation or part thereof for financial gain
shall not be allowed without my written permission. It is also understood that due
recognition shall be given to me and to the University of North Dakota in any scholarly
use which may be made of any material in my dissertation.

                                                        Jacob Teffs
                                                        06/25/2018

TABLE OF CONTENTS

LIST OF FIGURES

x

ACKNOWLEDGMENTS

This dissertation would not be possible without the help and support of numerous people. I would like to express my gratitude to my adviser, Dr. Tim Young, who was always available to discuss my research and provided invaluable guidance. My thanks to my committee members: Dr. Wayne Barkhouse, Dr. Kanishka Marasinghe, Dr. Graeme Dewar, and Dr. Travis Desell, for their advice and comments.

My undergraduate research advisor, Dr. Debra Burris, was integral in my early years as an astronomer. Without her guidance, support, and care, I would not have continued on to graduate school.

I am forever grateful to my parents whom have supported me throughout my time here at UND.

Thank you Madina Sultanova, for without her reminding me of so many deadlines, I would not have been able to graduate.

To my parents, Jeff and Susan Teffs,
who have always supported me.

ABSTRACT

Population III stars are the first stars formed after the Big Bang, comprised of primarily

hydrogen and helium and lack heavy elements from previous generations. Using the

one-dimensional radiation-hydrodynamics code BOOM, a grid of eighteen stellar models

with masses of 15-80 $M_\odot$, are exploded under a low and high explosion energy criteria.

Three types of central compact remnants are considered. The 3208 isotope TORCH nuclear

reaction network is used to calculate the nucleosynthesis that occurs during the

supernovae. The two convection criteria, Ledoux and Scharzschild, produce vastly

different stellar structures and thus produce different nucleosynthetic trends. When

comparing the numerically calculated abundances to observed extremely metal poor stars

($[Fe/H] < -3$), it is found that even using abundances from both the Schwarzschild and

Ledoux convection model a fit was not possible. The overall Ni-56 production claculated

for a given distribution and the peak production of Ni-56 is compared to observationally

calculated values from Population II supernovae. We show that for high energy

Schwarzschild models, integrated over a Salpeter initial mass function, the yields

approach that of the more compact lower energy Ledoux series, but heavier elemental

abundances of these metal poor stars need to be observed and determined to better fit the

data. The produced nickel for both series is high compared to observational work and is

likely to be lessened for larger central remnants.

CHAPTER 1

INTRODUCTION

After the Big Bang, the universe was primarily composed of hydrogen, some helium, and

trace amounts of lithium (Harwit & Spaans, 2003). It is assumed that the first stars were

formed from these primordial elements and with no heavy elements from previous

generations of stars, the formation environment was significantly different from those

present in our current universe (Bromm, 2013; Ferrara, 1998; Ciardi et al., 2000). These

first stars are called population III stars, and to date none have been detected. Population

II, currently the oldest observed stars, are metal poor as seen in their spectra and are

usually found in the nuclear bulge of spiral galaxies, the halos of spiral galaxies, and

throughout elliptical galaxies. Population I stars have the highest amounts of metals in

their spectra and are found in the disks of galaxies and in star forming regions. Thus the

sequence of populations of stars are in reverse chronological order, population III are the

oldest while Population I are the youngest.

Due to the different environments and no direct observations, the distribution of

population III initial stellar masses is unsure. Simulations have shown a wide spread in

possible formation mass distributions called the initial mass functions (IMFs). The IMF is

a distribution function which defines the number of forming stars as a function of mass.

These simulations suggest IMFS that range from a single peak near 100 $M_\odot$ or double

peaked around M < 1 $M_\odot$ and M > 100 $M_\odot$ (Nakamura & Umemura, 2001; Norman,

2008; Stacy et al., 2016).

While direct detection is not currently feasible, new telescopes such as the James Webb Space Telescope (JWST) may have the ability to detect the supernovae of population III stars (Lawlor et al., 2015). Supernova are the explosions of stars heavier than 8 $M_\odot$ that can outshine not only their progenitor star but their host galaxy. Thus population III supernovae give the best chances of deducing the existence of population III stars.

Measurements of our own Sun and solar system meteorites show elemental abundances ranging large amounts of abundant hydrogen and helium to the trace amounts of heavy elements such as uranium and thorium. The creation of elements heavier than hydrogen and helium is found primarily in stars. Stellar interiors are hot and dense, creating the conditions for nuclear fusion. As stars age and use up all their fuel in the stellar core, the inward pressure due to gravity overwhelms the outward energy from fusion in the core, and the whole star collapses. The collapse transforms the gravitational potential energy of the core through complex interactions between neutrinos and anti-neutrinos and can deposit this energy into the infalling material. This rapid absorption of energy creates an outward moving shock wave that ejects the stellar material, creating a supernova.

1.1   The First Stars

With no direct observations, information about these first stars comes from extrapolating information from current populations and simulations of stellar formation. One must assume that population III stars from according to the current theory of star formation (Clayton, 1968), which states that a critical mass of hydrogen gas collapses towards a

central point due to gravity, increases in temperature and ignites hydrogen fusion at the core. Stellar evolution of this metal free material is a subject of many studies (Ohkubo et al., 2009; Bromm, 2013; Stacy & Bromm, 2014).

Stellar evolution of Population III stars is done using 1-,2-, or 3- dimensional computer simulations. The 1-D and 2-D calculations follow a single star from initial formation to the end of all fusion in the core. There exists numerous codes that can do this such as `MESA` (Paxton et al., 2011), `BRAHMA` (Lawlor & MacDonald, 2006), and `KEPLER` (Weaver et al., 2017). The common usage of 1-D codes is due to the large range of time and space scaling, which is simpler under the spherically symmetric assumptions, but this neglects rigorous treatments of higher-dimensional physics. Approximations of higher dimensional effects, such as rotation, turbulent flow, and magnetic field, are often used and are currently being implemented in the open souce code `MESA`.

Instead of stellar evolution, 3-D codes often focus on stellar formation and the hydrodynamic environments in which these stars form. Some groups (Viallet, M. et al., 2011) work towards getting a fully 3-D stellar evolution code but the computational cost is still high. Other groups, such as Hopkins & Conroy (2017), Schneider et al. (2003), Omukai et al. (2005), and Chiaki et al. (2014), focus more on the initial growth and formation of stars by the fragmentation of large 3-D gas clouds. The usual method is to treat the formation of stars as gravitational sinks (Hubber et al., 2013), or effectively remove them from the simulation by preventing the formation of internal structure or physical processes to occur. By starting with an initial cloud mass and including any physical process they may be important in the early universe, such as radiation or metal free opacities, the simulations and statistics can be used to determine the initial properties

over a set of zero age main sequence mass stars. The zero age main sequence (ZAMS) defines the time in which the star begins to fuse hydrogen in the stellar core and joins the main sequence in the Hertzsprung-Russel Diagram (Carroll & Ostlie, 2007).

If observations of population III supernovae are detected, it may be possible to infer some information, such as radius or mass from the pre-supernova star by comparing to simulations of supernovae. Because the exact progenitors are unknown it is important to explore various types of population III stars to include all possible scenarios.

1.2 Supernovae

The study of supernovae has rapidly advanced since ancient observers first saw a 'guest star' in 185 AD (Stothers, 1977). Several supernovae were likely observed and recorded throughout history, but the first supernovae discovered in 1987, called SN1987a, is arguably one of the most famous due to its proximity in the Large Magellanic Cloud, number of observations, and unique progenitor. (Blinnikov et al., 2000; Arnett et al., 1989; Arnett & Fu, 1989) Radiation from supernovae are observed from radio to gamma waves due to the high energy and wide range of structure changes changing from a compact star to a large diffuse supernovae remnant. (Hughes et al., 2006; Arnett et al., 1989). Since the launch of automated transient telescope satellites, such as the GAIA telescope (Gaia Collaboration et al., 2016), the number of observed SNe has reached the thousands per year, though often with little long-term follow up in the optical or other wavelengths. This has produced an observational data problem (Zhang & Zhao, 2015) due to the quantity of unanalyzed data or lack of repeat observations.

Supernovae can fall broadly into two classes, Type I and Type II, as defined by their spectra as shown in figure 1. The focus of this work will be core collapse supernovae

with hydrogen in their spectra called Type II supernovae. Core collapse supernovae, or CCSNe, require stars with masses greater than 8 $M_\odot$ at ZAMS. The higher mass allows the stellar core to undergo nuclear fusion up to iron, but beyond iron is an endothermic process and prevents further quiescent element nucleosynthesis. At collapse, the gas pressure de to the fusion process, normally sufficient to balance the gravitational force inward, ceases and causes the central core to collapse. The exact physics of this collapse is still a focus of active research (Mezzacappa & Messer, 1999),(Dessart, Luc & Audit, Edouard, 2018). The collapse happens on time scales of milliseconds starting with the iron core contracting rapidly and the layers above the core, in shells made of C/O, He, and H begin to fall towards the iron core. The rapid contraction causes the iron to photodissassociate and releases energy mostly in the form of neutrinos(Janka, 2017). The interaction probability of neutrinos is low for normal matter, but the infalling material is dense and the neutrino flux is high so that the rate of probability increases and the neutrinos begin to produce anti-neutrinos upon interaction. The neutrino-antineutrino pairs have a probability to annihilate within the infalling layers, redepositing the energy into the matter. If this release of energy is great enough, a shock front will be formed unbinding the outer layers from the core, creating a supernova. If not, the star continues to collapse and can directly form a black hole. The remaining material that is not ejected in the supernovae can form a neutron star or black hole and is called a compact remnant. As the shock traverses in the interior of the star, two important features are present: the shock is hot and dense with an average temperature approaching 10 billion K and a density approximately 4 times the initial density of 100 billion g/cm^3. These features are important for explosive nucleosynthesis, the production of new elements as the high
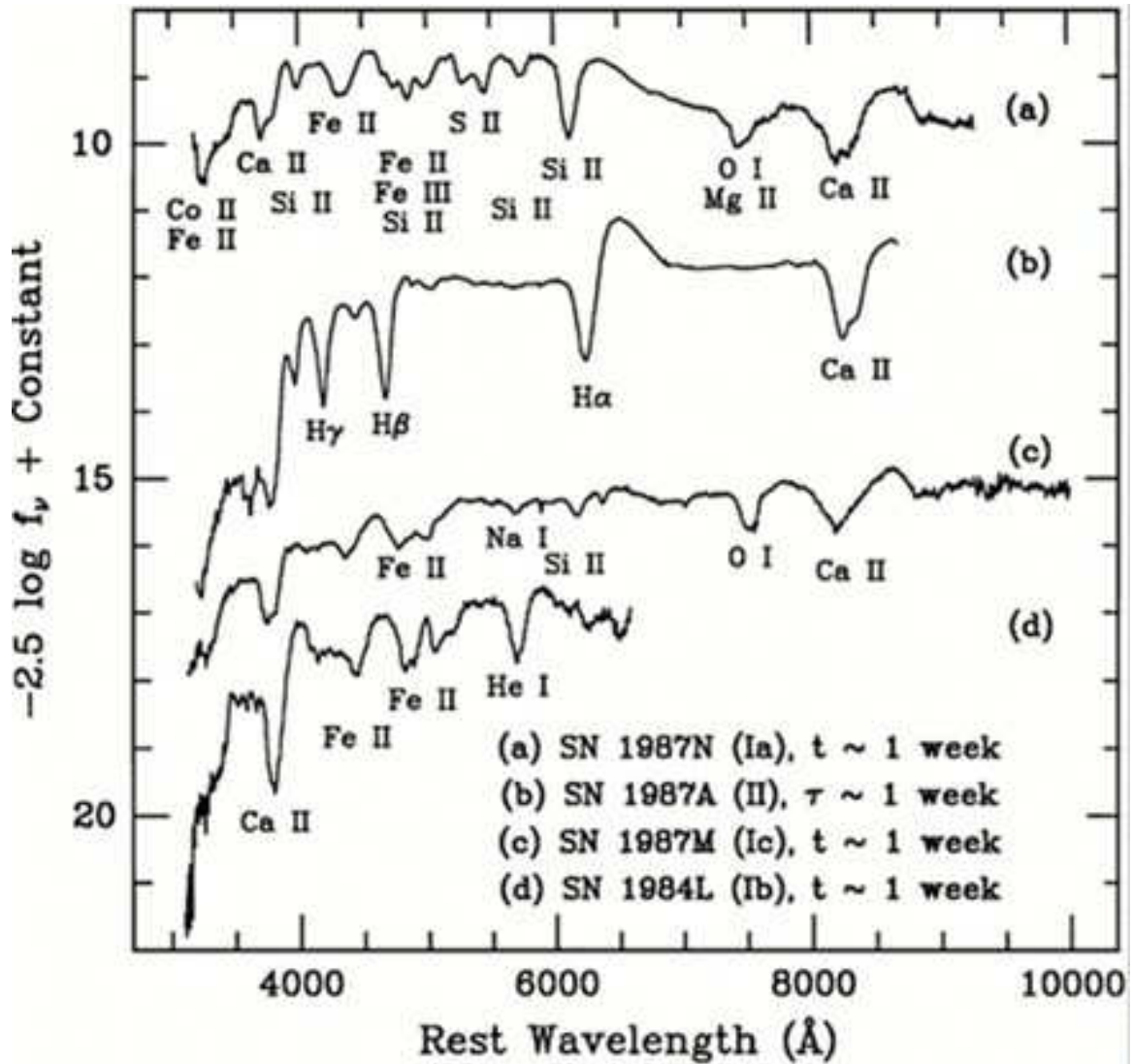
Figure 1. The spectra of each supernovae class changes due to the nature of the progenitor star, such as the presence a hydrogen line ($H\alpha$) and the subsequent lack of that line for the other three. Figure taken from Filippenko (1997)

energy shock propagates through the stellar material. The shock carries with it a high flux of neutrons that are heated to a high temperature, making ideal conditions for rapid neutron capture.

1.3 Nucleosynthesis

Nucleosynthesis occurs in two stellar environments; controlled fusion in stellar evolution and uncontrolled fusion in supernova shock waves. During stellar evolution, the star is in

hydrodynamic equilibrium and the energy generation in its core is in a form of controlled fusion. These fusion processes play an important role in the stars evolution, influencing the temperature and radius and thus taking various evolutionary tracks on the H-R diagram. Stars initially form from enough hydrogen mass to create the densities and temperatures in the core needed to initiate hydrogen burning under the PP-chain. For stars heavier than 1 $M_\odot$, these stars will eventually fuse helium and onward. These fusion processes generate energy dependent on the initial mass of the star, less massive stars do not need to produce as much energy as massive stars due to less gravity to withstand. For massive stars heavier than around 8 $M_\odot$, the stars fuse C, O, and Si, leaving an inert iron core. Nucleosynthesis in stellar evolution can account for elementals up to iron, but does not produce elements with Z > 26. Above Z > 26 is where the neutron capture processes become important and requires energetic events such as neutron star collisions or supernovae.

Two main neutron capture processes can account for heavy elements observed in the universe. These are the rapid and slow processes. The slow process includes capturing neutrons at a rate comparable to the decay of the neutron itself. Elements formed by this s-process tend to follow the line of stability as shown in figure 2. The rapid neutron capture process requires a high flux of neutrons at a rate much shorter then the decay rate of a free neutron, which has a mean lifetime of 881.5 ± 1.5 s (Carroll & Ostlie, 2007). As seen in figure 2, this allows the r-process to reach a different range of elements. Environments that have a high flux of neutrons include supernovae, both core collapse and type Ia, and mergers of neutron stars. Recent observations of neutron star mergers (Thielemann et al., 2017) confirm this to be an important site of r-process nucleosynthesis.

The likelihood of merger events, estimated at $R_{local} \approx 600^{+600}_{300} Gpc^3 yr^1$ by Chruslinska et al. (2018) in the local universe, may prove more important than the likelihood of population III SNe, but could depend on the IMF.
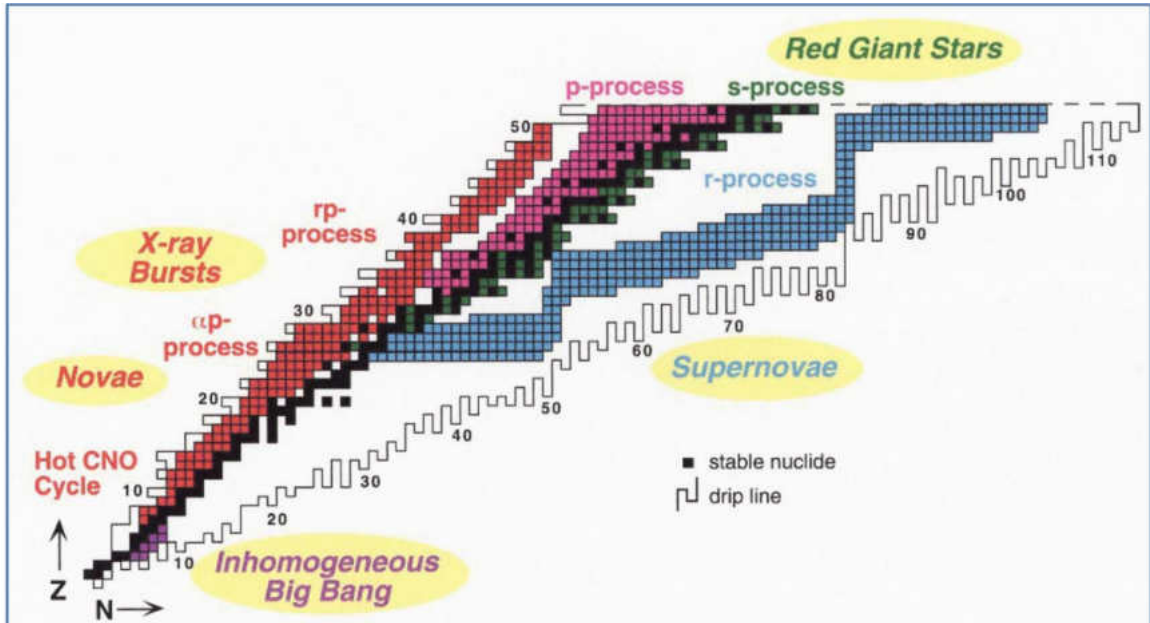
Figure 2. The sources of nucleosynthesis plotted on the Chart of the Nucleides. For the purpose of this work, primarily only the Neutron Drip line near the "Supernovae" section is of primary importance. The black points represent stable nuclei and follow an approximate 'Line of Stability.' Figure taken from Smith & Rehm (2001)

1.4 Motivation

Three important simulation outcomes can be calculated and cataloged and later compared to observations;Hertzsprung-Russel diagram evolution properties of Population III stars, the observable properties of their CCSNe explosions, and their nucleosynthesis. By first assuming some initial conditions for a population III star, it can be numerically evolved to the point of core collapse, after which the star can be numerically exploded. As the supernovae evolves, observational quantities can be calculated like the light cure or nucleosynthetic yields and compared to future detections of population III supernovae. A

large scale nuclear reaction network is used to calculate the explosive nucleosynthesis. By quantifying the yields of these population III supernovae, the results can be compared to the observed values in metal poor population II stars, or stars that were likely to have been contaminated by possibly only one or two previous generations of stars.

By assuming the distribution of stars matches an IMF, or initial mass function, the net yields over the entire mass range can be studied. The mass of the star and its subsequent evolution determines the outcome of the presupernova star, such as a large silicon or oxygen core, relative to the stars size. Abundance yields calculated from the nucleosynthesis can be compared to observed single-element trends for large groups of models or for a set of observed abundances of metal poor population II stars.

Multiple research groups have studied the explosive nucleosynthesis of population III stars in supernovae (Bessell et al., 2015; Tominaga et al., 2007). What makes this current work unique is the implementation of two different convection criteria in the stellar evolution. Two types of convection criteria gives rise to two unique sets of stars. These represent two evolutionary end points for pre-supernovae candidates.

1.5   Outline

In Chapter 2, I will discuss the codes and primary methods used to simulate the stellar evolution, the supernova explosions, and the nucleosynthesis. In Chapter 3, I will present the bulk of the data and the preliminary analysis. In Chapter 4, I will analyze the data further, calculating observables and expanding the nucleosynthesis data. In Chapter 5, I will summarize the results and make my concluding remarks. In chapter 6, I will discuss future work with the models and data.

CHAPTER 2

Methods

2.1   Stellar Evolution

The stellar models used in this project were numerically evolved by our collaborator Dr.

Tim Lawlor using BRAHMA (Lawlor & MacDonald, 2006). BRAHMA is a one dimensional

stellar evolution code based on an older Eggleton Code (Eggleton, 1971). A brief

discussion of the code is given below.

The code uses the standard set of stellar evolution equations as shown below

$$V \equiv \frac{1}{\rho} = 4\pi r^2 \frac{\partial r}{\partial m} \tag{2.1}$$

$$\frac{\partial E}{\partial t} = \varepsilon - \frac{\partial L}{\partial m} - P\frac{\partial V}{\partial t} \tag{2.2}$$

$$\frac{\partial u}{\partial t} = -G\frac{m}{r^2} - 4\pi r^2 \left(\frac{\partial P}{\partial m}\right) \tag{2.3}$$

$$\frac{\partial T}{\partial r} = -\frac{3}{4ac}\frac{\overline{\kappa}\rho}{T^3}\frac{L_{rad}}{4\pi r^2}(\text{radiation}) \tag{2.4}$$

$$\frac{\partial T}{\partial r} = -\left(1 - \frac{1}{\gamma}\right)\frac{\mu m_H}{k}\frac{GM_r}{r^2}(\text{adiabatic convection}) \tag{2.5}$$

These equations are, in order, conservation of mass, energy, momentum, and equations for

the transport of energy for radiation dominated regions and for convective dominated

regions. These are adapted to a staggered mesh (Kashiwa & Lee, 1991) that is evolved

using an adaptive mesh refinement routine as discussed in (Pretorius & Lehner, 2004).

10

Opacity, κ is treated by interpolation between the high and low temperature opacity tables given by OPAL (Iglesias & Rogers, 1996) and Alexander (Ferguson et al., 2005). The `BRAHMA` code also includes a nuclear reaction network that tracks the important fusion processes involved in stellar evolution (Timmes et al., 2000).

2.1.1   Convection

An important physical effect during the stellar evolution process is convection. Convection is a process in which macroscopic mass elements exchange energy between hotter and cooler layers. Higher temperature mass elements rise to cooler zones, depositing their excess energy, cool, and fall inward. This process may be inherently multi-dimensional, so approximations for the one-dimensional case must be used. The most common prescription in stellar evolution codes is mixing-length theory (Clayton, 1968). This theory relies on defining a free parameter called the mixing length l_m which measures the distance traveled by a convective mass element before releasing its energy in the surrounding gas. One caveat to this theory, is that it assumes hydrostatic-equilibrium, which implementing this in a stellar evolution code requires caution (Deng & Xiong, 2001). During slow burning phases, many regions of the star are likely in hydrostatic equilibrium, at least locally, but during rapid changes of structure and temperature as the star evolves from one burning phase to another, its unlikely that large regions are in hydrostatic equilibrium.

As derived in von Steinkirch (2012), a general form to determine convective stability is

$$\left(\frac{d \ln T}{d \ln P}\right)_s < \left(\frac{d \ln T}{d \ln P}\right)_e + \left(\frac{\varphi}{\delta}\frac{d \ln \mu}{d \ln P}\right)_s \tag{2.6}$$

where s and e represent the surroundings and the mass element respectively. φ and δ are defined as

$$\varphi = \left(\frac{\partial ln\rho}{\partial ln\mu}\right)_{P,T} \tag{2.7}$$

$$\delta = -\left(\frac{\partial ln\rho}{\partial lnT}\right)_{P,\mu} \tag{2.8}$$

which are the thermodynamic derivatives. μ is the chemical potential and P and T are the standard temperature and pressure terms.

This general form is defined as the Ledoux criteria for convective stability. For regions of the star in which there is no change in composition, the third term in 2.6 goes to zero and is defined as the Schwarzschild criteria for convective stability. For this work, one set of stars was evolved using only the Ledoux criteria of convection and another set was ran with only Schwarzschild criteria of convection.

The addition of the composition gradient in the Ledoux criterion maintains a stabilizing force that prevents the convective motion across these boundaries. Disallowing this stabilizing effect allows the composition zones to mix across larger regions inside the star. This extra energy convected from deeper in the star, causes the outer envelope shells to expand to a larger radius. Figure 3 shows the Hertzsprung-Russel diagram for the evolution of both series of stars. Once the models core begins to fuse hydrogen, the evolutions of similar mass models diverge due to the extra term in the Ledoux convection criteria.

2.2 Supernovae Simulation

To simulate core-collapse supernovae, the radiation hydrodynamics code BOOM is used. Details of the code can be found in Young (2004) and is based on an older Sutherland and
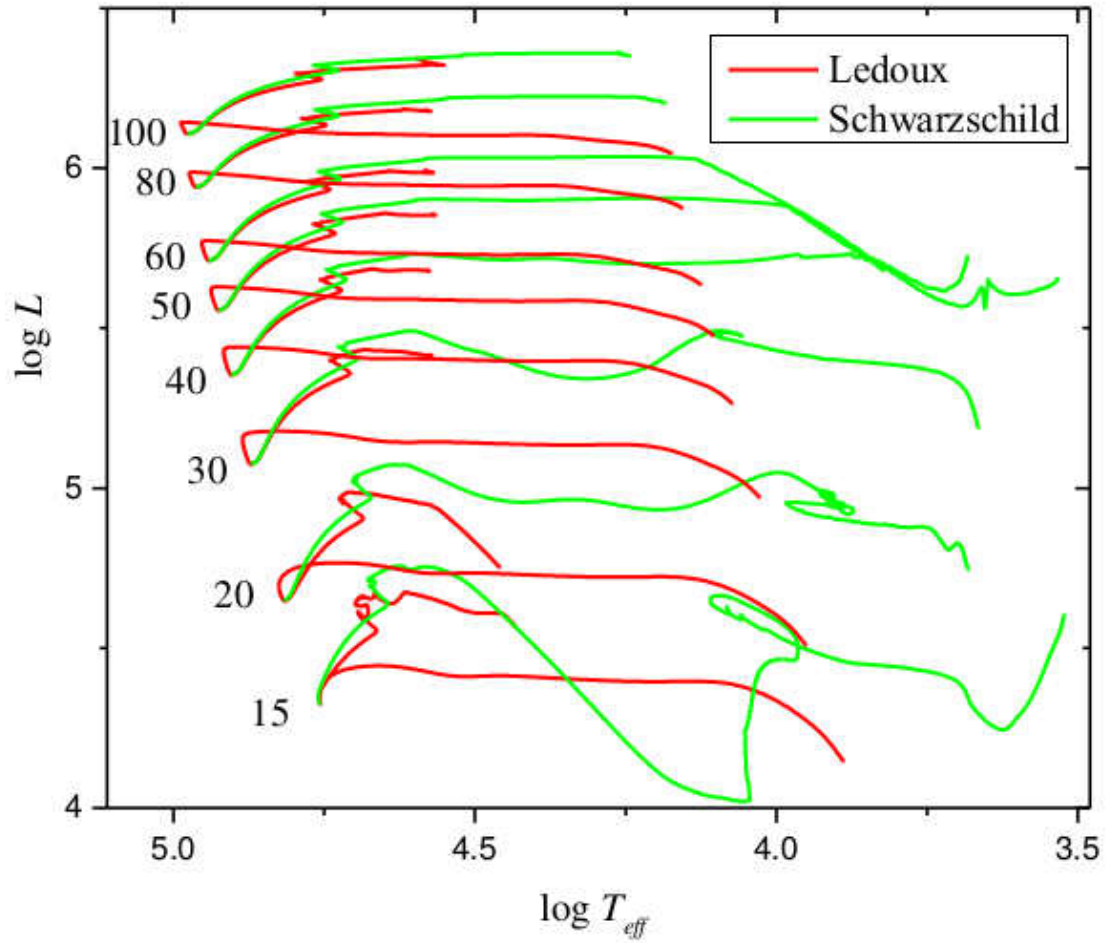
Figure 3. The Hertzsprung-Russel diagram for the stellar evolution of the Ledoux and Schwarzschild series of models. Both stars start on the right side of the lines due to both stars have the same initial conditions as the lines go from the right, or lower T_{eff} to higher before diverging on the left side.

Wheeler code (Sutherland & Wheeler, 1984). BOOM is a one-dimensional, spherically symmetric, flux limited, Lagrangian radiation hydrodynamics code. In a one-dimensional formalism, certain physical processes are neglected, such as turbulence, rotation, and magnetic fields, all of which can impact compositional and energy mixing (Radice et al., 2018). As these are largely higher dimensional effects, using approximations, such as boxcar mixing used by Kasen & Woosley (2009), add an extra free parameter and is not

focus of this work. Relativistic effects and neutrino physics are also not implemented.

Energy deposited by the radioactive decay of nickel is included, as a post-process energy

source that will be discussed later. Nucleosynthesis is calculated post-hydrodynamics and

assumes that the release of energy from the reactions are not significant enough to

influence the hydrodynamics.

2.2.1 Radiation Hydrodynamics

The equations of standard radiation hydrodynamics are as follows:

$$\frac{\partial r}{\partial t} = u \tag{2.9}$$

$$V \equiv \frac{1}{\rho} = 4\pi r^2 \frac{\partial r}{\partial m} \tag{2.10}$$

$$\frac{\partial u}{\partial t} = -G\frac{m}{r^2} - 4\pi r^2 \frac{\partial}{\partial m}(P + q) \tag{2.11}$$

$$\frac{\partial E}{\partial t} = \epsilon_{Ni} - \frac{\partial L}{\partial m} - (P + q)\frac{\partial V}{\partial t} \tag{2.12}$$

$$L = -(4\pi r^2)^2 \frac{\lambda ac}{3\kappa} \frac{\partial T^4}{\partial m} \tag{2.13}$$

These equations, in order, are the definition of velocity, conservation of mass, momentum,

and energy, and radiative luminosity. These equations are similar to the equations of

stellar structure with several differences. In particular, the luminosity due to convection

regions is negligible compared to that of radiative luminosity. This is due to the time

scales in which a supernova occurs compared to that of stellar evolution. In all numerical

hydrodynamic simulations an artificial viscosity term, q, is introduced to smooth out the

shock. The blast wave shock front is discontinuous, which can cause significant numerical

errors (Zel'dovich & Raizer, 2002) as the shock evolves. The artificial viscosity term q fixes this problem by spreading the discontinuity over several numerical zones (Caramana et al., 1998). In the absence of a shock, there is no discontinuity and the term disappears.

The radiation field in expanding material is complex because it needs to be calculated through a transition from regions of dense material to thin material. As the gas becomes optically thin, the rate of radiative flux diffusion can be overestimated under the grey atmosphere assumption. To limit this overestimation, λ, a flux limiter, is introduced. This term limits the radiative diffusion when the average photon path is on par with the flow length to a physically reasonable value (Mihalas, 1978). The role of the flux limiter, is to approximate the radiative flux from the diffusion regime to the free streaming regime.

2.2.2 Gamma Ray Deposition

The nuclear decay of $^{56}_{28}$Ni and $^{56}_{27}$Co is a primary energy source for Type Ia supernovae and powers the late time light curve of Type II supernova or in some cases the secondary peak in the light curve.

$$^{56}_{28}\text{Ni} \rightarrow ^{56}_{27}\text{Co} + e^+ + \nu_e + \gamma \tag{2.14}$$

$$^{56}_{27}\text{Co} \rightarrow ^{56}_{26}\text{Fe} + e^+ + \nu_e + \gamma \tag{2.15}$$
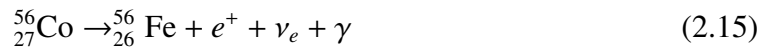
The mean life times of $^{56}_{28}$Ni and $^{56}_{27}$Co are 8.8 and 113.6 days respectively. As discussed, BOOM does not calculate nucleosynthesis or nuclear decay when calculating the hydrodynamics, but does include the nuclear heating in a second rerun calculation. The energy is produced from the $\gamma-$ray radiation from beta decays going from Ni to Co to Fe, described in equations 2.14 and 2.15.

To account for this energy deposition, a first run without nickel is calculated and

radius-density profiles are saved during the calculation. These profiles are used as input to an external code which calculates the energy deposited by the decay of $^{56}_{28}$Ni and $^{56}_{27}$Co. This code allows two variables that are important to the light curve analysis; the amount of nickel in the star and the radius to which this mass is uniformly mixed. This deposited gamma ray energy is included as an extra heating source in a second run of BOOM which influences the matter temperature and thus the opacity and the photospheres location in the expanding material.

To calculate the energy deposition by the decay of ^{56}Ni from first principles would require a complicated multi-group Monte Carlo calculation. This is in part because of the source location and deposited energy locations change throughout the expanding and inhomogeneous medium. The transfer of energy due to the $\gamma-$ ray is dependent on scattering angle and the line spectrum of the $\gamma-$ rays, which require wavelength dependent energies to be included (Mihalas & Mihalas, 1984). This type of calculation is complex and requires significant computing time. An approximation of this calculation is to treat the Monte Carlo scattering calculation as a geometric absorption calculation. This treatment is ideal in the later time light curve when the likelihood of single $\gamma-$ ray scattering twice is unlikely.

Combining the geometric aspects of the absorption and scattering and a constant source function s equals $d(a) \times s$, where $d(a)$ and s are defined as

$$d(a) = \frac{1}{2} \int_{-1}^{\mu_{max}} d\mu [e^{-\tau_{min}} - e^{-\tau_{max}}] \tag{2.16}$$

$$s = 3.9 \times 10^{10} e^{-t/\tau_{Ni}} + 6.78 \times 10^9 [e^{-t/\tau_{Co}} - e^{-t/\tau_{Ni}}] \tag{2.17}$$

where $\mu = cos\theta$ and τ_{min} and τ_{max} are the total optical depths to the near and far side of the radioactive core along the ray defined by the polar angle θ.

The $\gamma-$ rays have two roles; one is heating the dense material and contributing to an increased opacity and the second is when the material is less dense and adds to the late time luminosity, assuming the absorption is re-radiated into the optical.

$$L_{observed} = L_{photosphere} + \int_{m_{photo}}^{M} s_{dep}(m)dm \qquad (2.18)$$

2.3   Numerical Setup

2.3.1   Gridding

The pre-core collapse stellar model contributed by our collaborator is evolved using BRAHMA which uses an Eulerian grid. This gridding type defines fixed radius grid points where Lagrangian grids used fixed mass grid points. The stellar model from BRAHMA has variable mass zones so the model is regridded in equal mass zones for use in BOOM following the Lagrangian formulation. Spatial resolution is important (Couch & O'Connor, 2014), but too many zones can become computationally infeasible with respect to running time. The stellar model is initially divided into 400 zones. A central remnant is removed and the remaining zones are expanded into 600 even mass zones by methods of interpolation. Show below is a set of example regridded models compared to the original model.

In Figure 4, is tested with a different number of zones ranging from 100 to 1500 with run times as shown.

The overall structure of the lightcurve appears the similar regardless of zoning

17
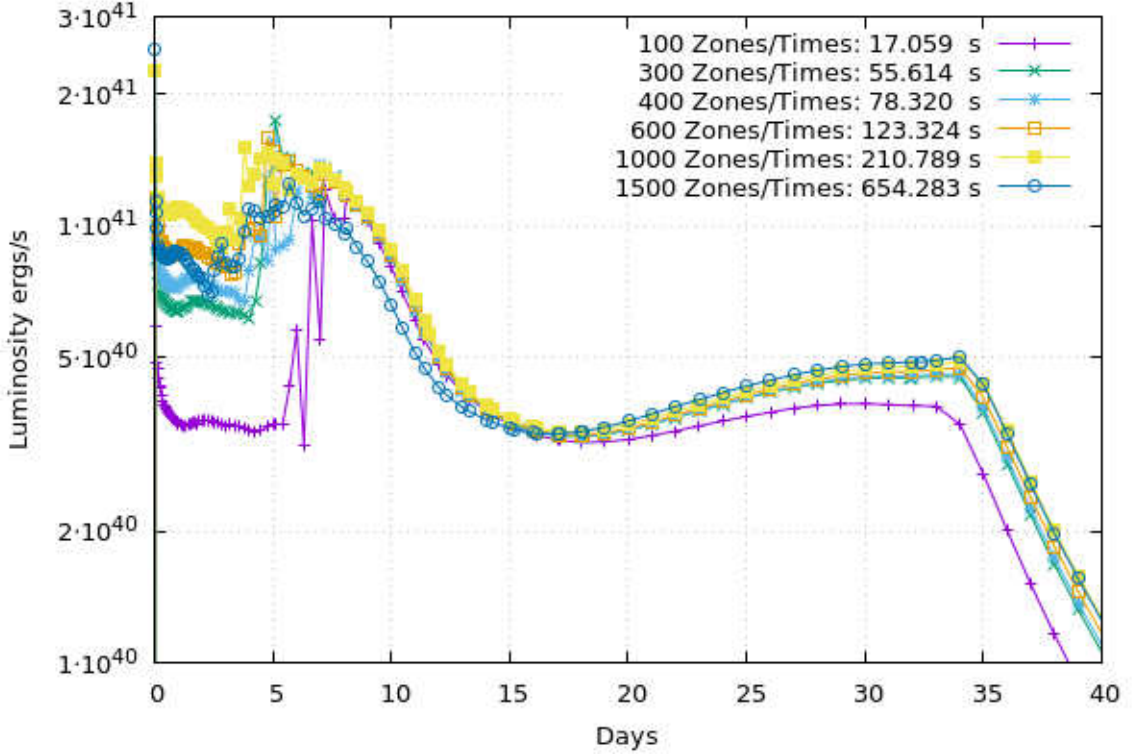
Figure 4. This is a 60 $M_\odot$ star exploded at 2.5×10^{51} ergs for six different gridding sizes

with the exception of the 100 zone model in which the pre-peak appears 40% dimmer and

misses the peak by a day. This model also dims sooner at the 15 day mark. This is due to

the coarse gridding not allowing the photosphere, calculated at $\tau = \frac{2}{3}$, to fall inward quick

enough and stays at an outer zone where the temperature falls quicker then the density as

the star expands. These differences are not great enough to require gridding beyond that of

600 zones, which falls approximately in the middle of the presented models.

2.3.2   Energy Injection

The physical central engine that powers the supernovae is still debated in literature and

some central engines work better than others but there is no consensus (Burrows, 2013;

Burrows et al., 2018). In general, the source of energy for the SN explosion comes from

the release of the gravitational binding energy of the stellar core collapsing to form a

compact remnant. Initiating a numerical explosion is a difficult calculation but can be approximated by injecting extra energy at the center of the model. The energy injected into the center of the model is required to be high enough such that the star becomes unbound.

In order to explode a model in a one-dimensional core collapse supernovae codes, the methods used in the literature ranges from thermal bombs (Tominaga et al., 2007), pistons (Heger et al., 2003), approximated or explicitly followed neutrino interaction (Messer et al., 1998; Sukhbold et al., 2016), and magnetar energy deposition (Kasen & Bildsten, 2010). In this work, the primary engine will be that of the thermal bomb. Neutrino heating, while most likely an important factor (Janka, H.-Th., 2001) in the shock revival of CCSNe, is assumed to be included in the thermal aspect. Any detailed interaction would be beyond the scope of this code, and is therefore not included. Magnetar energy injection, defined as the energy radiated by a rapidly rotating magnetized neutron star, is also neglected as it may help in the unbinding of the core, but not all CCSNe are expected to have this type of neutron star remnant. With no observations of Pop III SNe, there is no evidence to assume this type of central engine (Roy, 2013).

After the removal of the iron core zones in the original model, the temperature is artificially increased at the inner most zone to produce an explosion. Detailed calculations of the remnant formation is beyond the scope of the code and the mass that represents the remnant is removed from the model calculation. The increase in thermal energy creates a temperature discontinuity, which then diffuses out quickly forming a shock front. If the thermal energy is high enough, the envelope will unbind, forming a supernovae. If the energy is not, the supernovae fails and the code stalls due to a severe reduction in the time step of the calculation.

The total energy of the explosion is calculated as $E_{total} = E_{internal} + E_{kinetic} - E_{grav}$. The choice of temperature in the inner zone to produce the explosion is set at runtime by manually altering the initial model and checking the final energy. Changing the temperature in the inner zones ultimately gives a range of desired final energy in the explosion that match either observations or offer different possible scenarios.

2.4   Supernova Light Curves

The supernovae simulation is calculated for at least 200 days and in some cases up to 400 days. This covers the early time regime of the shock dominated physics and the late time light curve dominated by the radioactive decay of nickel. The physical properties of each zone, such as T, ρ, P, E are tracked through the evolution of the ejecta. These physical variables are used to calculate a wide set of observationally relevant parameters such as opacity, luminosity, and γ−ray deposition.

2.4.1   Light Curves

A lightcurve, defined as the luminosity versus time, is one of the primary tools to classify and study observed supernovae. From an observational perspective, SNe are observed in broadband filters with specific wavelength ranges but often lack full coverage across the electromagnetic spectrum.

In BOOM, which uses the grey atmosphere approximation, the net flux from the radiation is wavelength independent.

The luminosity is calculated at each zone in the model, but only the luminosity at the photosphere is used to calculat the lightcurve. The photosphere is defined as the surface of the star in which the optical depth is equivalent to $\tau = \frac{2}{3}$. The optical depth is

20

calculated as

$$\tau = \kappa s \rho \qquad (2.19)$$

where κ is the opacity, s is the distance traveled or thickness of the stellar layer, and ρ is the density. This is related to the mean free path of a photon (Mihalas, 1978). In `BOOM`, this is calculated by integrating τ starting at the outer most mass zone and then moving inward until a $\tau = 2/3$ term is reached. This mass zone is then treated as the zone that contains the photosphere and where the total luminosity is found using equation 2.13.

As per the grey atmosphere approximation, the flux from the star is called the bolometric flux. To calculate a wavelength dependent flux, the effective temperature of the photosphere is determined by the following

$$T_{eff} = max\left\{ \left(\frac{L}{4\pi r^2 \sigma} \right)^{\frac{1}{4}}, 5000K \right\} \qquad (2.20)$$

Where L is the photosphere luminosity and the left hand side of the *max* equation is the Stefan-Boltzman equation. This logic function, take from `BOOM`, sets a temperature floor, or minimum allowed temperature, of 5000 K. This is included to match the observations that the temperature never falls below 5000 K (Faran et al., 2018). Using this T_{eff} and a grid of filter-specific wavelength ranges, the Planck function can be integrated numerically. The application of the Planck function, as defined below, requires the assumption of a black body.

$$B_\lambda(T) = \frac{2hc^2}{\lambda^5} \frac{1}{e^{\frac{hc}{\lambda kT}} - 1} \qquad (2.21)$$

This is assumed to be accurate during the early shock-dominated phase of the supernovae

21

(Arnett, 1996). As the supernova evolves to the point in which the material is too diffuse, the black body approximation fails as an appreciable fraction of radiation field is decoupled from the material temperature. In order to follow the radiation field in detail, the radiation transfer equation is required. In the transition regime, the flux limiter is used to approximate the radiation field. The supernovae simulation is followed for up to 400 days, thus obtaining a light curve that can be compared to observations. For the population III CCSNe only the first 200 days are only considered due to severe redshift reductions in the luminosity making the later time lightcurve difficult to observe (Lawlor et al., 2015).

2.4.2 Filters

Broadband color filters have transmission curves, as shown in figure 5. The energy per second as a function of T and λ is
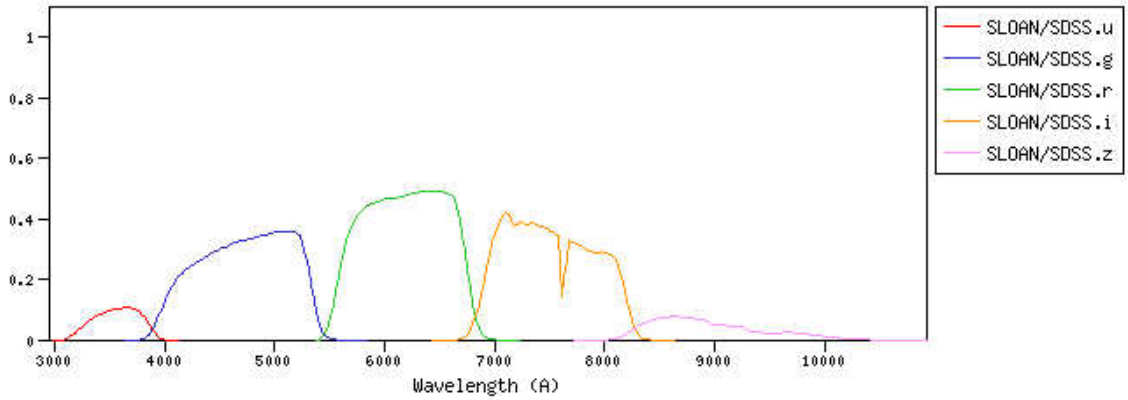
Figure 5. This is the Sloan filter set transmission curves. The z' filter is used in this work to determine the filtered light. Figure generated from the SVO filter service.

$$B_{\lambda,obs}(T) = B_\lambda(T) \times T(\lambda) \qquad (2.22)$$

where $T(\lambda)$ is defined as a set of discrete points within the filters $\Delta\lambda$ and 0 outside that range. The filter specific points are taken from the SVO filter service, see figure 5. The wavelength specific points tie into the numerical integration of the Planck equation.

2.4.3   Redshift

To determine the viability of observing a population III supernova, the simulated light curve is redshifted to account for the expansion of the universe. To compare to current observational campaigns, the focus is primarily on the 2MASS ks-band and the Sloan z' filter. A standard ΛCDM cosmology is assumed and is evaluated at two different redshifts $z = 5$ and $z = 15$. The wavelength is redshifted by the following equation

$$\lambda_{obs,z} = (1 + z)\lambda_{rest,0} \tag{2.23}$$

This redshifted wavelength is then used in the Planck equation to calculate a redshifted black body radiation field. The k-correction is also necessary at high redshifts and are taken from Kim et al. (1996). The k-correction is needed because light that would normally be observed in one filter is redshifted to a different filter. These two filters have two different transmission curves and the k-correction corrects this discrepancy. Using these k-corrections, the final apparent magnitude is calculated using equation 2.24.

$$m = 5log_{10}(d) - 5 - log_{10}(1 + z) + k \tag{2.24}$$

2.5   Central Remnant

The central remnant is the mass that presumably was left behind after the explosion. The formation of the remnant likely responsible for the energy of the explosion, releasing 10^{53} ergs during the collapse. As shown in figure 6, the mass of the central remnant has some relationship to the initial star mass and the metallicity.

In this work, several methods are considered to determine the central remnant such as the mixing-fallback method as described by Tominaga et al. (2007), the hydrodynamical fallback as used by Sukhbold et al. (2016), and a simpler assumed mass remnant as used by Morozova et al. (2015) and Lawlor et al. (2015). As mention in the previous section, the physics of the central remnant formation and interaction is beyond the scope of the code and the material that constitutes the remnant is removed prior to the hydrodynamics but still acts as a gravitational point mass.

For the purpose of this work, two methods were used to account for size of the central remnant. The first method is to assume that each star forms a central remnant composed of only the iron core. The edge of the iron core is approximately defined as the point where the iron abundance is less the 50% of the abundance of the layer. These results are tabulated in table 1.

Compared to the range of observed neutron star and black hole masses in Lattimer (2012) and Wiktorowicz et al. (2014), the degenerate iron core masses in table 1 fall around the 1.4 $M_\odot$, much closer to the neutron star masses then that of black holes.

As discussed in Heger et al. (2003), the higher mass stars have an increased chance of having a higher mass remnant. This is applied by assuming a neutron star remnant of a mass 1.44 $M_\odot$. The calculation of this mass includes the iron core, so that a 1 $M_\odot$ iron core

24
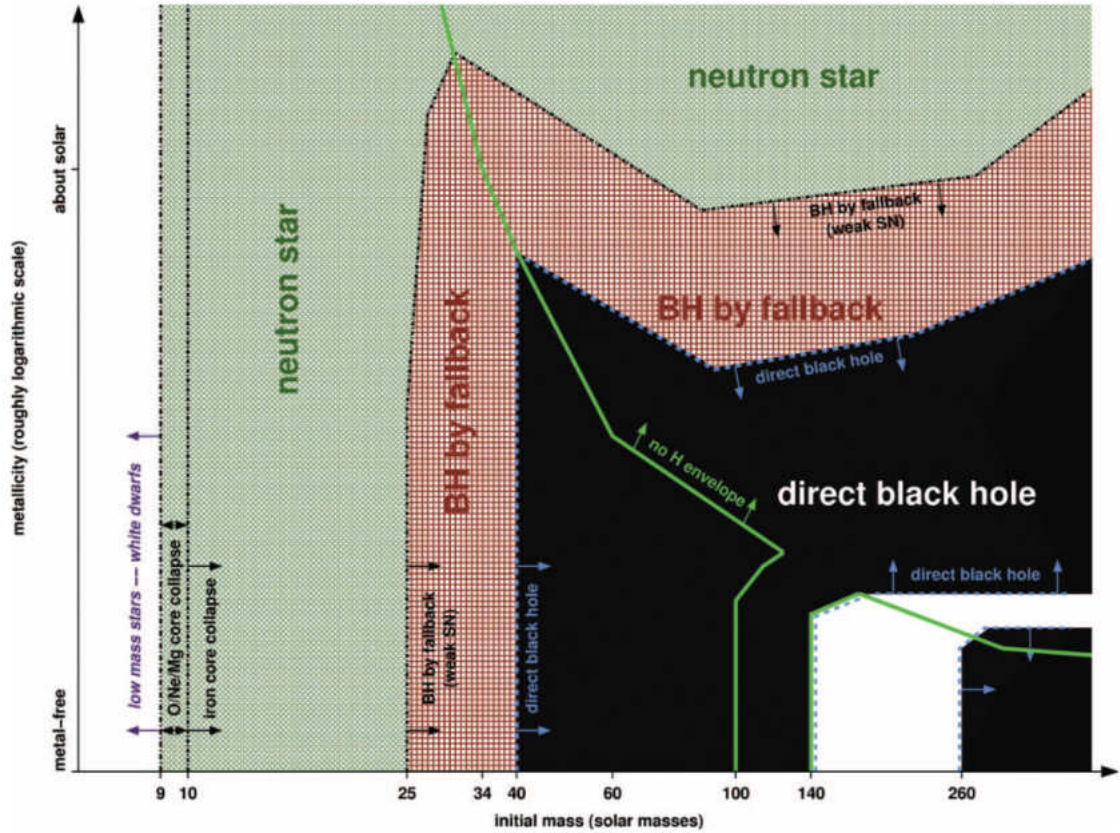
Figure 6. A plot of the likely SN type and remnant formed by a grid of star of different masses and metallicities. Zero metallicity follow the bottom of the graph. Figure taken from Heger et al. (2003)

would include 0.44 $M_\odot$ of material above the iron core into the remnant. For iron cores larger then 1.44 $M_\odot$, then no mass is taken from the iron core, and the neutron star would be the size of the iron core.

The last method that is used for this work is to assume that only a canonical mass of $Ni - 56$, or $0.07 M_\odot$ is ejected and everything below that amount falls back to the central remnant. The formation of $Ni - 56$ is primarily near the core so only the inner layers would fall back. This may not be ideal physically due to the amount of mixing during the shock waves initial traversal in the $Ni - 56$ forming regions.

Progenitor Mass ($M_\odot$)	Convection Criteria	Iron Core ($M_\odot$)
15	L	1.3
	S	2.08
20	L	0.66
	S	1.45
25	L	1.4
	S	1.2
30	L	1.497
	S	1.65
40	L	1.44
	S	2.08
50	L	1.75
	S	1.78
60	L	1.83
	S	1.73
70	L	1.91
	S	1.96
80	L	1.55
	S	0.035

Table 1. Shown in column three is the degenerate iron core masses left over at the end of the stellar evolution process. Model 80S does not form a degenerate iron core due to pair-instability at the end of its evolution and is not considered for this study.

2.6 Nucleosynthesis

Nucleosynthesis is handled by a large nuclear network simulation code that track interactions between species and energy as well as the decays of unstable isotopes as a function of temperature and density. The nuclear network code used is called TORCH developed by F.X. Timmes (Timmes et al., 2000; Timmes, 1999). TORCH is a general purpose nuclear network code , but is used in this case in its full 3302 isotopes version in the post-processing capacity. Post-processing in this case means not coupled to the hydrodynamic run or participates in the energy release by the reaction and decays. BOOM tracks the temperature-density profiles as a function of time and composition for each zone and is used as input for TORCH.This post-processing method is used in Tominaga

et al. (2007) and generally allows a higher number of isotopes to be used compared to a coupled nuclear network code which requires the number of isotopes to be lower due to the high number of interactions per timestep.

2.6.1 TORCH

As TORCH was not developed for this work, only a brief description of the code will be given. TORCH, as seen in (Timmes et al., 2000; Timmes, 1999), seeks to solve a general equation of the form

$$\frac{dY_i}{dt} = \sum_{j,k} Y_l Y_k \lambda_{kj}(l) - Y_l Y_j \lambda_{jk}(i) \tag{2.25}$$

where λ_{kj} and λ_{jk} are the creation and destruction nuclear reaction rates respectively. Y_x is the molar abundances of species $\mathbf{x}$. This equation can be recast into a more compact and standard form of

$$\dot{\mathbf{y}} = \mathbf{f}(\mathbf{y}) \tag{2.26}$$

This is a set of stiff ODE's and can be solved by use of a sparse Jacobian matrix as described in Timmes (1999). In figure 7 an example of a Jacobian matrix for the smaller 489 isotope network is shown. For the larger networks, the matrix becomes larger. Each direction in the matrix defines a nuclear reaction. For example the (γ, n) reaction, and its reverse, is the reaction of an element with $\gamma - ray$ that produces another element and a neutron.

2.6.2 Input and Output

Computationally, a 3302 isotope nuclear network calculation for a 600 zone model is a slow process, taking several minutes per zone. The time-step for the hydrodynamics
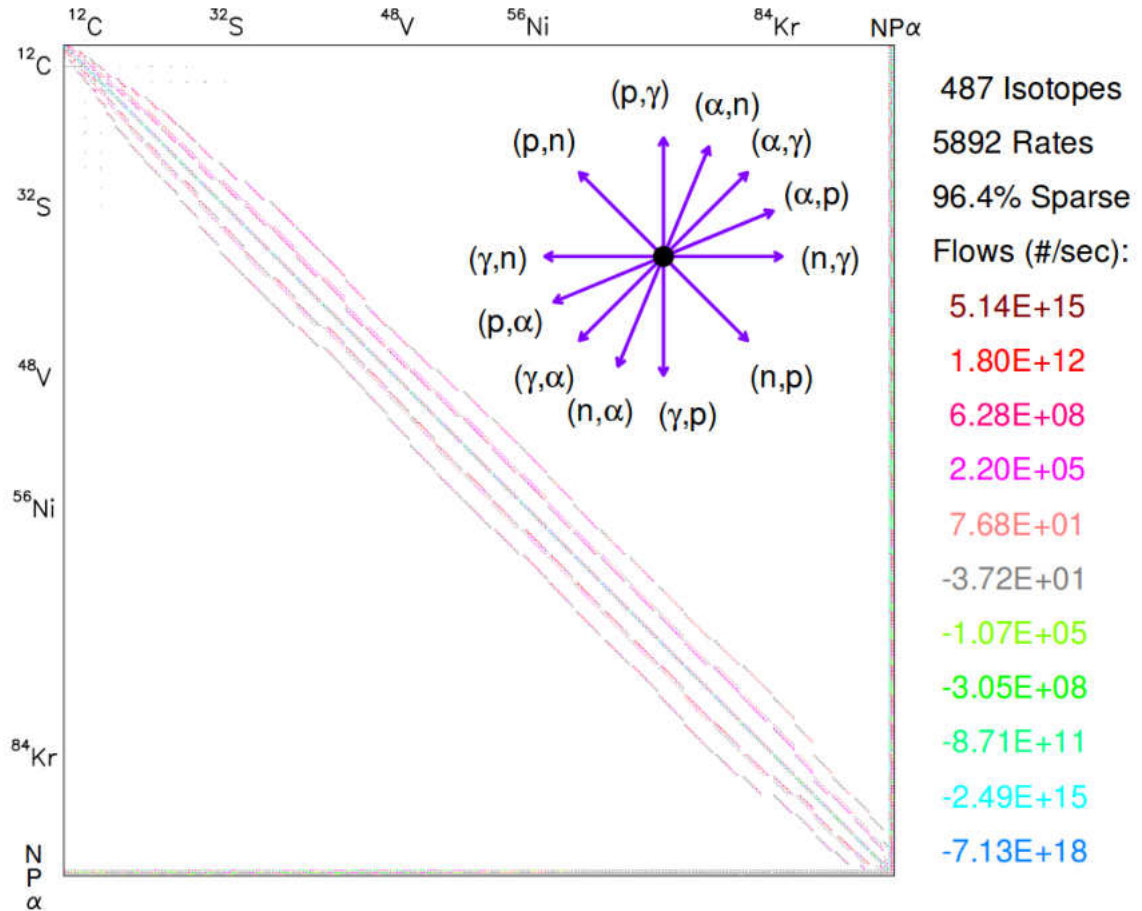
Figure 7. A sparse Jacobian matrix for the 489 isotope nuclear network. The color denotes the net positive or negative flow into each isotope. Figure taken from Timmes et al. (2000)

during the early time explosion is short, limited by the speed of sound through any given mass zone. Using the temperature-density profiles at every time step produces outputs several hundred megabytes per zone, and maintains a fine mesh of detail even during times of no dynamics for zones either pre- or post-shock. To simplify the process, the temperature-density profiles are tracked for only a short time when the temperature-density is high enough for nucleosynthesis to occur, which is usually on average of 5 days after the explosion. In addition, not every timestep is saved for use in TORCH. When the timestep is short, every other or every 5th timestep was saved but when

the timestep becomes larger, then every timestep was used. This allowed the temperature-density profiles to still be fine enough to capture the shock and coarse enough to keep the TORCH calculations manageable.

CHAPTER 3

Data

3.1 Population III Supernovae

Table 2 shows the final pre-explosion radii of the 18 progenitor stars used in this work,

nine stars for both the Ledoux and the Schwarzschild convection criteria. These models

are exploded in two energy ranges, a high and a low, with only the degenerate iron core

removed shown in table 1.

Mass/$M_\odot$	$R_{Ledoux}/R_\odot$	$R_{Schwarzschild}/R_\odot$
15	8.74	603
20	9.57	341
25	12.12	567
30	12.06	1066
40	16.08	2048
50	20.51	520
60	22.59	1038
70	64.6	399
80	28.09	179

Table 2. Initial radii and mass in terms of Solar units, where $R_\odot$ is 6.96×10^{10} cm

3.1.1 Low Energy CCSNe

The low energy CCSNe are defined as having the minimum explosion energy required to

completely eject the envelope of the star. Table 3 shows this range of energies for the

Ledoux and Schwarzschild models. These CCSNe are exploded and tracked for up to 400

days, but only the first 200 days will be presented. The minimum energy to explode each

model is dependent on mass and the density structure of the model and thus is not the

same for each model.

$M_\odot$	Convective Criteria	Energy ($10^{51} ergs$)
15	L	1.03
	S	1.13
20	L	1.22
	S	1.1
25	L	1.5
	S	1.1
30	L	2.4
	S	1.03
40	L	2.42
	S	1.1
50	L	3.4
	S	1.7
60	L	4.67
	S	1.8
70	L	2.9
	S	2.3
80	L	6.48
	S	0

Table 3. Minimum energy values for the Ledoux and Schwarzschild Models

3.1.1.1 Ledoux Models

The Ledoux progenitors are compact stars, defined by smaller radii and a more compact core. This produces a low luminosity pre-supernova star due to the r^2 dependence in equation 2.13. Figure 8 shows the light curves for this series.

The light curves for Ledoux series show several similar characteristics. For one, they are all low luminosity, having a bolometric luminosity lower than $L = 10^{44} \frac{ergs}{s}$, lower than typical CCSNe (Nadyozhin, 2003). This is primarily due to the compact nature of the star.

There is a feature present in most of the Ledoux models starting at about 10 days. This feature shows a dip in luminosity between 2-4 orders of magnitude. The photosphere
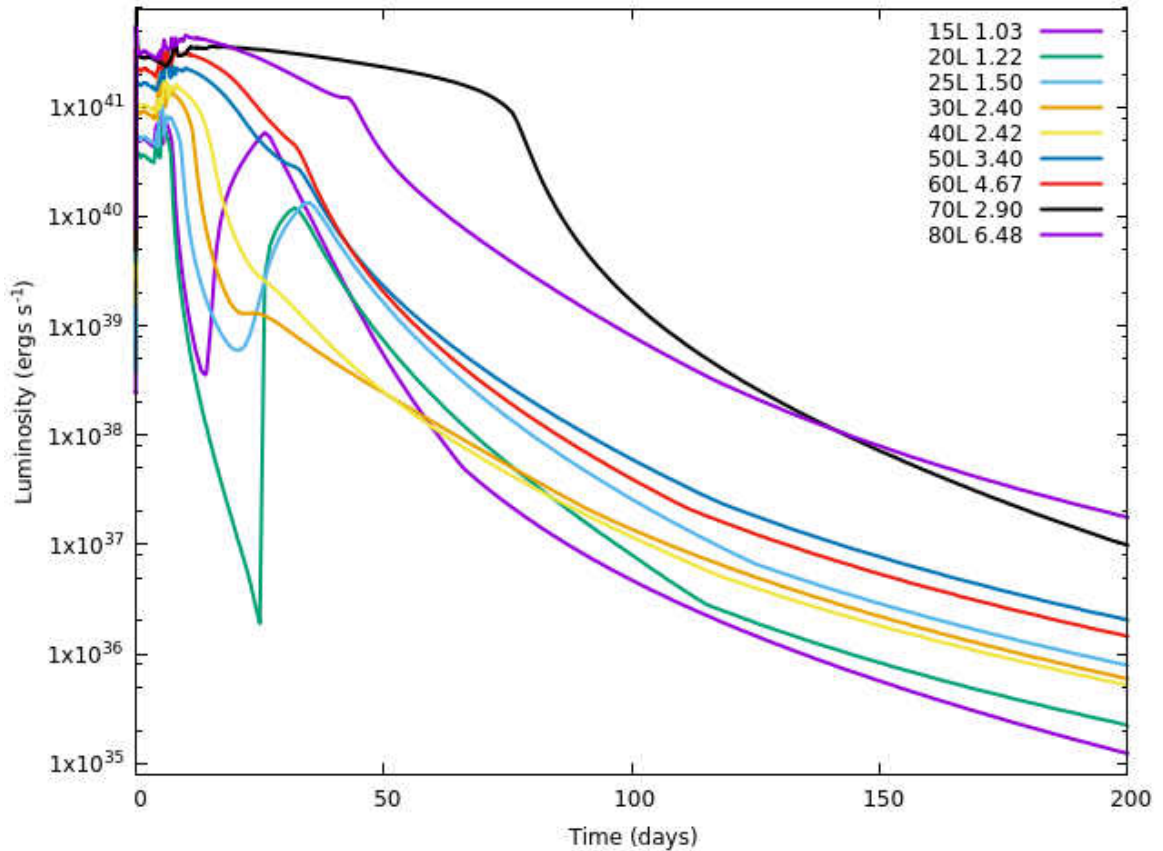
Figure 8. This is the Ledoux series of models exploded at the minimum energy required for complete envelope ejection

is initially near the outer edge of the model star. As the shock initially traverses through

and finally exits the star, the shock heats the material behind it, producing a hotter

photosphere layer. This photosphere layer is now hot, but still on the edges of the star, but

being moved outwards. This new temperature causes the brightness to increase. But the

expansion now causes the outer most zone to cool faster the the radius expands, due to the

T^4, as shown in 2.13, dependence compared to the r^2 surface area dependence in the

luminosity calculation. The density of these layers has only a r^3 in the volume so the

temperature effect out paces the density as well. As the star keeps expanding, the

photosphere begins to recede into the hotter inner layers of the star and then begins to

brighten before the expansion out paces the temperature and then the star starts to cool

finally. This feature is lessened as you increase the energy, with the deepest drop being the

lowest energy Ledoux supernova.

The energies required for these models, shown in table 3, are higher then

observationally derived energies for typical Type II SNe but not greater than the

hypernovae range with energies $E_{51} > 10$. Considering that in these models there was a

complete ejection of the envelope, its likely that there are lower energies in which the star

would explode, but would experience more fallback, leading to a larger remnant mass. In

some cases, even lower energies might lead to the direct formation of a black hole (Chen

et al., 2017).

Comparing to the lightcurve of SN1987a, the 15-25 $M_\odot$ models show several

similarities (Blinnikov et al., 2000). After failed attempts at modeling the traditional red

supergiant progenitor for SN1987a, it was finally shown to be more consistent with a

compact blue supergiant. In numerical simulations that are fit to observation there is a

secondary peak in the SN87a light curve in which the photosphere is held further out due

to the energy release by the beta decay of $Ni - 56$. The secondary peak becomes more

pronounced, matching observations. It was required to mix nickel outwards into the

hydrogen layers in order to achieve a smooth transition in the light curve from shock

heating to radioactive heating at around the 40 day mark. The peak in the Ledoux models

is hydrodynamic in nature, but becomes broader and longer when nickel is included into

the calculations, as shown in figure 9. The effect of nickel heating becomes noticeable

when the photosphere reaches the extent of the gamma-ray heated material, ranging from

20-80 days for these compact stars. In figure 9, the extent of the nickel mixing was out to

33

the edge of the helium layer. With further mixing out into the hydrogen layer the secondary peak would occur earlier and likely be more pronounced.
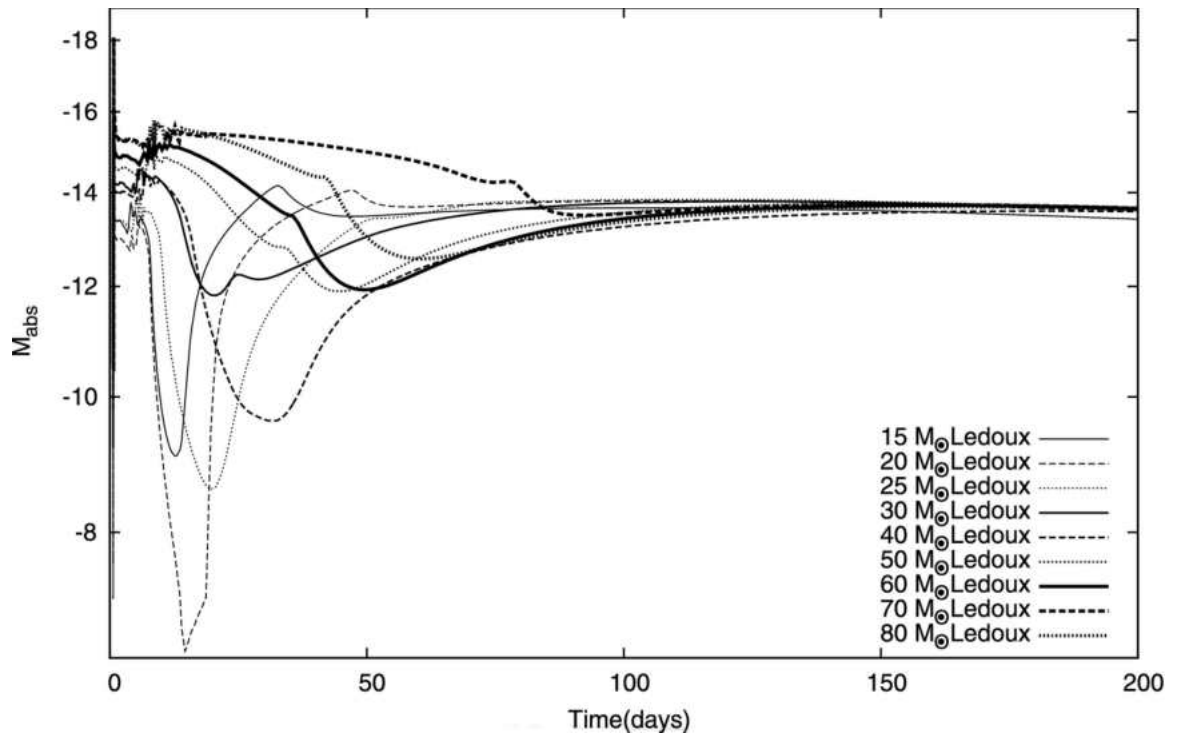
Figure 9. Low energy Ledoux series with addition of gamma ray deposition

3.1.1.2 Schwarzschild Models

The Schwarzschild models have very large progenitor radii, primarily in an extended low density hydrogen envelope. This is matched with a gradual gravitational potential in the core, requiring less energy to completely eject the envelope, seen in Table 3. Figure 10 shows the light curves for this series.
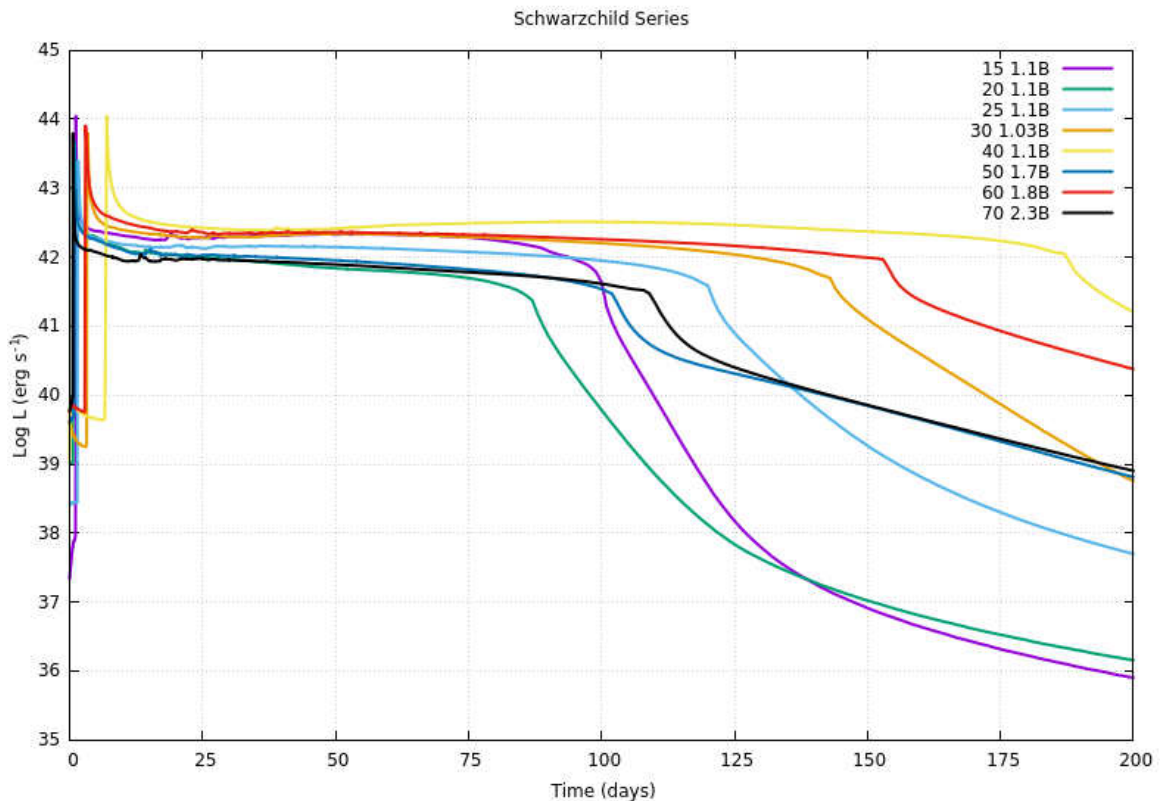
Figure 10. This is the Schwarzschild series of models exploded at the minimum energy required for complete envelope ejection

The light curves for this series of models show similar characteristics within the Schwarzschild models, but differ to the Ledoux series. A key feature in this series it the very bright shock breakout and the long plateaus. The plateau feature is common for large radii progenitor stars and defines a subclass of Type II SNe called Type IIP's. The plateau feature is formed by a velocity balance of the photosphere receding at approximately the

same speed in which the material is moving outwards. These two combine in a way that the luminosity remains constant over a period of time. The length of this plateau is dependent on several factors (Young, 2004), such as radii, explosion energy, and progenitor mass. Compared to the Ledoux models, the Schwarzschild shock breakout luminosity is two orders of magnitude brighter while the plateau luminosity is consistently brighter in all phases, lasting from $80 - 100$ days.

There is a noticeable lag time between the start of the shock at the core and the appearance of the shock at the surface. This is more noticeable with the Schwarzschild models compared to the Ledoux models at early times. The shock must travel a significantly further distance to reach the surface in the larger radii of the Schwarzschild series. The $40M_\odot$ model has the largest radii and also the longest time for shock breakout.

Due to the low minimum energy of these SNe, there is most likely lower energy SNe with high amounts of fallback, especially considering the higher mass models likely produce higher mass remnants (Heger et al., 2003). Assuming a standard energy of 1×10^{51} ergs to about 1.2×10^{51} ergs, the formation of a remnant mass is expected to be higher for the Ledoux series compared to that of the Schwarzschild series due to the possible lower energies required.

3.1.2 High Energy CCSNe

A higher explosion energy series was calculated by artificially setting the temperature high enough to reach 10×10^{51} ergs. These high explosion energy supernove are called hypernovae, or HNe. The exact energies per model used is shown in Table 4

Mass ($M_\odot$)	Convective Criteria	Energy ($10^{51} ergs$)
15	L	10.1
	S	5
20	L	10.7
	S	9.98
25	L	10.3
	S	10.5
30	L	10
	S	10.3
40	L	10
	S	9.9
50	L	10
	S	10.5
60	L	10.1
	S	10.3
70	L	10.1
	S	10
80	L	10.06
	S	0

Table 4. Hypernovae energy range for the Ledoux and Schwarzschild series

3.1.2.1 Ledoux Models

Shown below is the graph of all the final light curves of the HNe Ledoux series.

As discussed in a previous section, the dip in the Ledoux series was due to the compact nature of the star, but became less prominent as the energy increased. At high energy, none of the light curves show the dip in the early times. In Figure 12, a single star is exploded at several energies to examine the effect of changing the energy independent of other parameters.
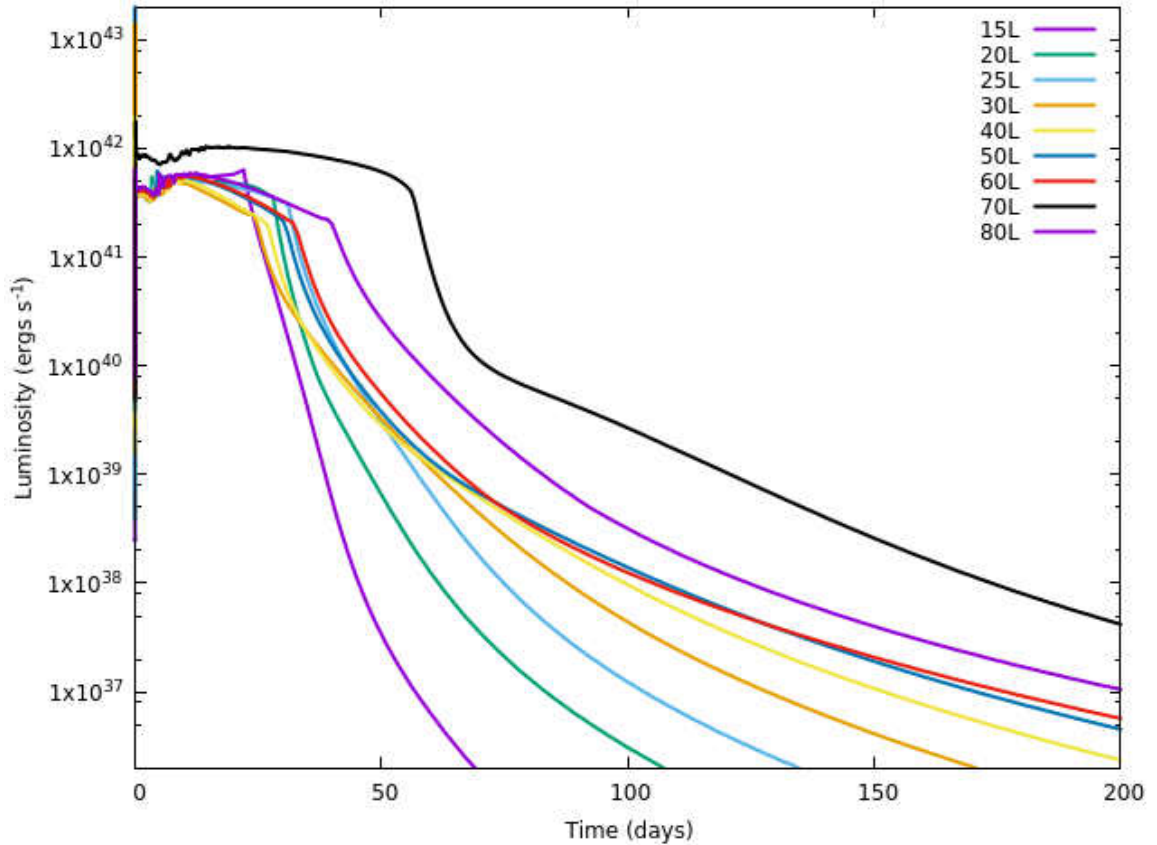
Figure 11. This is the Ledoux series of models exploded at the energies shown in Table 4

As the energy is increased, three features change in the lightcurve, noting that the rest of the models show a similar pattern. The first is the initial luminosity increases by an order of magnitude. This is due to the higher shock energy imparting a higher temperature to the material. The second primary feature is the dip, as discussed in section 3.1.1, is absent. With the increased energy, the material is given a higher outward velocity. This increased velocity begins to create a plateau feature, as discussed in section 3.1.1.2. Similar to that of the Schwarzschild SNe, as the energy is increased, the plateau feature shortens in time causing a faster light curve meaning the similar features are seen earlier. The final feature is the hydrodynamic-only post-plateau, called the tail. The higher energy forces the ejecta to expand quicker, causing the photosphere to recede inward. The
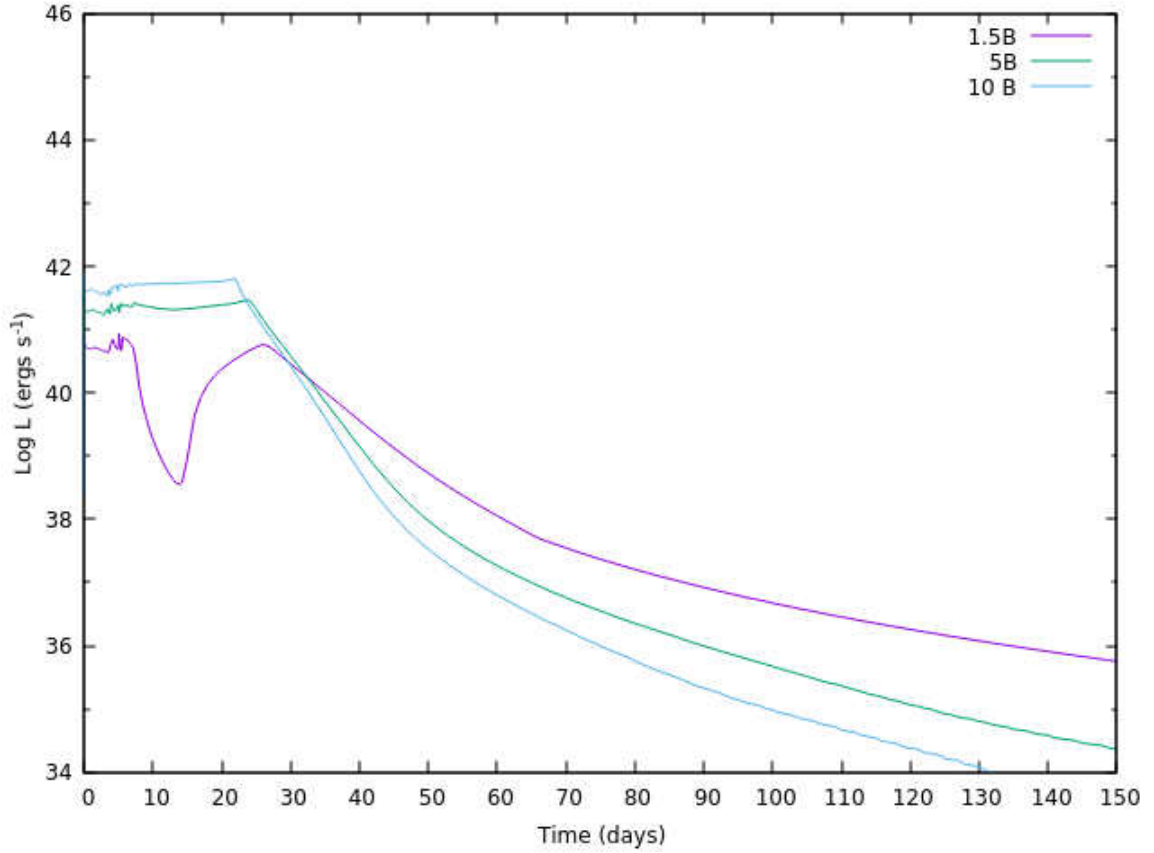
Figure 12. This is the 15 $M_\odot$ Ledoux model exploded at a range of three energies. A Bethe (B) is defined as 1×10^{51} ergs and is used in honor of Hans Bethe

expanding material is now moving faster, causing layers to cool quicker resulting in a

lower luminosity photosphere.

3.1.2.2 Schwarzschild Models

Shown below is the figure of all the final light curves of the HNe Schwarzschild series.
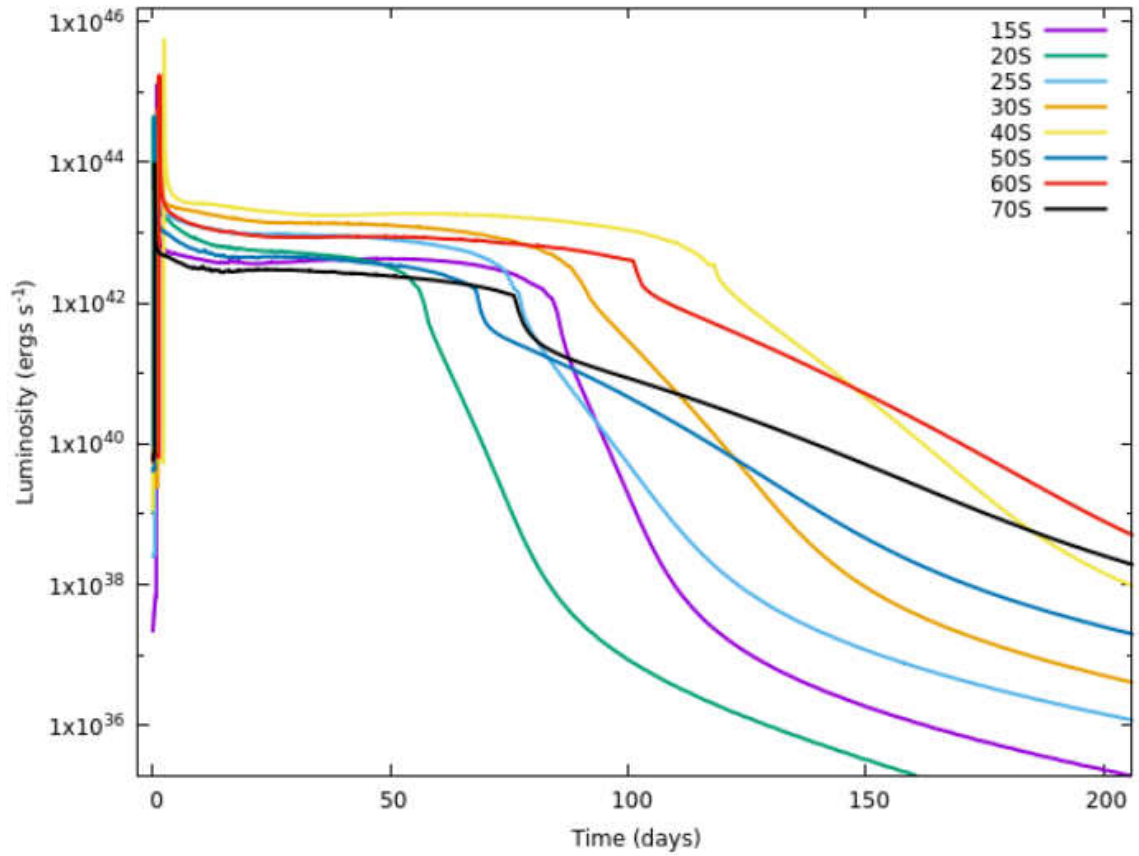
Figure 13. This is the Schwarzschild series of models exploded at the energies shown in Table 4

The HNe in the Schwarzschild series are similar to those in the lower energy SNe and are similar to Type II-P light curves. The higher energy HNe produce shorter but brighter plateau features. This is shown in figure 14
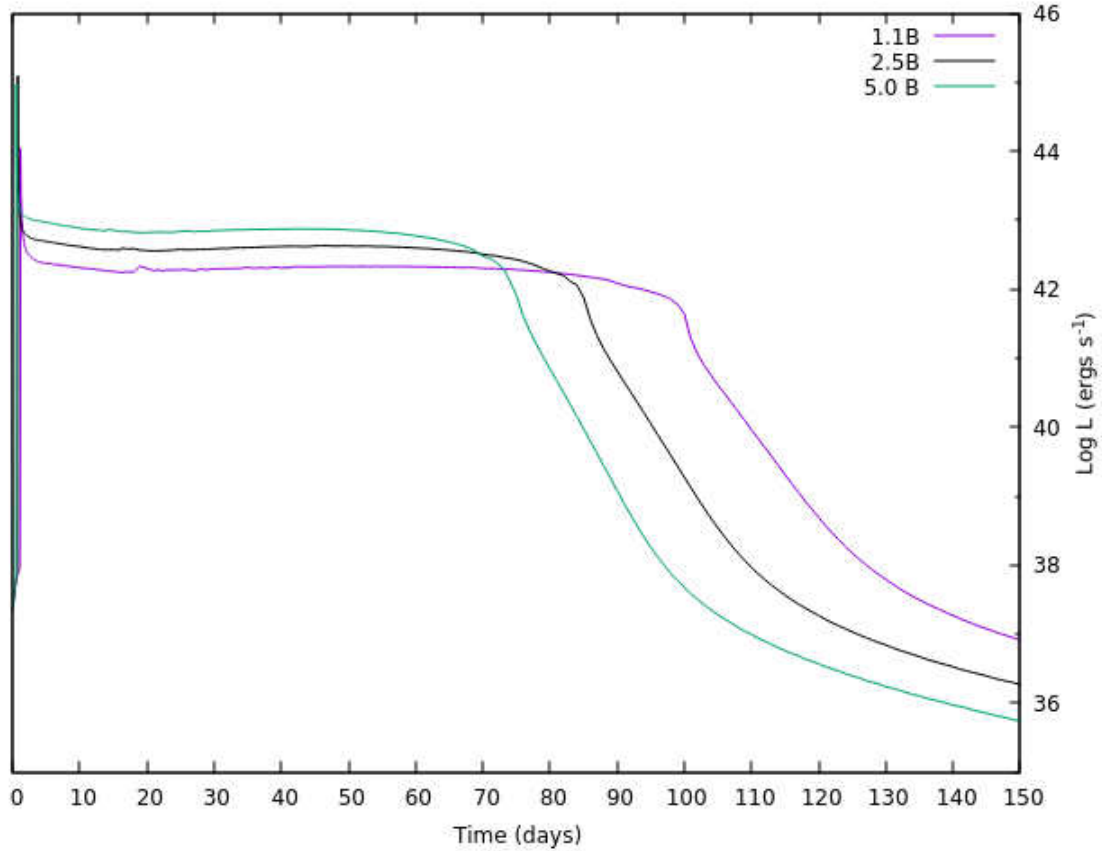
Figure 14. This is the 15 $M_{\odot}$ Schwarzschild model exploded at a range of three energies. A Bethe (B) is defined as $1 \times 10^{51} ergs$

3.1.3 High Redshift CCSNe

As discussed in chapter 2, to reproduce Population III supernovae, the luminosity is redshifted and integrated into wide-band filters. Figure 15, shows an example of a lightcurve redshifted in a set of filters. In equation 2.21, the wavelength λ is substituted with equation 2.23. The Planck distribution of radiation is shifted towards redder wavelengths for more distant objects due to the expansion of the universe. Thus, the magnitude in each filter changes, which can be shown easily in figure 15.

Figure 16 shows a set of lightcurves redshifted to $z = 15$ and indicates JWST limiting magnitude in the z' band and the 2MASS Ks band while figure 17 shows the

41
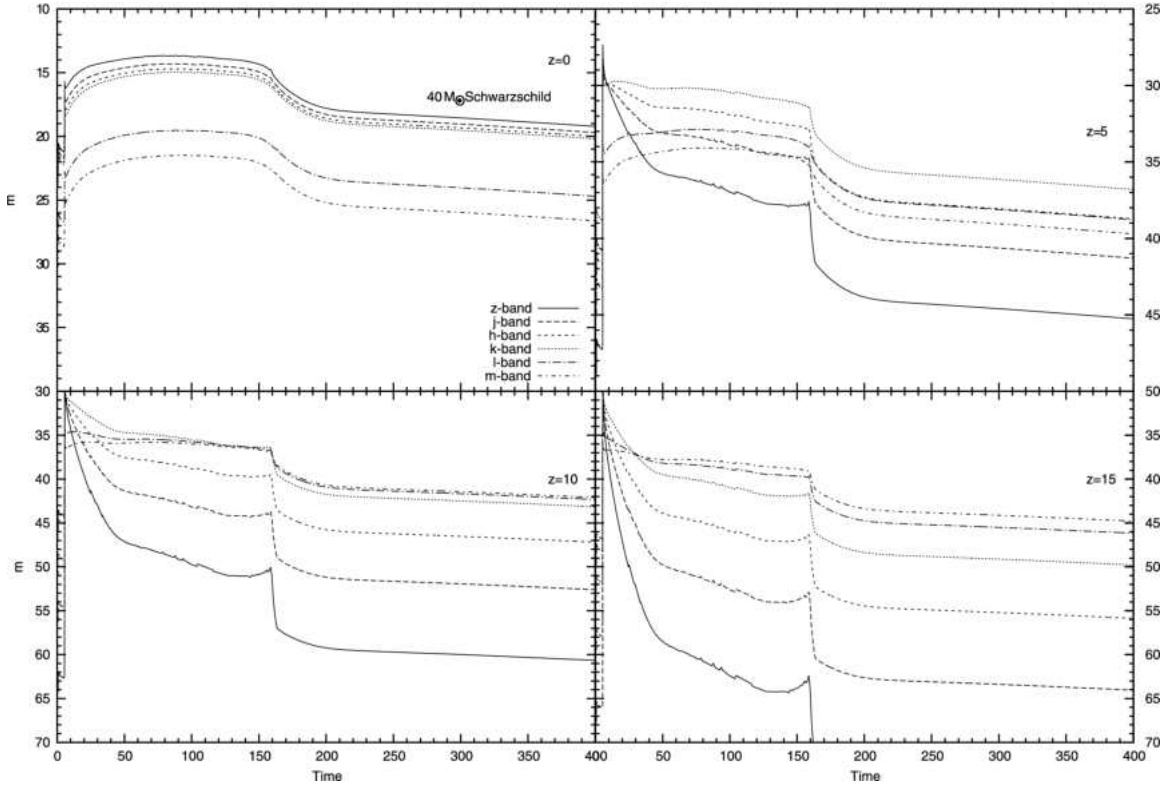
Figure 15. The 40 $M_\odot$ Schwarzschild model redshifted to $z = 0, 5, 10, 15$ in the zjhklm filter range

same bands and lightcurves at a redshift $z = 5$. As discussed in (Lawlor et al., 2015), the detectability of these population III CCSNe are low and can only be observed in the $1 - 10$ day window for the majority of the models across both convection criteria. There is slightly improved detectability in the $z = 5$ range for the Schwarzschild series.

As shown in the previous sections, the luminosity changes approximately by an order of magnitude when the explosion energy is increased by a factor of 10. This would likely extend the detectability for some of the models for 5-10 more days, going beyond peak of the light curve and revealing more of the plateau. For the low energy Ledoux, this may limit the detectability due to the luminosity dip in the Ledoux models. In this case, the nature of even having a detection could allow observers to distinguish between compact and large-radii progenitors.
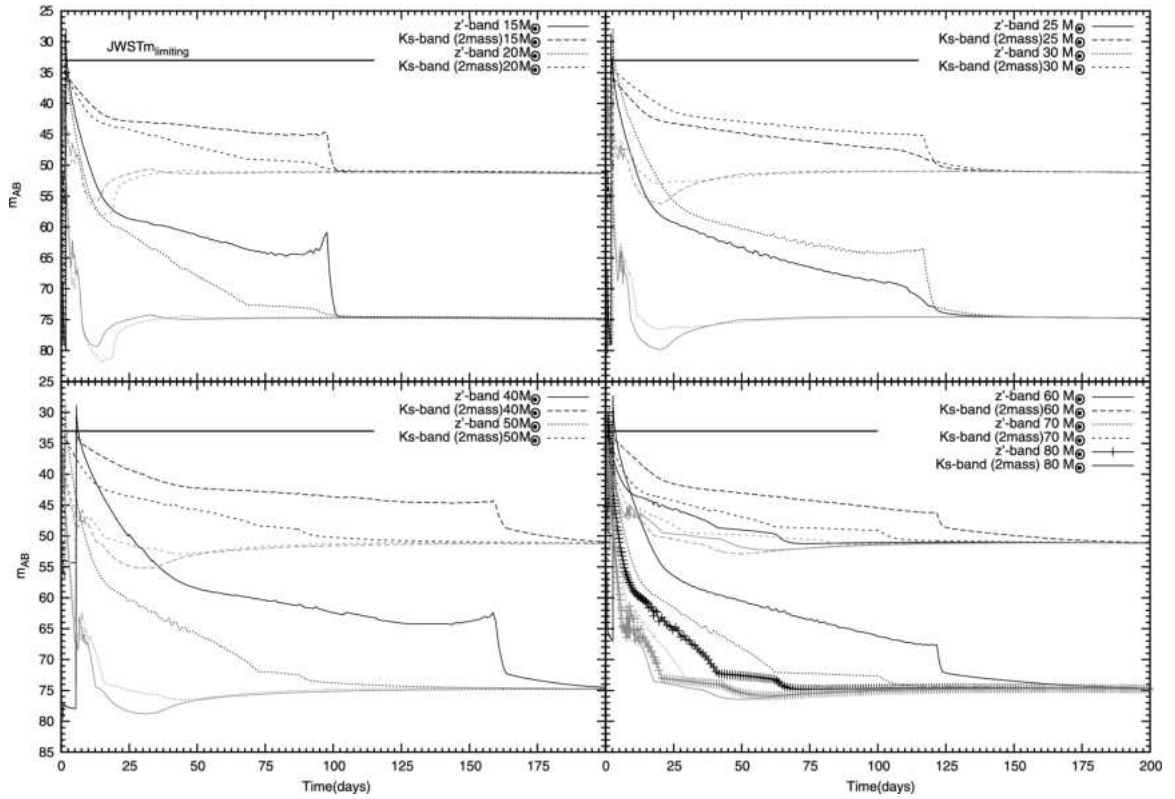
Figure 16. The bold lines are the Schwarzschild and the faint lines are the Ledoux with a redshift of $z = 15$

These calculations do not consider the effects of lensing, which as shown in Goldstein & Nugent (2017), Kelly et al. (2015), is likely to increase the magnitude and duration of the observations.
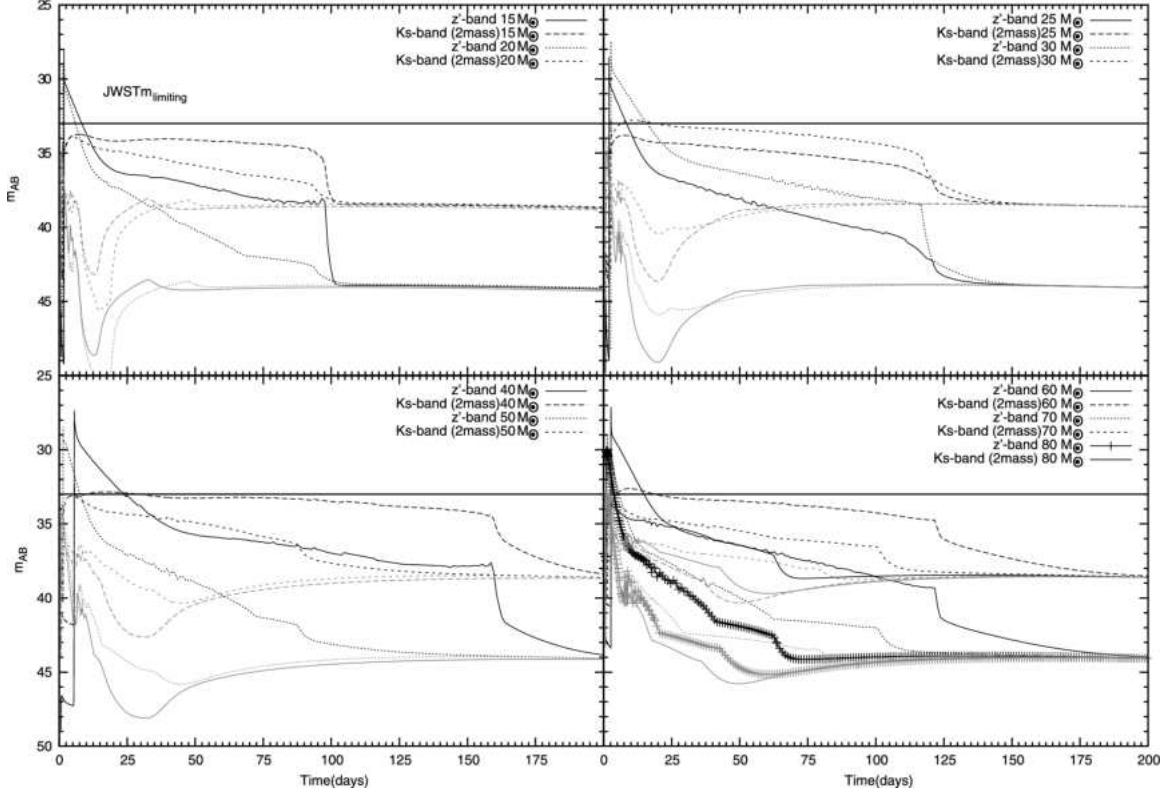
Figure 17. The bold lines are the Schwarzschild and the faint lines are the Ledoux with a
redshift of $z = 5$

3.2 Nucleosynthesis

The results from the TORCH nucleosynthesis calculations for low and high energy will be

presented with the following assumptions and conventions. First, solar abundance values

from Asplund et al. (2009) are used. This is a more recent publication, compared to the

widely cited (Anders & Grevesse, 1989). The notation used in abundance calculations is

that of the logarithmic ratio of some element to either hydrogen or iron, denoted as

$[X/Fe]$[1] and $[X/H]$.

All abundance values, unless noted otherwise, can be considered to be including

the entire ejecta. This means that each abundance value is not just the yield from the

---

[1]This is defined as $[X/Fe]$ as $log_{10}\left(\frac{N_m}{N_{Fe}}\right)_{star} - log_{10}\left(\frac{N_m}{N_{Fe}}\right)_{Sun}$

CCSNe explosion itself but nucleosynthetic yields plus the initial pre-core collapse yields.

3.2.1   Low Energy

Table 3, lists the energy ranges used to determine the SNe of the low energy range.

3.2.1.1   Ledoux Models

Table 5 shows the $[X/Fe]$ abundances values post explosion for the Ledoux models.

Figures 18 to 20 graphs the yields in terms of $[x/H]$. The low energy Ledoux series have

different explosion energies associated with each mass model. The explosion energies of

the models vary enough that caution should be used when making generalized trends

regarding the yields. The yields of beryllium in the Ledoux models is higher relative to

solar and the Schwarzschild abundances. The abundances of 60L model is quite different

compared to that of the other Ledoux series models. The abundances of the light n-capture

elements (Sr, Y, Zr) (Burris et al., 2009) will be discussed in chapter 4
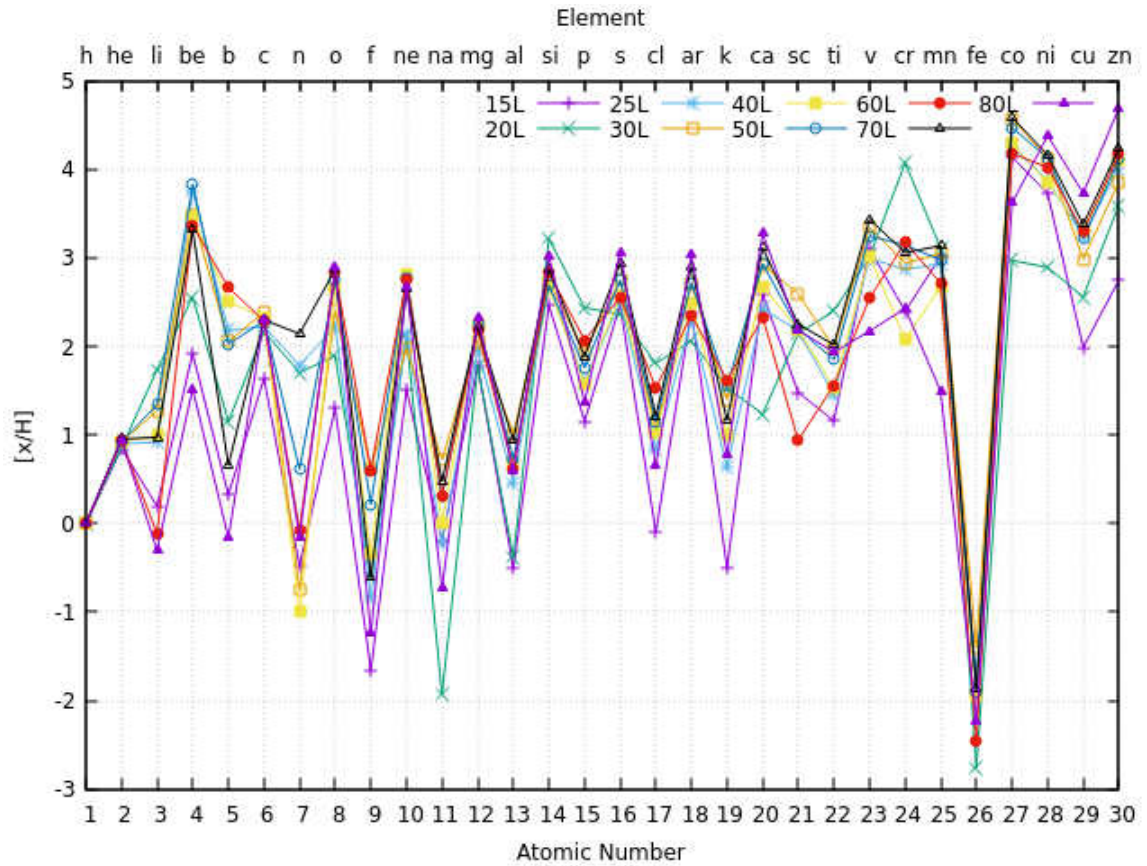
Figure 18. Ledoux series $[X/H]$ for $1 > Z > 30$

3.2.1.2   Schwarzschild Models

In table 6 and figures 21 to 23 the $[X/H]$ results for the low energy Schwarzschild series are shown. Compared to the Ledoux series, the Schwarzschild series has lower abundances in the in the $Z > 60$ range.
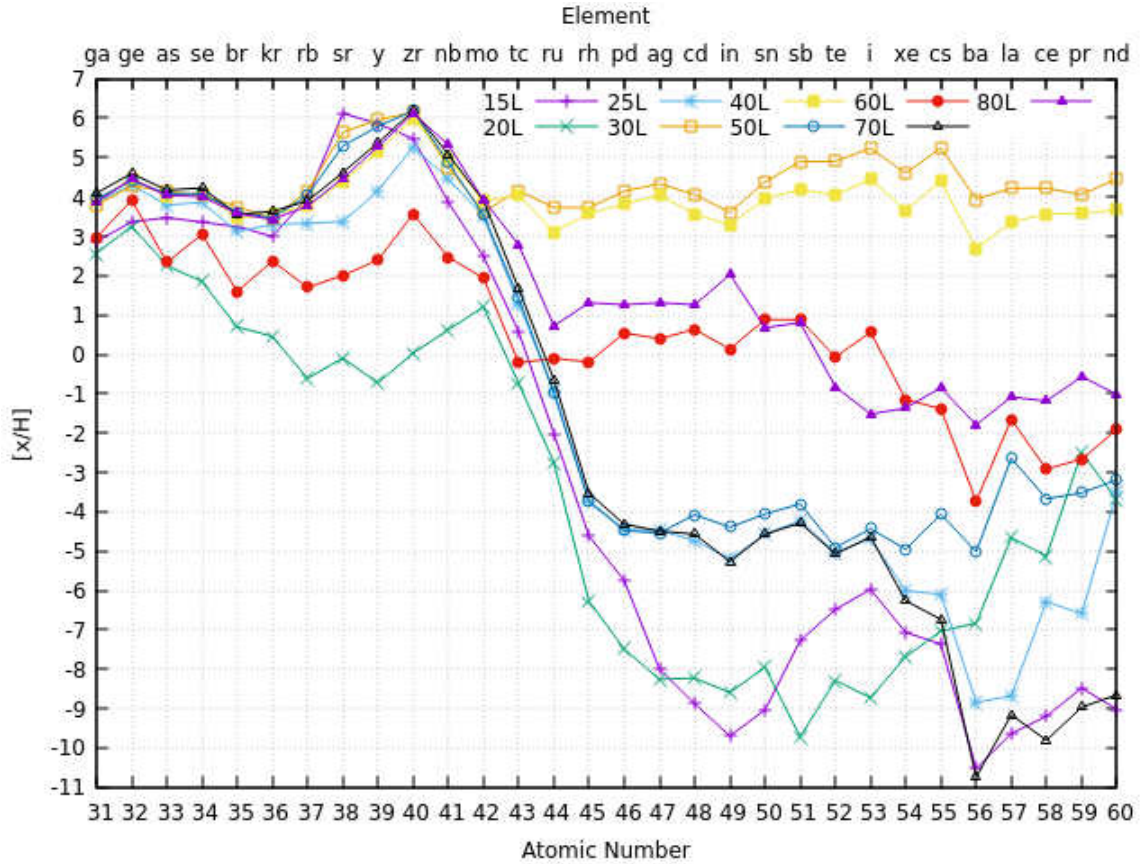
Figure 19. Ledoux series [*X*/*H*] for 31 > Z > 60

3.2.2   *High Energy*

The high energy nucleosynthesis uses the same energy range as in figure 4, but only the

graphs are shown.

3.2.2.1   Ledoux Models

Figures 24 to 26 show the abundances for the high energy Ledoux series. The increase in

explosion energy in the simulations tends to increase the yields across the range of

elements shown, especially in the high Z range. However, the 30 and 40 $M_\odot$ models do

not show a significant change in abundance as the low to high simulation explosion energy

changes. They show a noticeable change in the abundances in the Sr,Y,Zr range in which

the higher energy series has lower yields than that of the lower explosion energies. This
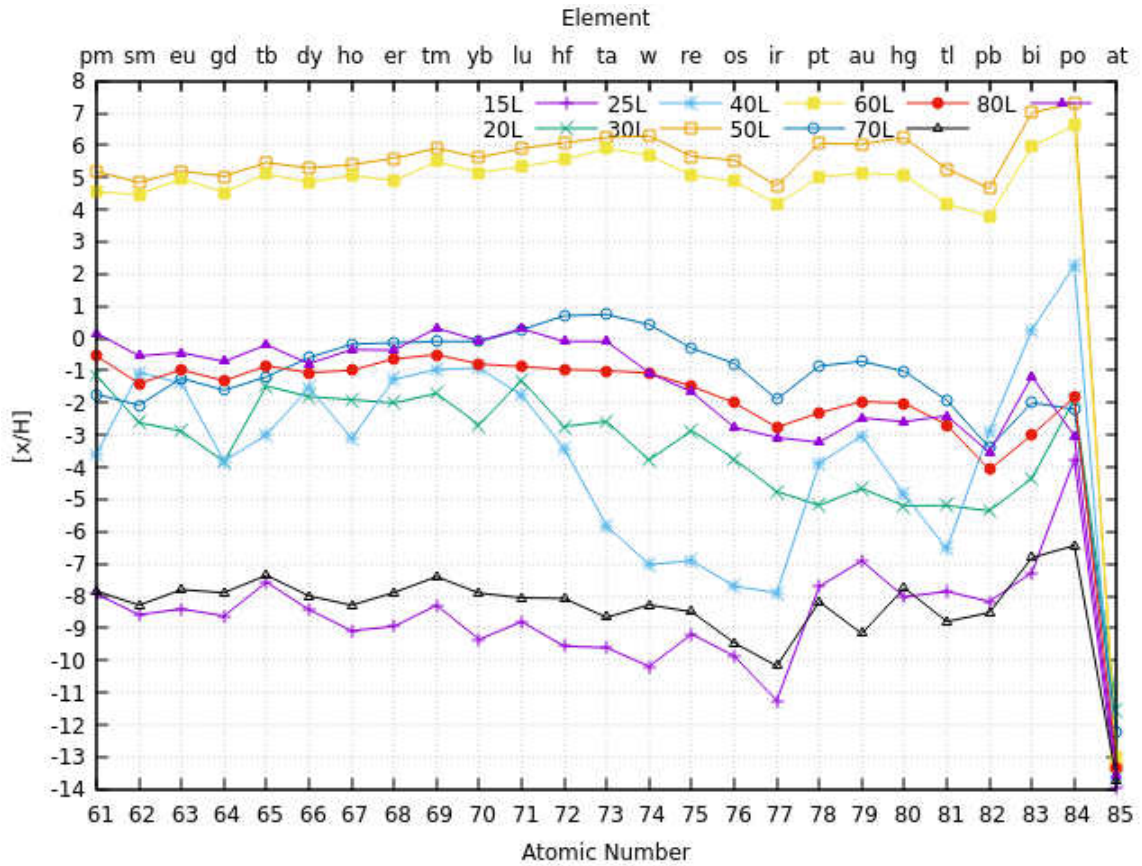
Figure 20. Ledoux series $[X/H]$ for $61 > Z > 85$

implies that either the shock energy caused the produced Sr, Y, and Zr to be fused into

higher Z elements as seen in the high explosion energy series, showing a slight increase in

abundances over all higher Z element or that the shock passed too quickly for this series to

be produced.
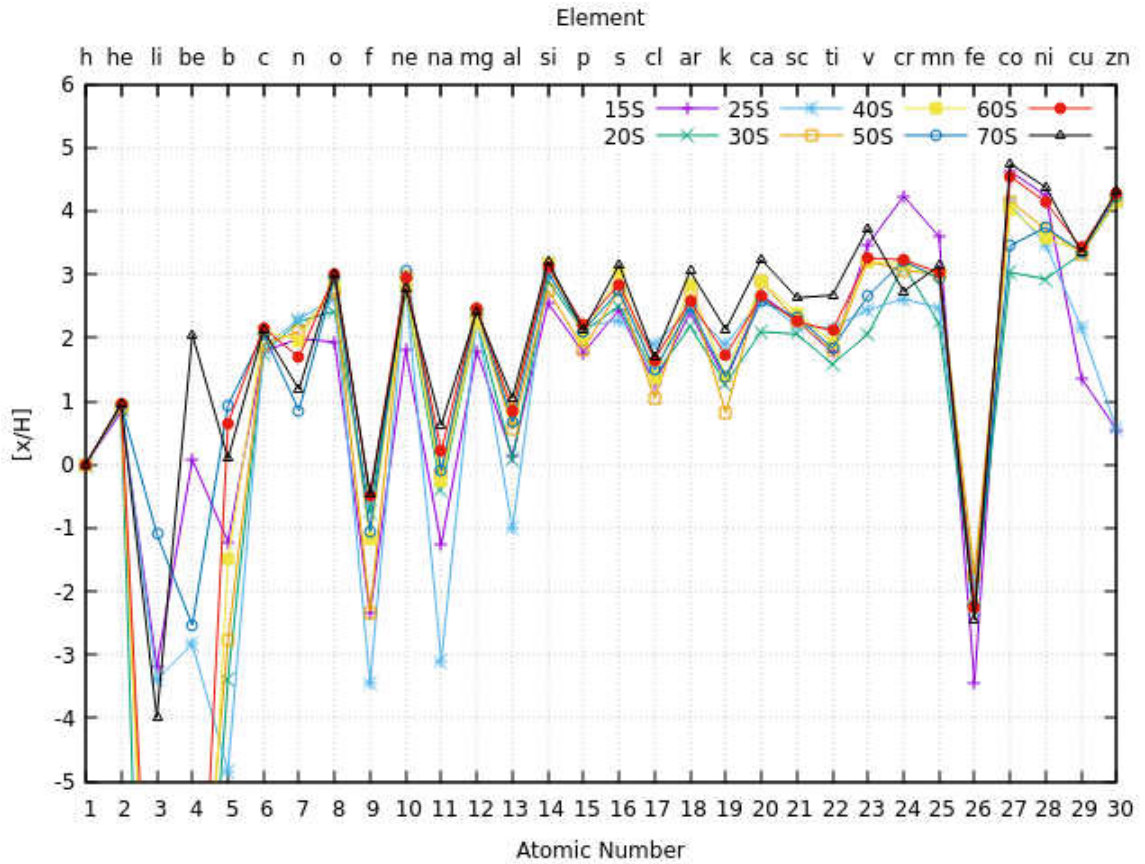
Figure 21. Schwarzschild series [X/H] for $1 > Z > 30$

3.2.2.2 Schwarzschild Models

Figures 27 to 29 show the high energy Schwarzschild series simulated explosion yields. The behavior of the low and high energy Schwarzschild results are not as consistent compared to those of the Ledoux high/low explosion energy results. In the low Z range, $Z < 30$, the trend is similar to that of the Ledoux high and low in that the yields are on average higher as the energy increases. In the low energy regime, the yields dropped off dramatically for most models starting at Zr, or $Z = 40$. The high energy has no consistent high or low drop off or mass-based trends. For the stars with $M < 40M_\odot$, the reduction in yields starts at Gallium, or $Z = 31$, but the yields still maintain an approximate [x/Fe] around -3, much higher than those of the low energy Schwarzschild models. The models
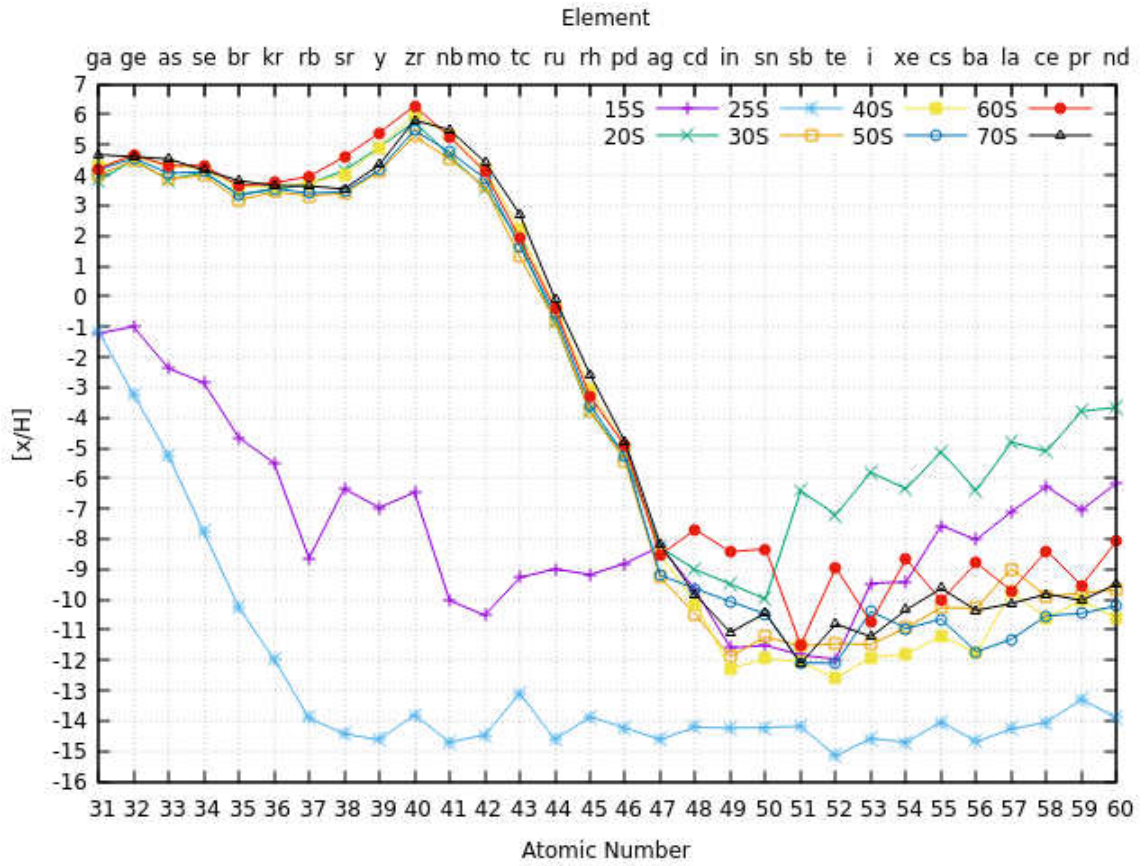
Figure 22. Schwarzschild series [X/H] for $31 > Z > 60$

with $M \geq 40 M_\odot$ are still not consistent with each other. The 70 $M_\odot$ model behaves like the

lower mass models, and the drop off point for the others are spread from lower than Zr up

to Rh.

Figure 23. Schwarzschild series [*X*/*H*] for 61 > Z > 85

Element	15 $M_\odot$	20$M_\odot$	25$M_\odot$	30 $M_\odot$	40 $M_\odot$	50 $M_\odot$	60 $M_\odot$	70 $M_\odot$	80 $M_\odot$
H	-1.876E+00	-2.760E+00	-1.797E+00	-1.404E+00	-1.946E+00	-1.907E+00	-2.455E+00	-1.875E+00	-2.223E+00
He	-1.027E+00	-1.903E+00	-8.991E-01	-4.863E-01	-1.028E+00	-9.851E-01	-1.521E+00	-9.204E-01	-1.278E+00
Li	-1.682E+00	-1.024E+00	-1.302E+00	-8.798E-01	-9.497E-01	-5.653E-01	-3.244E+00	-9.030E-01	-2.525E+00
Be	4.390E-02	-1.999E-01	1.961E+00	2.091E+00	1.523E+00	1.923E+00	-1.986E+00	1.439E+00	-7.004E-01
B	-1.553E+00	-1.608E+00	3.796E-01	6.494E-01	5.587E-01	1.167E-01	-5.920E+00	-1.220E+00	-2.385E+00
C	-2.367E-01	-5.936E-01	4.268E-01	9.807E-01	3.817E-01	3.793E-01	-1.646E+00	4.247E-01	8.752E-02
N	-2.354E+00	-1.055E+00	-1.058E-02	-2.160E+00	-2.938E+00	-1.294E+00	-2.396E+00	2.665E-01	-2.376E+00
O	-5.758E-01	-8.672E-01	4.313E-01	1.006E+00	7.085E-01	8.372E-01	3.761E-01	9.922E-01	6.691E-01
F	-3.531E-01	-3.356E+00	-2.630E+00	-7.889E-01	-2.284E+00	-1.691E+00	-7.205E+00	-2.486E+00	-3.463E+00
Ne	-3.721E-01	-6.347E-01	3.500E-01	5.766E-01	8.653E-01	8.689E-01	3.026E-01	7.682E-01	4.593E-01
Na	-2.066E+00	-4.688E+00	-2.006E+00	-6.867E-01	-1.936E+00	-1.598E+00	-5.365E+00	-1.399E+00	-2.955E+00
Mg	-9.496E-02	-9.844E-01	1.691E-01	6.614E-01	2.996E-01	3.297E-01	-2.826E+00	3.444E-01	9.968E-02
Al	-2.385E+00	-3.145E+00	-1.334E+00	-3.928E-01	-1.278E+00	-1.183E+00	-3.350E+00	-9.404E-01	-1.628E+00
Si	5.895E-01	4.527E-01	8.936E-01	1.330E+00	7.222E-01	7.863E-01	6.016E-01	1.000E+00	7.928E-01
P	-7.227E-01	-3.216E-01	-1.985E-01	5.283E-01	-3.690E-01	-1.510E-01	-6.612E-02	6.148E-03	-8.507E-01
S	5.939E-01	-3.984E-01	7.064E-01	1.340E+00	6.187E-01	8.444E-01	-8.280E-01	1.068E+00	8.462E-01
Cl	-1.976E+00	-9.521E-01	-9.528E-01	-3.377E-01	-9.312E-01	-7.591E-01	-7.002E-01	-6.578E-01	-1.571E+00
Ar	5.195E-01	-6.992E-01	5.038E-01	1.303E+00	6.187E-01	8.138E-01	-1.133E+00	1.027E+00	8.197E-01
K	-2.378E+00	-1.227E+00	-1.165E+00	-3.852E-03	-9.402E-01	-3.605E-01	-1.113E+00	-7.105E-01	-1.451E+00
Ca	7.130E-01	-1.523E+00	6.264E-01	1.520E+00	7.299E-01	1.027E+00	-2.194E+00	1.237E+00	1.051E+00
Sc	-3.947E-01	-6.167E-01	3.826E-01	1.190E+00	2.439E-01	2.912E-01	-9.292E-01	3.758E-01	-3.860E-02
Ti	-7.177E-01	-3.588E-01	-3.496E-01	5.785E-01	-4.051E-01	-5.781E-02	-2.443E-01	1.436E-01	-2.896E-01
V	1.224E+00	2.566E-01	1.197E+00	1.941E+00	1.066E+00	1.342E+00	5.350E-01	1.560E+00	-4.940E-02
Cr	5.175E-01	1.310E+00	1.069E+00	1.535E+00	1.331E+00	1.233E+00	1.040E+00	1.182E+00	2.070E-01
Mn	1.142E+00	3.473E-01	1.137E+00	1.645E+00	7.358E-01	1.069E+00	4.794E-01	1.263E+00	-7.307E-01
Fe	-1.876E+00	-2.760E+00	-1.797E+00	-1.404E+00	-1.946E+00	-1.907E+00	-2.455E+00	-1.875E+00	-2.223E+00
Co	2.261E+00	2.101E-01	2.461E+00	3.167E+00	2.347E+00	2.564E+00	4.603E-01	2.711E+00	1.396E+00
Ni	1.848E+00	1.308E-01	2.070E+00	2.720E+00	1.899E+00	2.220E+00	-9.272E-01	2.287E+00	2.155E+00
Cu	1.097E-01	-1.995E-01	1.451E+00	1.580E+00	1.360E+00	1.308E+00	-2.414E+00	1.502E+00	1.506E+00
Zn	8.729E-01	8.346E-01	2.220E+00	2.454E+00	2.160E+00	2.203E+00	-4.221E+00	2.355E+00	2.466E+00
Ga	9.879E-01	-2.020E-01	2.074E+00	2.377E+00	1.965E+00	2.040E+00	-6.408E+00	2.218E+00	1.634E+00
Ge	1.483E+00	4.872E-01	2.506E+00	2.873E+00	2.524E+00	2.498E+00	-8.529E+00	2.714E+00	2.229E+00
As	1.598E+00	-5.033E-01	1.993E+00	2.731E+00	2.074E+00	2.172E+00	-1.076E+01	2.295E+00	1.810E+00
Se	1.477E+00	-9.148E-01	2.060E+00	2.631E+00	2.162E+00	2.176E+00	-1.287E+01	2.350E+00	1.781E+00
Br	1.362E+00	-2.065E+00	1.320E+00	2.348E+00	1.508E+00	1.701E+00	-1.516E+01	1.675E+00	1.352E+00
Kr	1.118E+00	-2.308E+00	1.499E+00	2.049E+00	1.597E+00	1.557E+00	-1.478E+01	1.753E+00	1.201E+00
Rb	2.116E+00	-3.374E+00	1.529E+00	2.737E+00	1.827E+00	2.135E+00	-1.530E+01	2.018E+00	1.542E+00
Sr	4.244E+00	-2.856E+00	1.569E+00	4.234E+00	2.429E+00	3.384E+00	-1.696E+01	2.740E+00	2.242E+00
Y	3.981E+00	-3.487E+00	2.351E+00	4.553E+00	3.204E+00	3.879E+00	-1.718E+01	3.493E+00	3.050E+00
Zr	3.598E+00	-2.735E+00	3.457E+00	4.737E+00	4.041E+00	4.278E+00	-1.698E+01	4.309E+00	3.894E+00
Nb	1.984E+00	-2.140E+00	2.671E+00	3.353E+00	3.018E+00	2.969E+00	-1.673E+01	3.206E+00	3.097E+00
Mo	6.117E-01	-1.555E+00	1.698E+00	2.216E+00	1.952E+00	1.627E+00	-1.673E+01	2.029E+00	1.697E+00
Tc	-1.313E+00	-3.498E+00	-5.185E-01	2.753E+00	2.084E+00	-4.861E-01	-1.515E+01	-2.082E-01	5.553E-01
Ru	-3.891E+00	-5.507E+00	-2.725E+00	2.324E+00	1.159E+00	-2.890E+00	-1.682E+01	-2.521E+00	-1.502E+00
Rh	-6.491E+00	-9.034E+00	-5.515E+00	2.314E+00	1.630E+00	-5.653E+00	-1.594E+01	-5.403E+00	-9.146E-01
Pd	-7.632E+00	-1.025E+01	-6.251E+00	2.741E+00	1.866E+00	-6.392E+00	-1.651E+01	-6.196E+00	-9.630E-01
Ag	-9.878E+00	-1.102E+01	-6.282E+00	2.926E+00	2.094E+00	-6.449E+00	-1.627E+01	-6.367E+00	-9.169E-01
Cd	-1.075E+01	-1.098E+01	-6.526E+00	2.653E+00	1.617E+00	-5.983E+00	-1.666E+01	-6.446E+00	-9.662E-01
In	-1.157E+01	-1.135E+01	-7.006E+00	2.201E+00	1.336E+00	-6.302E+00	-1.592E+01	-7.142E+00	-1.985E-01
Sn	-1.091E+01	-1.071E+01	-6.366E+00	2.970E+00	2.010E+00	-5.971E+00	-1.681E+01	-6.451E+00	-1.545E+00
Sb	-9.152E+00	-1.247E+01	-6.023E+00	3.484E+00	2.238E+00	-5.708E+00	-1.610E+01	-6.161E+00	-1.421E+00
Te	-8.358E+00	-1.104E+01	-6.836E+00	3.500E+00	2.101E+00	-6.816E+00	-1.718E+01	-6.948E+00	-3.054E+00
I	-7.851E+00	-1.149E+01	-6.485E+00	3.826E+00	2.499E+00	-6.345E+00	-1.657E+01	-6.513E+00	-3.745E+00
Xe	-8.942E+00	-1.044E+01	-7.800E+00	3.194E+00	1.700E+00	-6.864E+00	-1.700E+01	-8.138E+00	-3.590E+00
Cs	-9.240E+00	-9.799E+00	-7.897E+00	3.837E+00	2.458E+00	-5.969E+00	-1.603E+01	-8.610E+00	-3.073E+00
Ba	-1.240E+01	-9.586E+00	-1.064E+01	2.534E+00	7.494E-01	-6.927E+00	-1.695E+01	-1.261E+01	-4.016E+00
La	-1.151E+01	-7.422E+00	-1.047E+01	2.814E+00	1.407E+00	-4.552E+00	-1.633E+01	-1.104E+01	-3.311E+00
Ce	-1.107E+01	-7.888E+00	-8.087E+00	2.818E+00	1.620E+00	-5.582E+00	-1.639E+01	-1.168E+01	-3.412E+00
Pr	-1.035E+01	-5.258E+00	-8.387E+00	2.653E+00	1.634E+00	-5.429E+00	-1.541E+01	-1.084E+01	-2.794E+00
Nd	-1.090E+01	-6.466E+00	-5.311E+00	3.060E+00	1.720E+00	-5.102E+00	-1.628E+01	-1.052E+01	-3.244E+00
Pm	-9.815E+00	-3.913E+00	-5.389E+00	3.774E+00	2.606E+00	-3.646E+00	-1.444E+01	-9.725E+00	-2.060E+00
Sm	-1.046E+01	-5.376E+00	-2.862E+00	3.438E+00	2.514E+00	-3.979E+00	-1.542E+01	-1.016E+01	-2.769E+00
Eu	-1.027E+01	-5.642E+00	-3.181E+00	3.794E+00	3.012E+00	-3.145E+00	-1.532E+01	-9.679E+00	-2.666E+00
Gd	-1.050E+01	-6.599E+00	-5.610E+00	3.637E+00	2.581E+00	-3.516E+00	-1.570E+01	-9.774E+00	-2.942E+00
Tb	-9.451E+00	-4.240E+00	-4.795E+00	4.055E+00	3.166E+00	-3.099E+00	-1.508E+01	-9.229E+00	-2.428E+00
Dy	-1.030E+01	-4.573E+00	-3.325E+00	3.887E+00	2.889E+00	-2.510E+00	-1.592E+01	-9.875E+00	-3.008E+00
Ho	-1.095E+01	-4.666E+00	-4.899E+00	3.987E+00	3.114E+00	-2.091E+00	-1.524E+01	-1.015E+01	-2.575E+00
Er	-1.082E+01	-4.769E+00	-3.073E+00	4.189E+00	2.946E+00	-2.044E+00	-1.569E+01	-9.768E+00	-2.590E+00
Tm	-1.016E+01	-4.468E+00	-2.770E+00	4.500E+00	3.547E+00	-2.004E+00	-1.500E+01	-9.278E+00	-1.908E+00
Yb	-1.122E+01	-5.449E+00	-2.719E+00	4.209E+00	3.203E+00	-2.008E+00	-1.558E+01	-9.787E+00	-2.300E+00
Lu	-1.068E+01	-4.059E+00	-3.561E+00	4.490E+00	3.384E+00	-1.640E+00	-1.479E+01	-9.929E+00	-1.932E+00
Hf	-1.143E+01	-5.499E+00	-5.217E+00	4.668E+00	3.602E+00	-1.206E+00	-1.548E+01	-9.954E+00	-2.315E+00
Ta	-1.148E+01	-5.337E+00	-7.613E+00	4.834E+00	3.942E+00	-1.166E+00	-1.479E+01	-1.054E+01	-2.323E+00
W	-1.206E+01	-6.538E+00	-8.825E+00	4.883E+00	3.736E+00	-1.480E+00	-1.561E+01	-1.015E+01	-3.296E+00
Re	-1.106E+01	-5.622E+00	-8.698E+00	4.250E+00	3.109E+00	-2.214E+00	-1.450E+01	-1.037E+01	-3.888E+00
Os	-1.173E+01	-6.509E+00	-9.493E+00	4.126E+00	2.938E+00	-2.689E+00	-1.643E+01	-1.132E+01	-4.986E+00
Ir	-1.312E+01	-7.512E+00	-9.699E+00	3.328E+00	2.220E+00	-3.801E+00	-1.632E+01	-1.205E+01	-5.304E+00
Pt	-9.583E+00	-7.946E+00	-5.687E+00	4.649E+00	3.064E+00	-2.768E+00	-1.600E+01	-1.005E+01	-5.450E+00
Au	-8.786E+00	-7.419E+00	-4.822E+00	4.624E+00	3.184E+00	-2.620E+00	-1.550E+01	-1.104E+01	-4.693E+00
Hg	-9.906E+00	-7.965E+00	-6.652E+00	4.824E+00	3.117E+00	-2.926E+00	-1.563E+01	-9.630E+00	-4.810E+00
Tl	-9.739E+00	-7.953E+00	-8.324E+00	3.861E+00	2.234E+00	-3.828E+00	-1.543E+01	-1.067E+01	-4.630E+00
Pb	-1.004E+01	-8.121E+00	-4.697E+00	3.256E+00	1.840E+00	-5.295E+00	-1.641E+01	-1.039E+01	-5.769E+00
Bi	-9.152E+00	-7.118E+00	-1.536E+00	5.597E+00	4.007E+00	-3.909E+00	-1.526E+01	-8.688E+00	-3.414E+00
Po	-5.638E+00	-4.651E+00	4.551E-01	5.903E+00	4.673E+00	-4.106E+00	-1.448E+01	-8.310E+00	-5.241E+00
At	-1.581E+01	-1.433E+01	-1.549E+01	-1.466E+01	-1.493E+01	-1.412E+01	-1.603E+01	-1.563E+01	-1.581E+01

Table 5. The final abundance values of the Ledoux series in [X/Fe] form for the low energy explosion with just the degenerate iron core removed

Element	15 $M_\odot$	20$M_\odot$	25$M_\odot$	30 $M_\odot$	40 $M_\odot$	50 $M_\odot$	60 $M_\odot$	70 $M_\odot$
H	-3.441E+00	-2.271E+00	-1.953E+00	-1.743E+00	-2.230E+00	-2.220E+00	-2.257E+00	-2.454E+00
He	-2.616E+00	-1.388E+00	-1.063E+00	-8.401E-01	-1.287E+00	-1.283E+00	-1.309E+00	-1.498E+00
Li	-6.627E+00	-1.977E+01	-5.347E+00	-1.346E+00	-1.431E+00	-3.318E+00	-1.259E+01	-6.452E+00
Be	-3.361E+00	-1.336E+01	-4.788E+00	-1.084E+01	-1.445E+01	-4.758E+00	-1.279E+01	-4.030E-01
B	-4.662E+00	-5.657E+00	-6.792E+00	-4.521E+00	-3.721E+00	-1.286E+00	-1.606E+00	-2.362E+00
C	-1.653E+00	-5.176E-01	-1.055E+00	1.498E+00	-1.268E+00	-1.546E+01	-1.032E-01	-3.394E-01
N	-1.457E+00	-1.583E-02	3.428E-01	3.570E-01	-2.671E-01	-1.371E+00	-5.686E-01	-1.269E+00
O	-1.510E+00	1.462E-01	6.651E-01	9.784E-01	6.431E-01	7.265E-01	7.402E-01	5.640E-01
F	-5.791E+00	-3.006E+00	-5.407E+00	-4.069E+01	-3.406E+00	-3.271E+00	-2.755E+00	-2.930E+00
Ne	-1.633E+00	4.380E-01	8.849E-01	1.236E+00	5.332E-01	8.343E-01	6.783E-01	3.238E-01
Na	-4.704E+00	-2.679E+00	-5.060E+00	-1.889E+00	-2.509E+00	-2.311E+00	-2.046E+00	-1.835E+00
Mg	-1.650E+00	-1.628E-02	3.611E-01	6.529E-01	5.674E-03	2.473E-01	2.214E-01	-3.638E-02
Al	-3.313E+00	-2.186E+00	-2.969E+00	-1.186E+00	-1.347E+00	-1.552E+00	-1.407E+00	-1.407E+00
Si	-8.938E-01	6.288E-01	1.209E+00	1.014E+00	9.410E-01	8.168E-01	8.684E-01	7.493E-01
P	-1.676E+00	-1.788E-01	-2.162E-01	7.481E-02	-2.162E-01	-1.125E-01	-5.171E-02	-3.402E-01
S	-1.000E+00	2.317E-01	3.254E-01	1.014E+00	7.993E-01	5.209E-01	5.868E-01	7.006E-01
Cl	-2.165E+00	-8.708E-01	-5.864E-02	-7.062E-01	-8.698E-01	-7.300E-01	-6.047E-01	-7.688E-01
Ar	-1.038E+00	-9.252E-02	4.843E-01	9.508E-01	5.902E-01	2.642E-01	3.270E-01	5.941E-01
K	-2.121E+00	-9.931E-01	-6.122E-01	-9.252E-01	-8.563E-01	-8.428E-01	-5.324E-01	-3.235E-01
Ca	-7.656E-01	-1.778E-01	6.633E-01	1.143E+00	6.627E-01	3.560E-01	3.939E-01	7.832E-01
Sc	-1.176E+00	-2.149E-01	2.193E-01	5.255E-01	1.601E-01	1.023E-01	-3.889E-03	1.724E-01
Ti	-1.671E+00	-6.867E-01	1.995E-01	5.400E-02	-3.065E-01	-3.808E-01	-1.466E-01	2.152E-01
V	2.913E-02	-2.170E-01	4.876E-01	1.461E+00	9.688E-01	4.358E-01	9.973E-01	1.269E+00
Cr	7.904E-01	8.680E-01	6.617E-01	1.322E+00	9.323E-01	9.911E-01	9.732E-01	2.751E+00
Mn	1.574E-01	-4.729E-02	5.164E-01	1.252E+00	7.476E-01	7.142E-01	7.715E-01	6.800E-01
Fe	-3.441E+00	-2.271E+00	-1.953E+00	-1.743E+00	-2.230E+00	-2.220E+00	-2.257E+00	-2.454E+00
Co	1.184E+00	7.598E-01	2.150E+00	2.409E+00	1.803E+00	1.231E+00	2.289E+00	2.288E+00
Ni	8.017E-01	6.530E-01	1.512E+00	1.971E+00	1.334E+00	1.518E+00	1.880E+00	1.919E+00
Cu	-2.078E+00	1.048E+00	2.044E-01	1.585E+00	1.142E+00	1.136E+00	1.162E+00	8.968E-01
Zn	-2.900E+00	1.889E+00	-1.404E+00	2.426E+00	1.909E+00	2.016E+00	2.020E+00	1.869E+00
Ga	-4.667E+00	1.536E+00	-3.094E+00	2.256E+00	2.074E+00	1.963E+00	1.955E+00	2.221E+00
Ge	-4.437E+00	2.219E+00	-5.187E+00	2.716E+00	2.330E+00	2.329E+00	2.412E+00	2.148E+00
As	-5.824E+00	1.583E+00	-7.212E+00	2.124E+00	2.097E+00	1.847E+00	2.047E+00	2.078E+00
Se	-6.286E+00	1.818E+00	-9.725E+00	2.256E+00	1.960E+00	1.884E+00	2.070E+00	1.706E+00
Br	-8.102E+00	1.097E+00	-1.221E+01	1.433E+00	1.383E+00	1.119E+00	1.391E+00	1.358E+00
Kr	-8.931E+00	1.238E+00	-1.391E+01	1.700E+00	1.378E+00	1.337E+00	1.483E+00	1.189E+00
Rb	-1.208E+01	1.433E+00	-1.586E+01	1.579E+00	1.512E+00	1.175E+00	1.699E+00	1.180E+00
Sr	-9.789E+00	1.885E+00	-1.638E+01	1.650E+00	1.779E+00	1.238E+00	2.341E+00	1.094E+00
Y	-1.041E+01	2.640E+00	-1.657E+01	2.376E+00	2.661E+00	1.951E+00	3.133E+00	1.884E+00
Zr	-9.910E+00	3.487E+00	-1.575E+01	3.546E+00	3.796E+00	3.257E+00	4.027E+00	3.358E+00
Nb	-1.347E+01	2.380E+00	-1.665E+01	2.774E+00	3.081E+00	2.541E+00	3.009E+00	3.041E+00
Mo	-1.396E+01	1.284E+00	-1.641E+01	1.894E+00	1.963E+00	1.668E+00	1.858E+00	1.982E+00
Tc	-1.271E+01	-4.506E-01	-1.505E+01	-4.370E-01	-3.496E-02	-5.665E-01	-3.553E-01	2.533E-01
Ru	-1.242E+01	-3.114E+00	-1.656E+01	-2.555E+00	-2.602E+00	-2.818E+00	-2.672E+00	-2.532E+00
Rh	-1.262E+01	-6.068E+00	-1.582E+01	-5.552E+00	-5.289E+00	-5.806E+00	-5.559E+00	-5.036E+00
Pd	-1.225E+01	-7.559E+00	-1.618E+01	-7.169E+00	-7.209E+00	-7.493E+00	-7.194E+00	-7.255E+00
Ag	-1.169E+01	-1.054E+01	-1.657E+01	-1.101E+01	-1.073E+01	-1.141E+01	-1.078E+01	-1.062E+01
Cd	-1.312E+01	-1.128E+01	-1.616E+01	-1.223E+01	-1.234E+01	-1.186E+01	-9.953E+00	-1.230E+01
In	-1.503E+01	-1.176E+01	-1.618E+01	-1.363E+01	-1.451E+01	-1.228E+01	-1.068E+01	-1.353E+01
Sn	-1.495E+01	-1.226E+01	-1.617E+01	-1.297E+01	-1.417E+01	-1.269E+01	-1.058E+01	-1.289E+01
Sb	-1.527E+01	-8.686E+00	-1.613E+01	-1.327E+01	-1.429E+01	-1.431E+01	-1.375E+01	-1.456E+01
Te	-1.540E+01	-9.476E+00	-1.711E+01	-1.320E+01	-1.482E+01	-1.431E+01	-1.121E+01	-1.326E+01
I	-1.290E+01	-8.084E+00	-1.653E+01	-1.322E+01	-1.413E+01	-1.261E+01	-1.300E+01	-1.368E+01
Xe	-1.286E+01	-8.621E+00	-1.666E+01	-1.267E+01	-1.404E+01	-1.317E+01	-1.092E+01	-1.280E+01
Cs	-1.100E+01	-7.397E+00	-1.599E+01	-1.201E+01	-1.342E+01	-1.287E+01	-1.229E+01	-1.208E+01
Ba	-1.147E+01	-8.669E+00	-1.663E+01	-1.202E+01	-1.399E+01	-1.394E+01	-1.104E+01	-1.281E+01
La	-1.054E+01	-7.089E+00	-1.622E+01	-1.072E+01	-1.197E+01	-1.353E+01	-1.196E+01	-1.259E+01
Ce	-9.722E+00	-7.380E+00	-1.600E+01	-1.163E+01	-1.284E+01	-1.275E+01	-1.064E+01	-1.227E+01
Pr	-1.047E+01	-6.063E+00	-1.524E+01	-1.153E+01	-1.225E+01	-1.267E+01	-1.179E+01	-1.248E+01
Nd	-9.598E+00	-5.932E+00	-1.586E+01	-1.141E+01	-1.284E+01	-1.242E+01	-1.031E+01	-1.194E+01
Pm	-8.779E+00	-4.537E+00	-1.447E+01	-1.073E+01	-1.145E+01	-1.142E+01	-1.073E+01	-1.154E+01
Sm	-8.624E+00	-5.458E+00	-1.498E+01	-1.064E+01	-1.215E+01	-1.159E+01	-9.984E+00	-1.155E+01
Eu	-8.327E+00	-6.017E+00	-1.543E+01	-1.062E+01	-1.260E+01	-1.227E+01	-1.194E+01	-1.221E+01
Gd	-9.273E+00	-7.138E+00	-1.573E+01	-9.865E+00	-1.277E+01	-1.208E+01	-1.192E+01	-1.245E+01
Tb	-8.885E+00	-7.264E+00	-1.524E+01	-8.617E+00	-1.193E+01	-1.185E+01	-1.148E+01	-1.189E+01
Dy	-9.958E+00	-9.073E+00	-1.603E+01	-1.057E+01	-1.245E+01	-1.178E+01	-1.149E+01	-1.220E+01
Ho	-1.000E+01	-9.719E+00	-1.540E+01	-1.071E+01	-1.247E+01	-1.199E+01	-1.154E+01	-1.213E+01
Er	-1.039E+01	-1.049E+01	-1.575E+01	-1.028E+01	-1.163E+01	-1.120E+01	-1.105E+01	-1.178E+01
Tm	-1.017E+01	-1.052E+01	-1.514E+01	-1.054E+01	-1.181E+01	-1.163E+01	-1.130E+01	-1.190E+01
Yb	-9.805E+00	-1.077E+01	-1.556E+01	-9.764E+00	-1.174E+01	-1.207E+01	-1.166E+01	-1.156E+01
Lu	-1.003E+01	-4.962E+00	-1.489E+01	-8.136E+00	-1.134E+01	-1.159E+01	-1.078E+01	-1.078E+01
Hf	-9.555E+00	-5.874E+00	-1.548E+01	-8.766E+00	-1.090E+01	-1.196E+01	-1.137E+01	-1.159E+01
Ta	-7.538E+00	-4.540E+00	-1.475E+01	-1.079E+01	-1.131E+01	-1.238E+01	-1.167E+01	-1.217E+01
W	-7.725E+00	-4.000E+00	-1.549E+01	-1.106E+01	-1.178E+01	-1.016E+01	-1.033E+01	-1.140E+01
Re	-8.049E+00	-3.235E+00	-1.439E+01	-9.813E+00	-1.155E+01	-1.166E+01	-1.216E+01	-1.134E+01
Os	-8.464E+00	-4.518E+00	-1.628E+01	-1.202E+01	-1.317E+01	-1.262E+01	-1.326E+01	-1.324E+01
Ir	-8.806E+00	-4.332E+00	-1.606E+01	-1.275E+01	-1.403E+01	-1.405E+01	-1.392E+01	-1.406E+01
Pt	-8.552E+00	-4.580E+00	-1.585E+01	-1.139E+01	-1.305E+01	-1.013E+01	-1.053E+01	-1.161E+01
Au	-8.325E+00	-3.895E+00	-1.537E+01	-1.198E+01	-1.292E+01	-1.275E+01	-1.284E+01	-1.303E+01
Hg	-8.063E+00	-3.529E+00	-1.575E+01	-1.064E+01	-1.256E+01	-9.863E+00	-1.016E+01	-1.132E+01
Tl	-8.937E+00	-3.278E+00	-1.523E+01	-1.119E+01	-1.241E+01	-1.173E+01	-1.105E+01	-1.164E+01
Pb	-7.551E+00	-5.222E+00	-1.619E+01	-1.102E+01	-1.314E+01	-1.225E+01	-1.131E+01	-1.166E+01
Bi	-7.219E+00	-1.953E+00	-1.500E+01	-6.657E+00	-1.168E+01	-8.284E+00	-7.841E+00	-6.139E+00
Po	-6.200E+00	-1.176E+00	-1.436E+01	-8.282E+00	-1.044E+01	-8.567E+00	-8.400E+00	-7.751E+00
At	-1.689E+01	-1.666E+01	-1.644E+01	-1.557E+01	-1.461E+01	-1.566E+01	-1.637E+01	-1.610E+01

Table 6. The final abundance values of the Schwarzschild series in [X/Fe] form for the low energy explosion with just the degenerate iron core removed

53

Figure 24. High energy Ledoux series [X/H] for $1 > Z > 30$

Figure 25. High energy Ledoux series $[X/H]$ for $31 > Z > 60$

Figure 26. High energy Ledoux series $[X/H]$ for $61 > Z > 85$
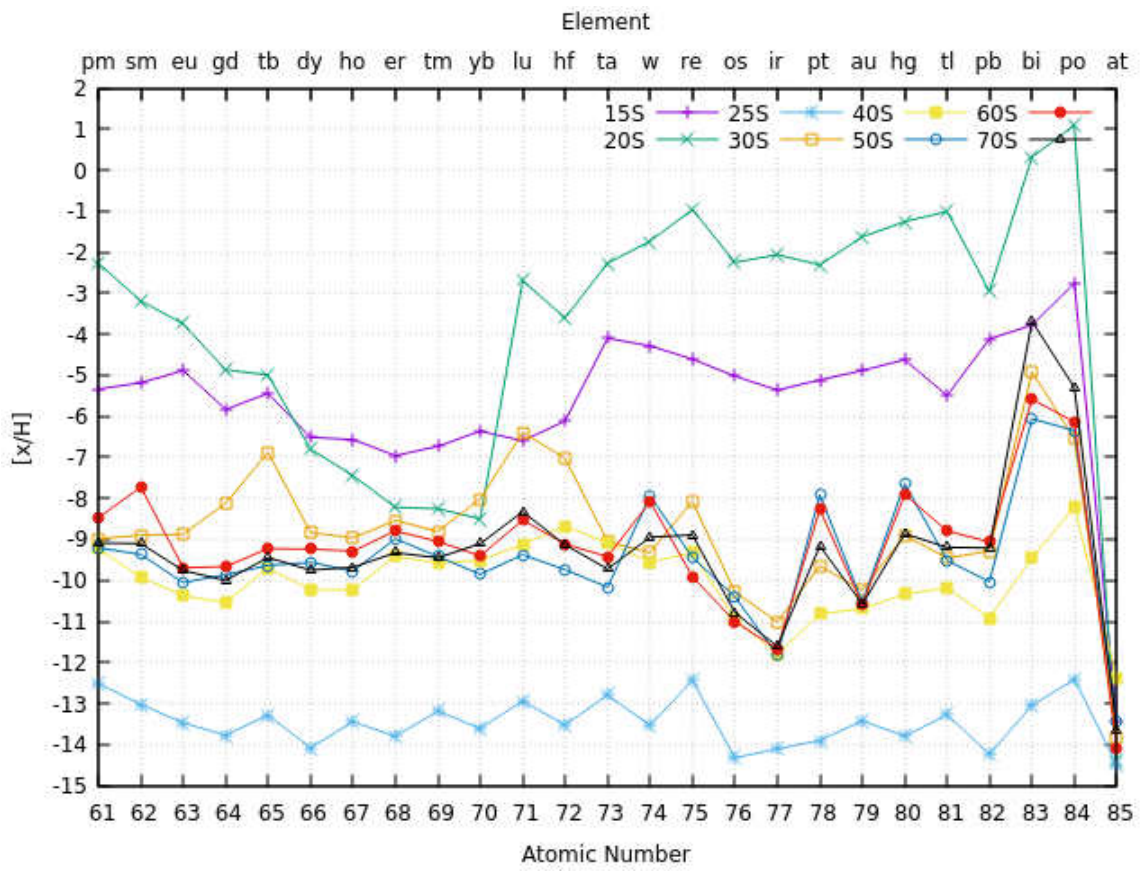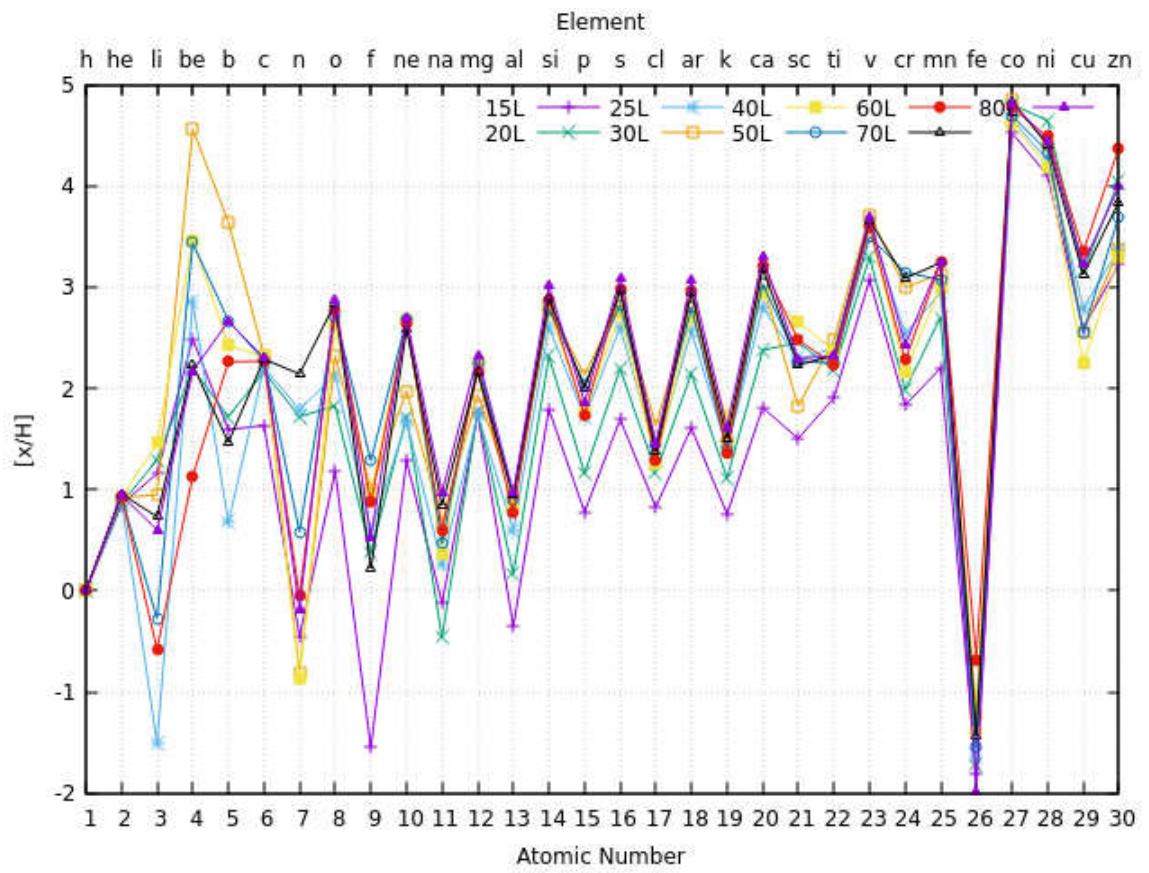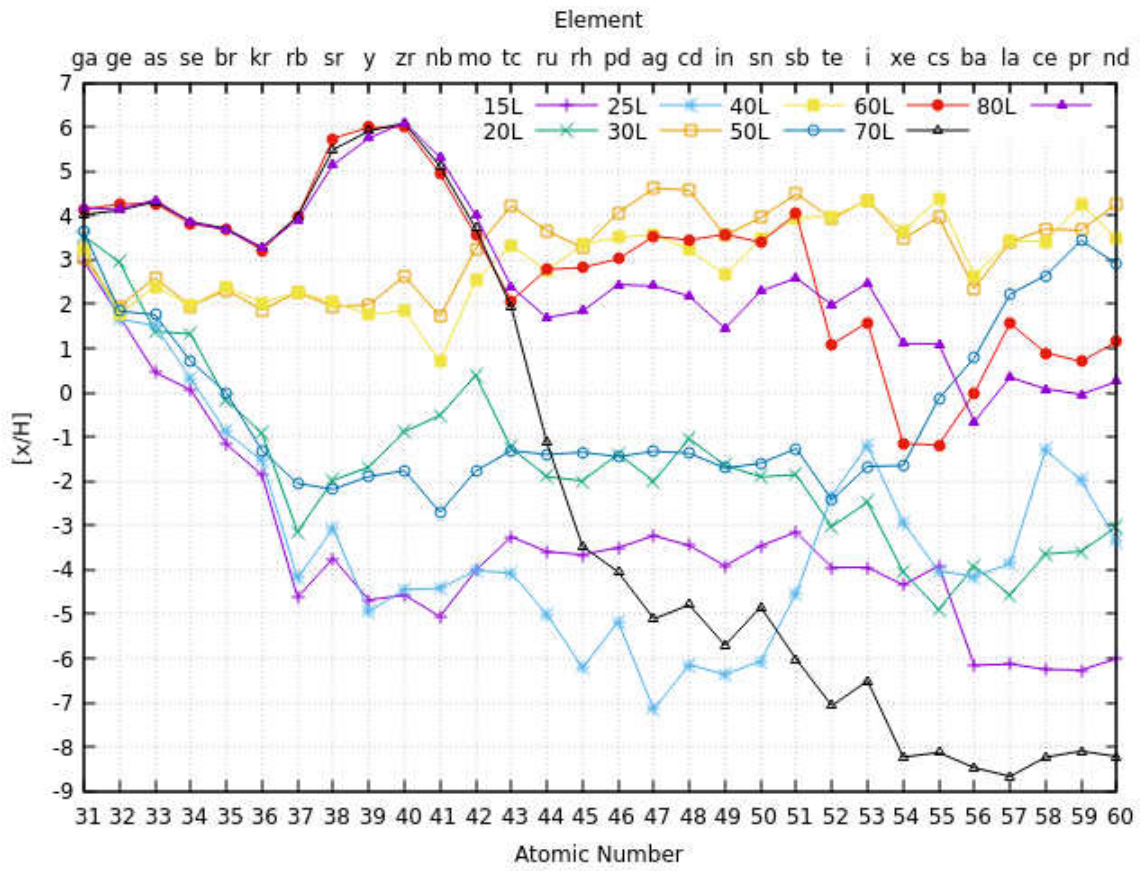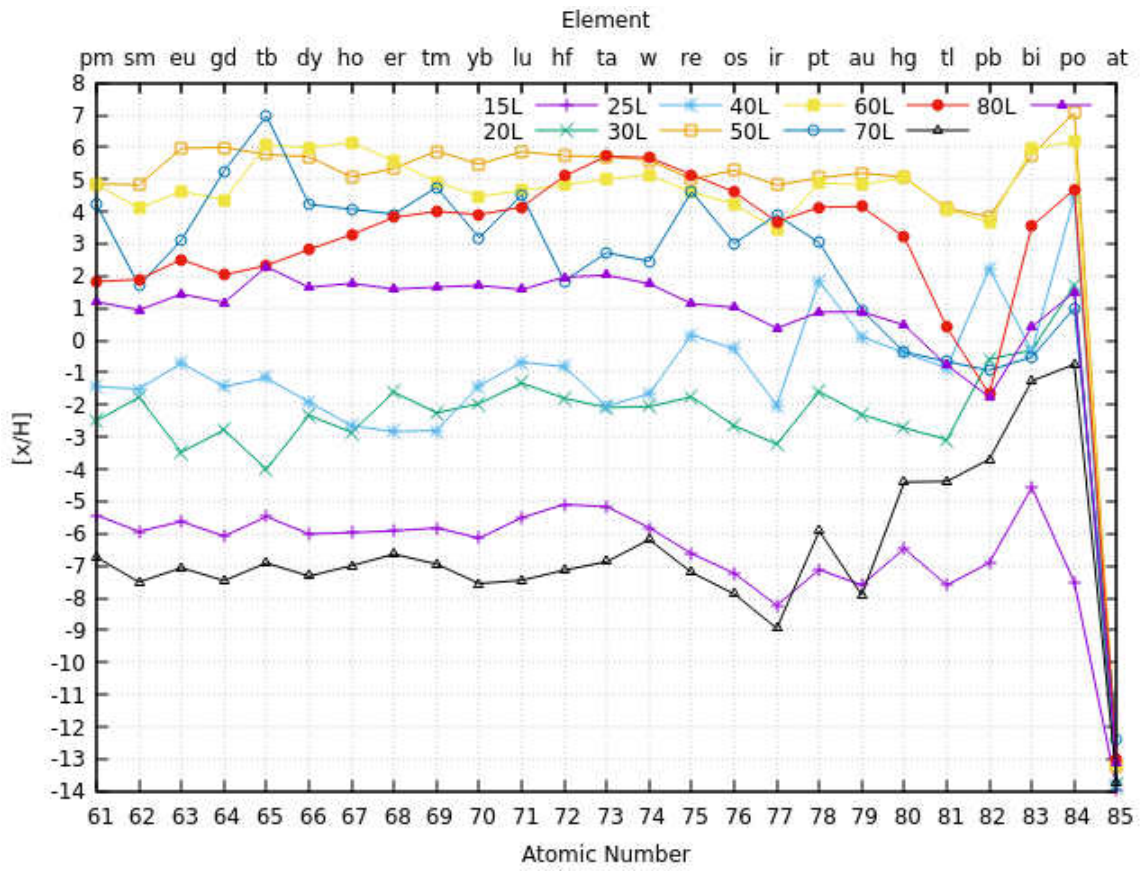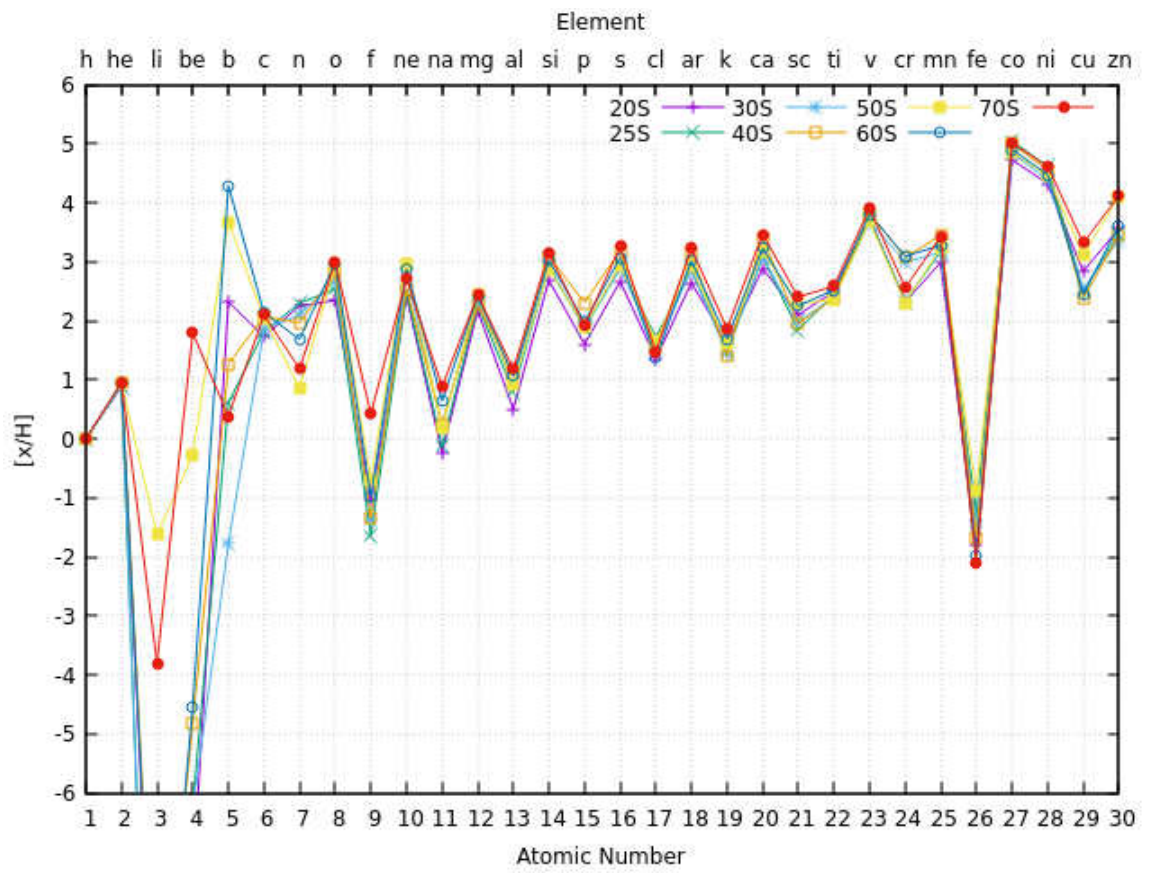
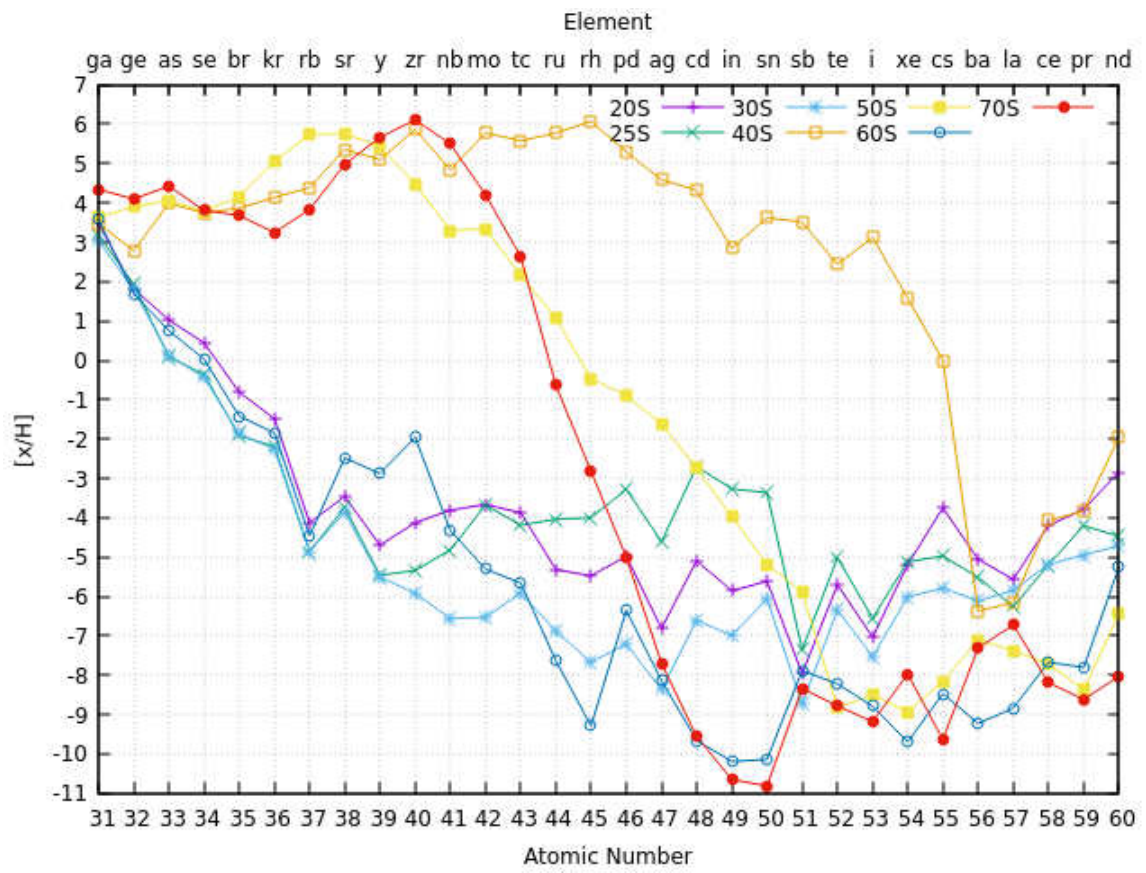Figure 27. High energy Schwarzschild series $[X/H]$ for $1 > Z > 30$

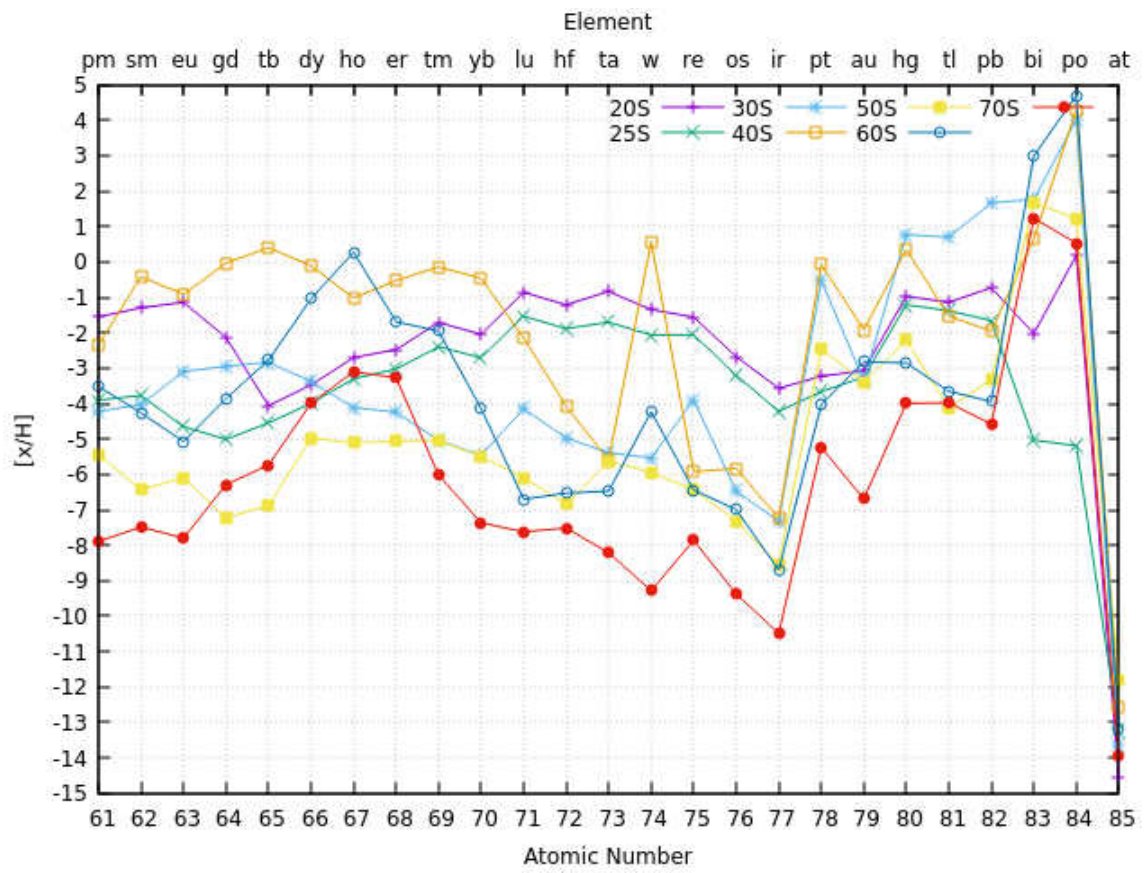Figure 28. High energy Schwarzschild series [X/H] for $31 > Z > 60$

Figure 29. High energy Schwarzschild series [X/H] for $61 > Z > 85$

CHAPTER 4

Analysis and Discussion

4.1 Population III Supernovae

As presented in Chapter 3, the lightcurves of the Ledoux and Schwarzschild supernovae

for both high and low explosion energies are shown as luminosity versus time. From an

observational perspective, the lightcurve and the spectra together are the best tools to

analyze CCSNe. Spectral synthesis is beyond the scope of this work and work done here

is from analyzing the light curves. From the light curve, methods to calculate the SN

explosion energy by fitting simple semi-analytic models are often used (Nagy & Vinkó,

2016; Chatzopoulos et al., 2012; Arnett, 1980) as well as tools to determine the nickel

abundance (Arnett, 1996; Nagy et al., 2014). Abundances of elements, either from the

progenitor star or the nucleosynthesis can only be observationally determined from

spectral analysis, as well as classifying the SNe. Comparisons of the Ledoux to that of

SN1987a will be discussed as well as method of exploring the explodeability parameter of

stellar models used in CCSNe studies.

4.1.1 Nickel

Figure 30 shows the nickel yields from the high and low explosion energy series. Nickel is

the primary energy source for the latetime lightcurve as discussed in section 2.2.2. Nickel

masses can be measured using observational methods by using the tail luminosity (Arnett,

1996). The SN light curve tails in section 3.1.3 might be difficult to observe or even

detect. With no observed population III CCSNe, there exists no direct observational constraints on possible nickel masses. Looking at observed values for ejected M_{Ni} in Mller et al. (2017), the majority of measured nickel abundances give an ejected mass of less then .12 $M_\odot$. These are normal Type II CCSNe, and as such have energies near 1×10^{51} ergs, but considering superluminous supernovae (Nicholl et al., 2014), these can require greater than 1 $M_\odot$ of nickel being produced to account for the very bright light curve. It is argued there could be other factors giving these bright supernovae high luminosity, such as an optically thick and large circumstellar region or the formation of a magnetar as the central remnant (Kasen & Bildsten, 2010). Figure 30 shows a correlation
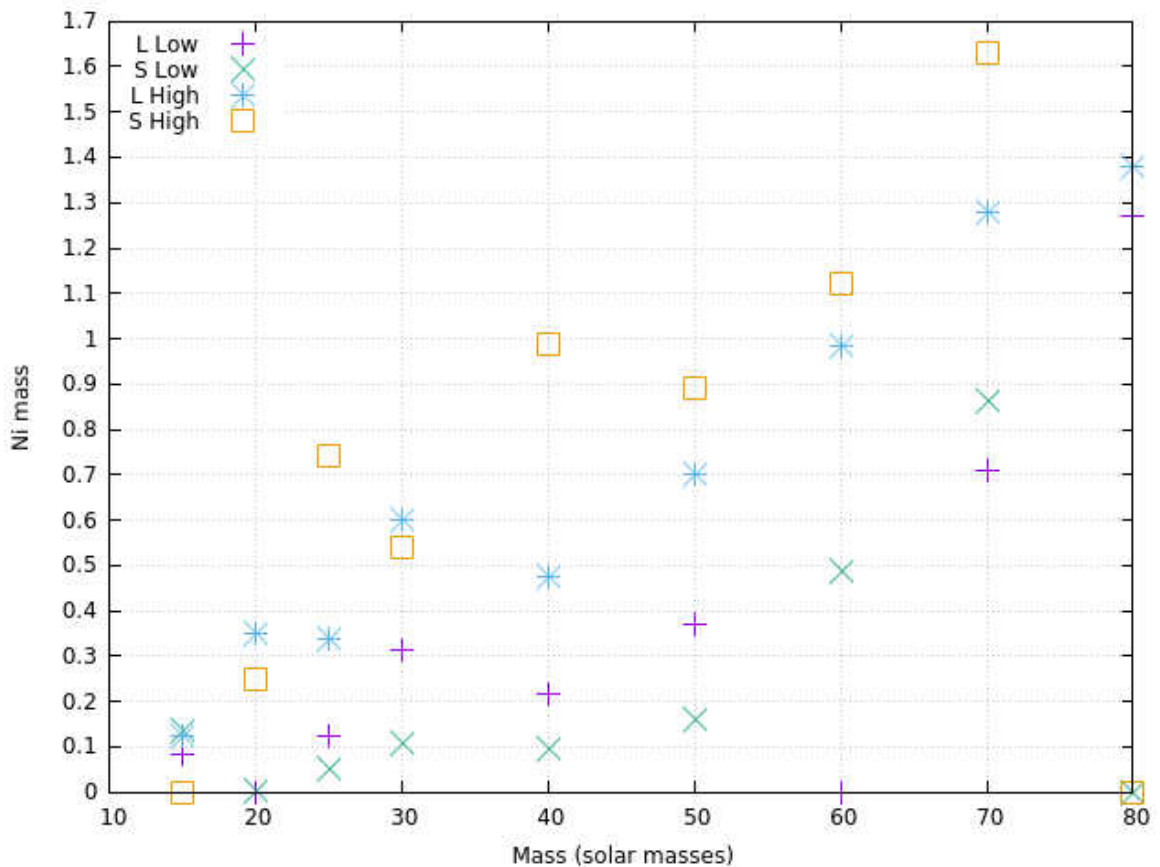
Figure 30. With only the degenerate iron core removed, this is the plotted yields of Nickel 56 as a function of M_{ZAMS}, where ZAMS is zero age main sequence.

between the energy of the explosion and the production of nickel. This behavior is not

linear nor is it consistent between low and high energy and convection criteria. Looking at

only the high energy series, in which the energy is 10×10^{51} ergs $\pm .2 \times 10^{51}$ ergs, the

yields of nickel increase as the mass of the progenitor increases, but not uniformly.

Between the L/S series, the lower energy Ledoux produces, on average, more nickel while

the higher energy Schwarzschild on average produces more nickel.
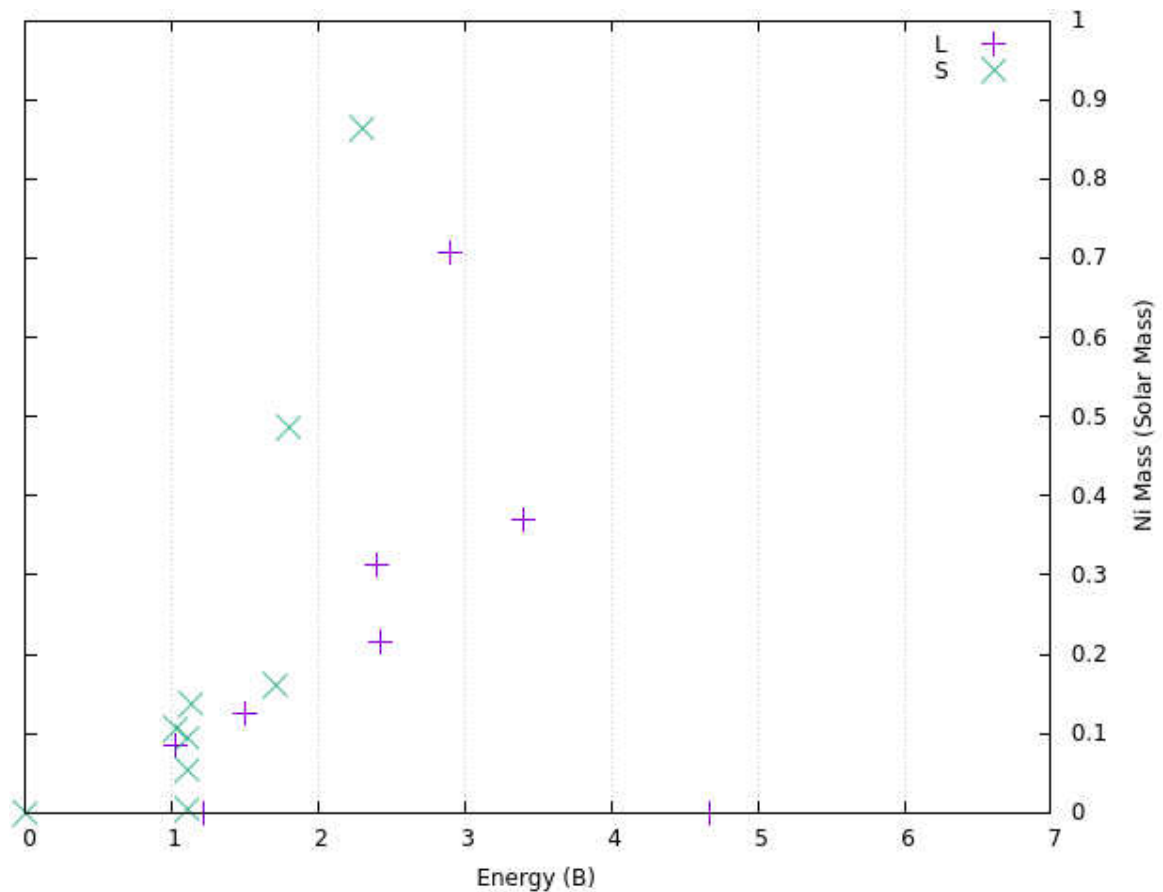
Figure 31. With only the degenerate iron core removed, this is the plotted yields of Nickel 56 as a function of explosion energy for only the low energy series.

Considering only the low energy series in figure 31, the SNe in the 1×10^{51} ergs

area produce nickel yields consistent with that presented by (Mller et al., 2017) in the

$.05 - .12 \ M_\odot$ range. The Schwarzschild series has a steeper dependence to the increase in

energy, exemplified by a 2.5×10^{51} ergs explosion and the nickel production approaching

.9 $M_{\odot}$. In contrast the three Ledoux models with $E_{explosion} > 2.5 \times 10^{51}$ ergs produce less

than $0.5 M_{\odot}$ of nickel.
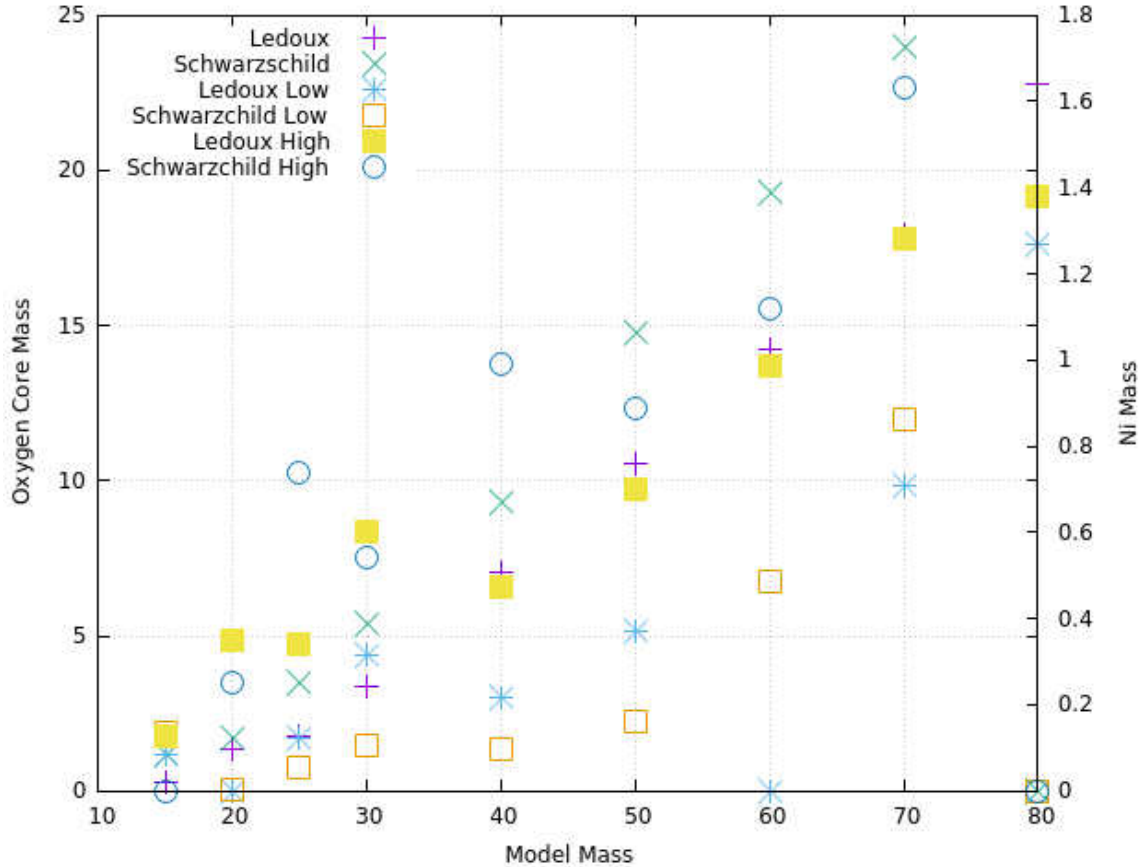
Figure 32. With only the degenerate iron core removed, plotting on the left side for the purple + and green × and the right side for the other four points. The Left plot shows the size of the oxygen rich core, starting at central point in star outward to end of oxygen rich region, to the M_{ZAMS}. The right side plots the produced Nickel mass for the high/low L/S series to the M_{ZAMS}

Figure 32 shows that as the M_{ZAMS} increases, the oxygen core increases. The

oxygen layer in the core is the second to last fuel to burn, requiring $1.5 - 2.6 \times 10^9$ K to

undergo nuclear fusion. The larger stellar masses provides conditions for the star to

maintain a high enough temperature and density to fuse up to oxygen and usually fuse to

silicon. Table 7 shows that in the pre-supernova star, the silicon core mass tends to be

larger in the Schwarzschild series. Given the rates shown in figure 34, the larger silicon

mass may explosively burn into a higher nickel mass. This is supported by the trends

shown in figure32 and discussed in Woosley et al. (1973).

Mass ($M_\odot$)	Convection	Oxygen Core Mass ($M_\odot$)	Silicon Core Mass ($M_\odot$)
15	L	0.278	0.209
	S	1.179	0.973
20	L	1.377	0.946
	S	1.707	0.379
25	L	1.785	0.484
	S	3.495	0.752
30	L	3.385	0.470
	S	5.365	0.420
40	L	7.048	0.671
	S	9.302	1.114
50	L	10.552	0.778
	S	14.783	1.383
60	L	14.244	1.382
	S	19.279	2.556
70	L	17.918	1.514
	S	23.958	3.152
80	L	22.769	2.644
	S	-	-

Table 7. Pre-core collapse Oxygen and Silicon core masses per star and convection criteria. Core masses are defined as measured from outward in, when the mass fraction of Si or O is greater then .5, the core mass is all mass contained within that region minus the remnant.

$$^{16}_{8}O + ^{16}_{8}O \rightarrow ^{28}_{14}Si + ^{4}_{2}He + 9.593 \text{ MeV (34\%)}$$
$$\rightarrow ^{31}_{15}P + ^{1}_{1}H + 7.676 \text{ MeV (56\%)}$$
$$\rightarrow ^{31}_{16}S + n + 1.459 \text{ MeV (5\%)}$$
$$\rightarrow ^{30}_{14}Si + 2 ^{1}_{1}H + 0.381 \text{ MeV}$$
$$\rightarrow ^{30}_{15}P + ^{2}_{1}D - 2.409 \text{ MeV (5\%)}$$
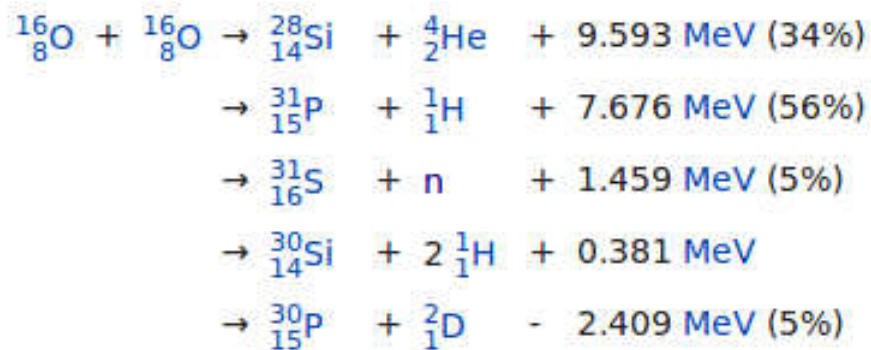
Figure 33. The fusion chains for the $^{16}_{8}O - ^{16}_{8}O$ reaction

$$^{28}_{14}Si + ^{4}_{2}He \rightarrow ^{32}_{16}S$$

$$^{32}_{16}S + ^{4}_{2}He \rightarrow ^{36}_{18}Ar$$

$$^{36}_{18}Ar + ^{4}_{2}He \rightarrow ^{40}_{20}Ca$$

$$^{40}_{20}Ca + ^{4}_{2}He \rightarrow ^{44}_{22}Ti$$

$$^{44}_{22}Ti + ^{4}_{2}He \rightarrow ^{48}_{24}Cr$$

$$^{48}_{24}Cr + ^{4}_{2}He \rightarrow ^{52}_{26}Fe$$

$$^{52}_{26}Fe + ^{4}_{2}He \rightarrow ^{56}_{28}Ni$$

$$^{56}_{28}Ni + ^{4}_{2}He \rightarrow ^{60}_{30}Zn$$
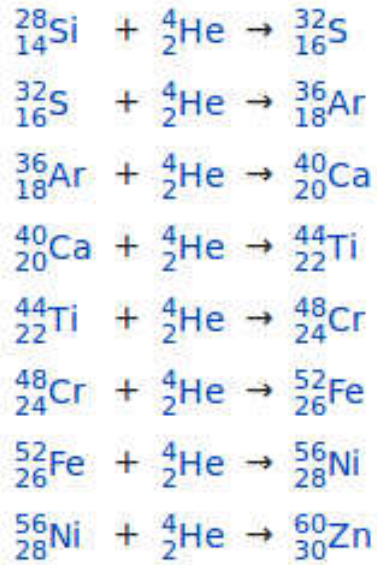
Figure 34. The fusion chains for the $^{28}_{14}Si$ burning

The nickel yields in figure 30 are higher than those published by Mller et al. (2017). This may be due to the Fe core central remnant, which could smaller in size than what is observed or used in other studies. The energy required to completely eject the outer layers in the Ledoux series shown in table 3 is relatively high compared to those found in Mller et al. (2017). The silicon core mass in table 7 ranges from .2 to 3.15 $M_\odot$ has the possibility of completely falling back into the central remnant given that the central remnant is chosen to be 5 $M_\odot$. In that case the formation of nickel would have to be created in the oxygen rich region and thus go through two burning process as shown in figures 33 and 34.

4.1.2 SN1987a

In section 3.1.1.1, the low energy Ledoux CCSNe has a similar light curve to SN1987a shown in figure 35. The distinctive features of this supernovae is the bright peak followed by a decline in the brightness of the SNe, before a re-brightening by almost 2 orders of magnitude due to the radioactive decay of nickel before falling to the standard Ni-decay powered late time lightcurve. Looking at figure 8, the same features appear, with the exception that our second peak is hydrodynamic in nature, but can be broadened or brightened with the addition of the $\gamma-$ ray energy deposition from the beta decay of Ni to Co to Fe, which can be seen in figure 9.

There exists a variety of progenitor models in the literature that reproduce the lightcuve of SN1987a shown in Table 8. Comparing these to our 15 and 20 $M_\odot$ in table 2, our models have similar radii. In solar radii, the radii of the SN1987a models are in the 50 $R_\odot$ range. This implies that the internal structure of our Ledoux models matches closer to that of the SN1987a models then the larger Schwarszschild models, but the comparison may not be reasonable due to the metallicity of $Z = 0$ in this work at formation compared to those in the SN1987a models, ranging from full solar to 'low' metallicity.

model	$M_\alpha/M_\odot$	$M_{He}/M_\odot$	$R/10^{12}cm$	Structure	$Z/Z_\odot$	Rotation
W18	7.39	9.53	3.3	Full	1/3	Yes
N20	6	10	3.3	core+env	low	No
S19.8	6.12	9.73	74	Full	1	No
W15	4.1	10	2.8	core+env	1/4	No
W20	5.86	13.5	4.5	Full	1/3	No

Table 8. A selection of SN1987a progenitor stars with a range of H/He masses, radii, and metallicity. Full structured models are those who evolve the whole star to a final stage, while the core+env models are those with an evolved core stitched to another stars evolved envelope. Reproduced from Sukhbold et al. (2016). The five models, in order, are from Sukhbold et al. (2016),Shigeyama & Nomoto (1990),Woosley et al. (2002),Woosley et al. (1988),and Woosley et al. (1997)
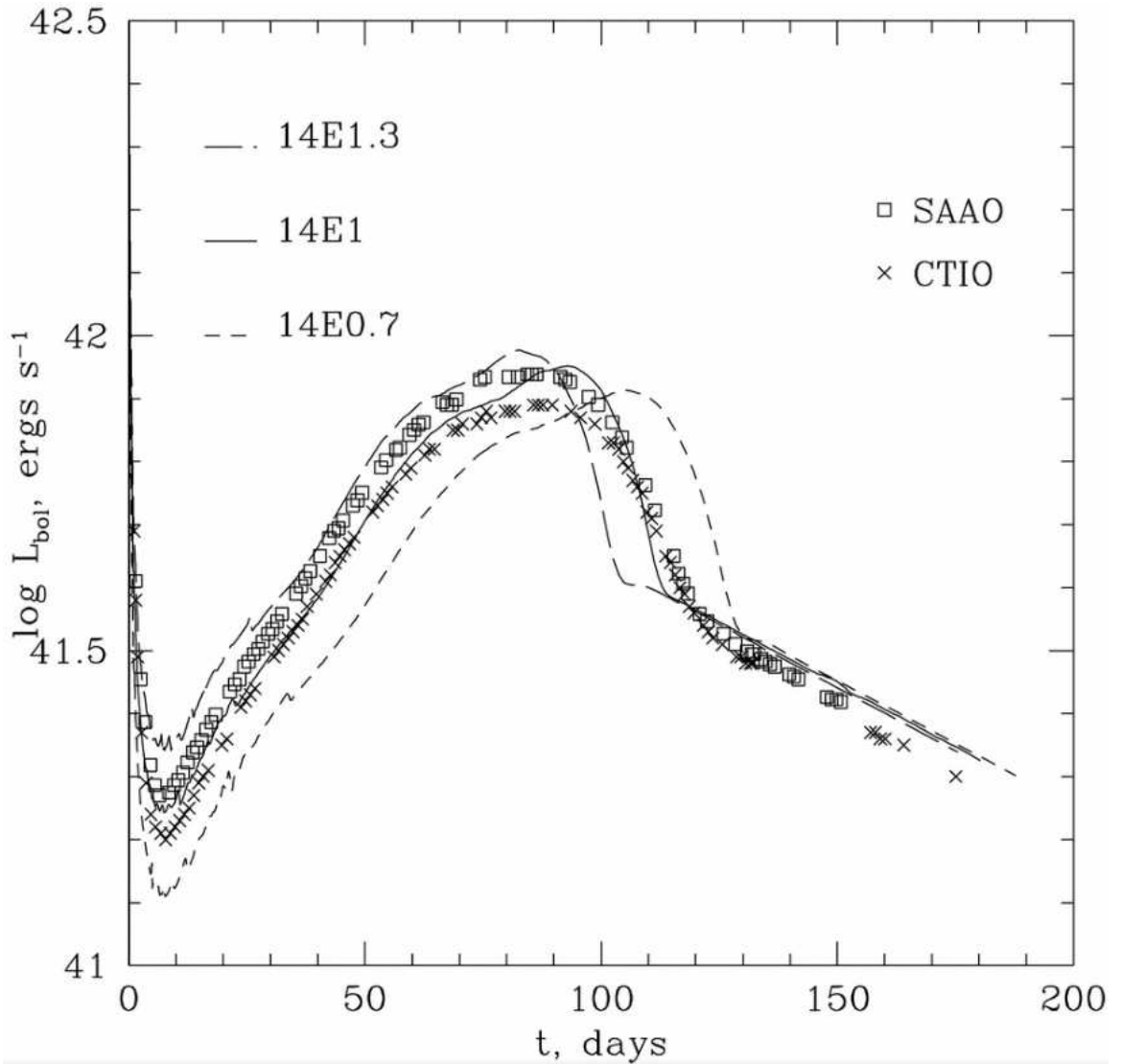
Figure 35. Taken from Blinnikov et al. (2000), graph shows the light curve of SN1987a for three explosion energies (1.3,1,.7) plotted over the observational data from CTIO and SAAO, (Catchpole et al., 1987) and (Phillips et al., 1988) respectively.

4.1.3 Compactness

O'Connor & Ott (2011) explored a compactness parameter $\zeta_{2.5}$ as a way to determine the explodability of pre-supernovae models. This parameter, defined in equation 4.1, is calculated at the time of core bounce, or when the infalling layers collides with the central remnant. My simulations do not use this infalling method, so this work sets t_{bounce} as zero.

Figure 36 shows plotted compactness parameters for the Ledoux and Schwarzschild model. Comparing our minimum energies and the compactness parameter to obtain a functional relation is difficult due to the coarseness in mass of our grid compared to the solar metallicity grids found in Sukhbold et al. (2016). Traditionally, the models that ζ predicts to be difficult to explode have been difficult to explode in the literature. The 'easily explodeability' description is defined as models that can explode at a wide range of energies, low and high.

$$\zeta_M = \left.\frac{M/M_\odot}{R(M)/1000km}\right|_{t_{bounce}} \tag{4.1}$$
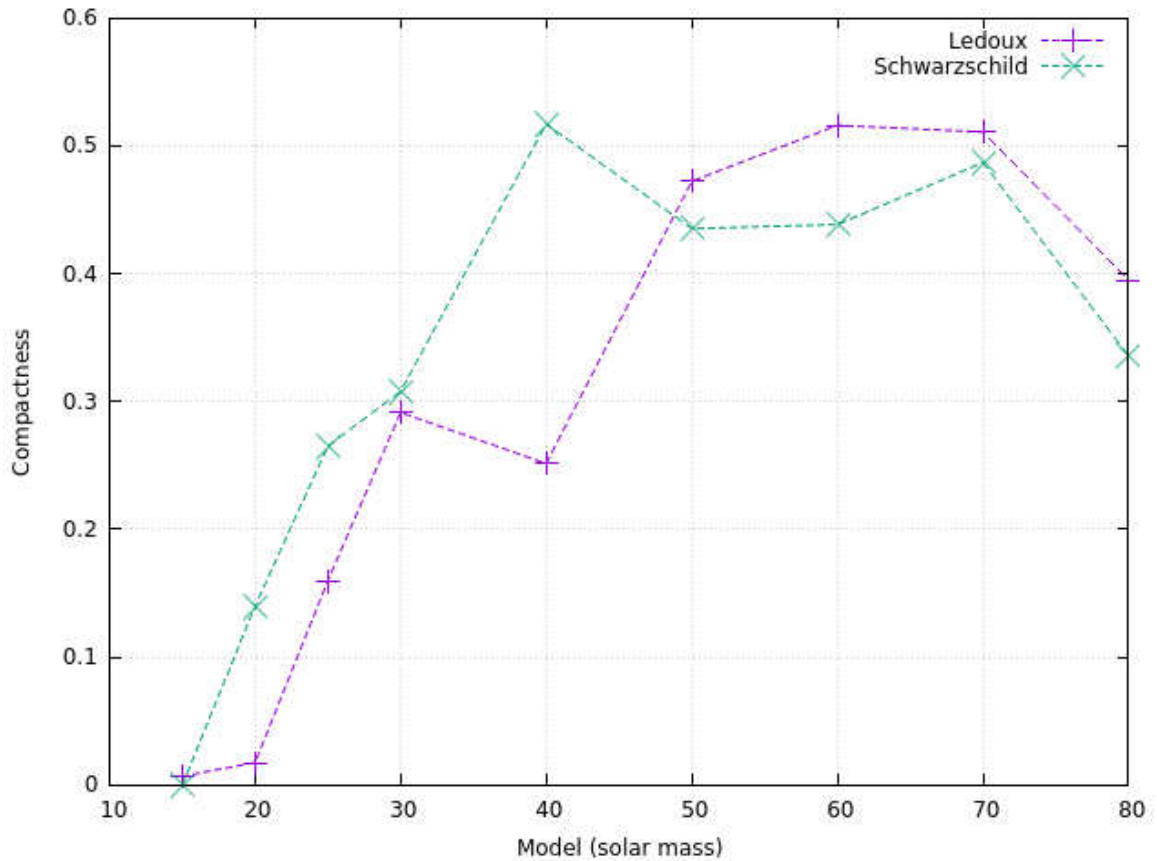
Figure 36. This is the compactness parameter $\zeta_{2.5}$ for the Ledoux and Schwarzschild series of models

As shown, the compactness parameter of the Ledoux models tend to increase towards the 50-70 $M_\odot$ range. This is not quite consistent with O'Connor & Ott (2011) and Sukhbold et al. (2016) which has a spike in the mid 20 $M_\odot$ and the 40 $M_\odot$. The Schwarzschild series has a larger spike at 40 $M_\odot$ which is more similar to that found in the previously cited works. There are several explanations for this variation. For one, the models used in O'Connor & Ott (2011) and Sukhbold et al. (2016), are generated in KEPLER (Woosley & Heger, 2007) are evolved at solar metallicities. In addition the KEPLER code includes a semi-convective overshooting and only the Ledoux criteria for convection so the final pre-core collapse star may have different density structure, influencing the progression of the shock wave. And finally, the t_{bounce} value as calculated in their codes may introduce a secondary effect not taken into account in the work presented here. Woosley & Heger (2007) has generated a finer grid of $Z = 0$ models and future work may include that grid and mine to try and determine a population III compactness parameter or another method of determining explodability.

4.2 Nucleosynthesis

4.2.1 First Zone

An interesting result comes from the first zone of each model over the whole range of models and both convection criteria. As discussed in section 2.3.2, to produce an explosion, the temperature of the first zone is increased artificially to initiate a shock. This energy injection is treated as an time independent, and thus only the subsequent expansion cools this region. Changing this temperature too high, and the innermost region burns through its material rapidly due to the temperature being in the range of $8 - 11 \times 10^9$ K while the material is still dense enough for nucleosynthesis to occur.

Figure 37 shows the temperature profiles of two zones; the first and tenth zones. The first zone, where the thermal bomb was placed, shows that the temperature stays high before the expansion and subsequent cooling. Zone 10 shows a lower initial steady temperature and then a spike in the temperature due to the shock impacting and compressing this region and therefore increasing the temperature to 4×10^9 K.
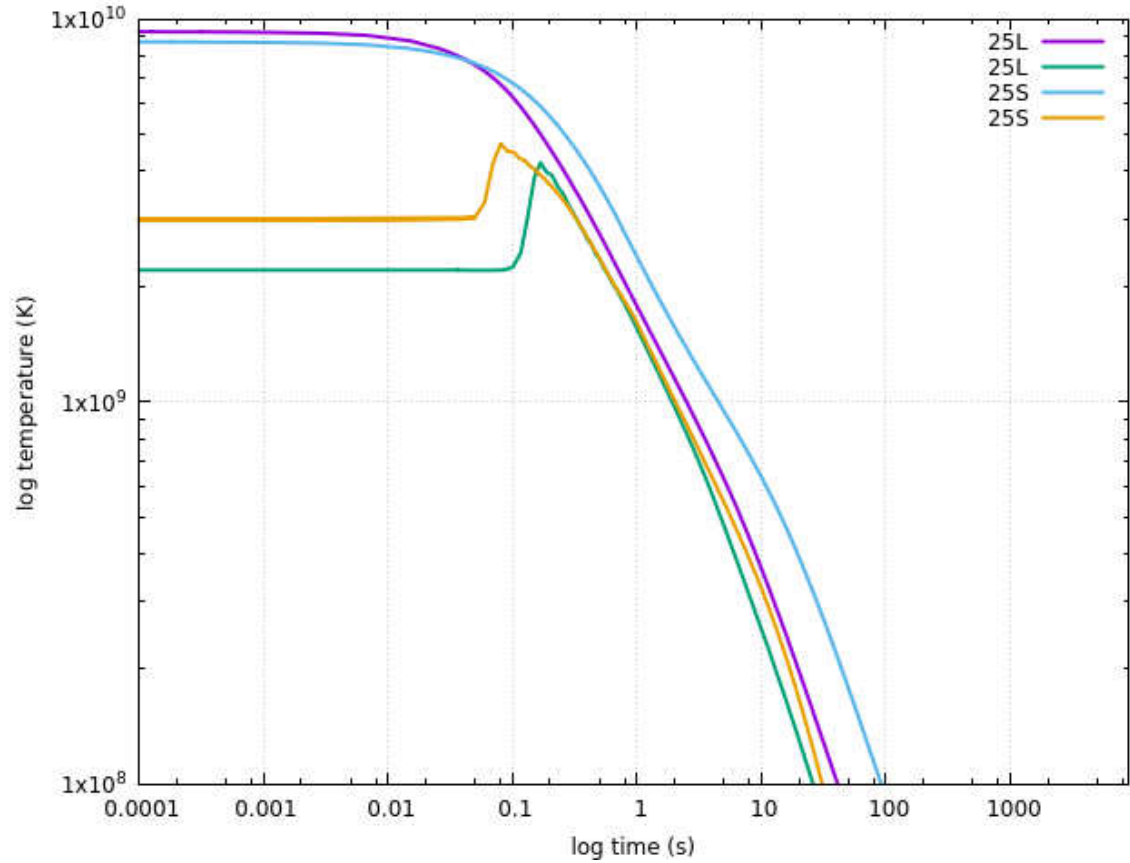

Figure 37. This is first and tenth zone of both of the 25 $M_\odot$ stars exploded at the minimum energy as shown in 3

In figures 38 and 39 the pre- and post-supernovae abundances of the first zone for all models and energies are shown.

In most of the Ledoux models, the composition of the innermost zone is iron and silicon. Note that in figure 37 the temperature and density, not shown, are both high. This
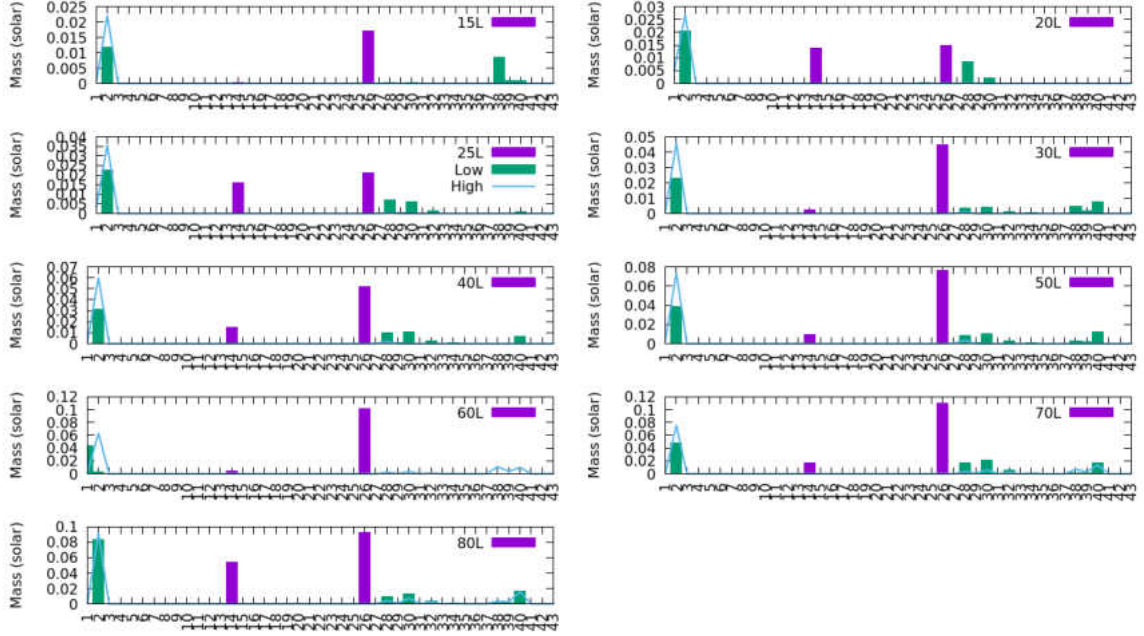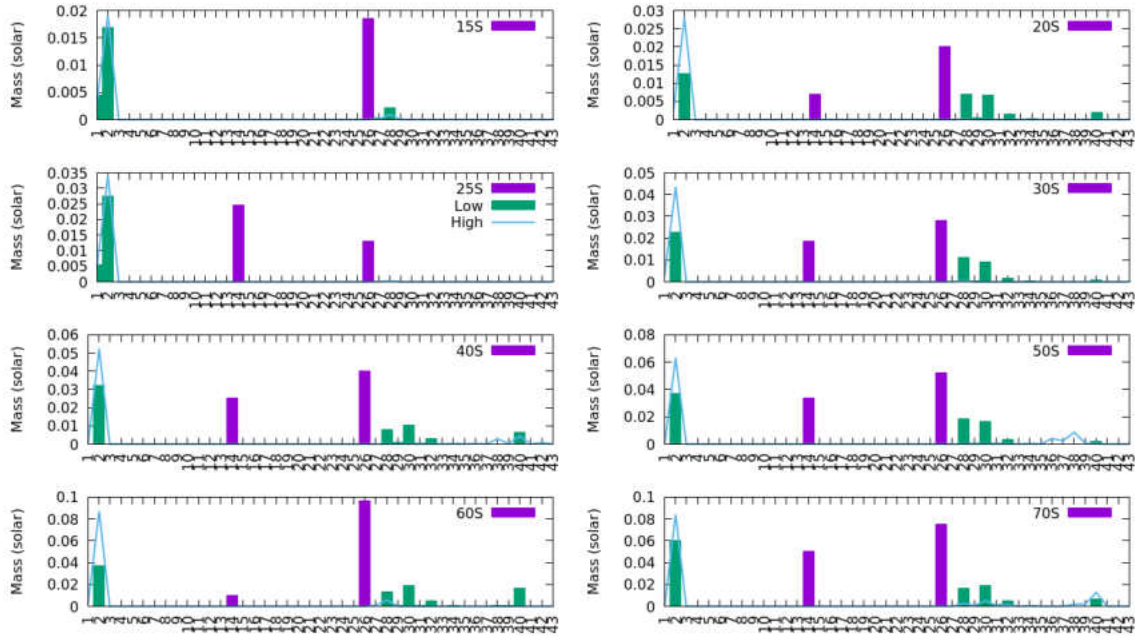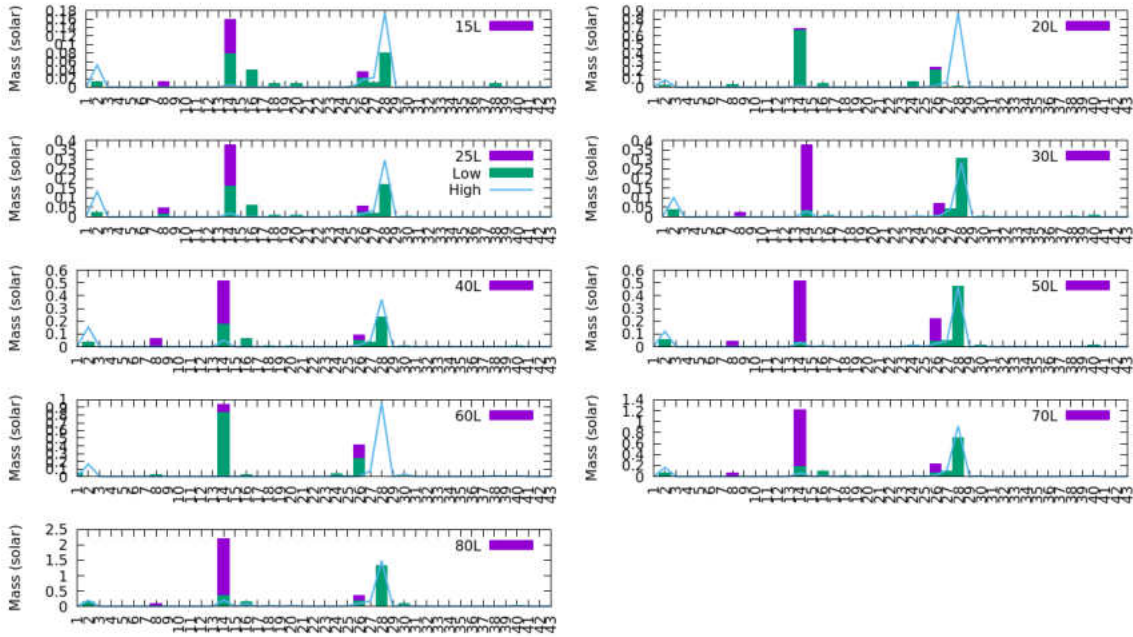
Figure 38. This is all nine Ledoux models exploded at the minimum and high explosion energy series shown in 3 and 4. In all plots, the colors are represented by that in the 25L plot, such that the purple bar is the pre-supernovae, green is the low explosion energy and the teal line is the high explosion energy yields.

results in the process of photodisintegration (Carroll & Ostlie, 2007) seen in equations 4.2 and 4.3. This causes the iron rich edge of the core to produce a high quantity of helium, called α particles. This material may separate again into protons and neutrons. If the iron is not completely disintegrated, the remaining iron can interact with the helium, protons, or neutrons to form heavier elements, such as nickel, as the material cools to lower temperatures.

$$\gamma +^{56} Fe \longrightarrow 13^4 He + 4n \tag{4.2}$$

$$\gamma +^4 He \longrightarrow 2p^+ + 2n \tag{4.3}$$

The material may not completely burn into helium or recombine as the material cools to form heavier elements, which can be seen in several of the models. The models with the

higher energy shock, represented by the light blue line, produces primarily helium in the models with masses less than 60 $M_\odot$ models. Some nickel is produced in this zone for some of the higher mass models. This leads to the conclusion that the main source of nickel production is outside this zone in order to account for the mass of nickel produced.

Figure 39. This is all nine Ledoux models exploded at the minimum and high explosion energy series shown in 3 and 4. In all plots, the colors are represented by that in the 25S plot, such that the purple bar is the pre-supernovae, green is the low explosion energy and the teal line is the high explosion energy yields.

In most of the Schwarzschild models, the trends seen in the Ledoux concerning the overall yields, are the same here for the first zone. The high explosion energy series produce a higher quantity of helium than that of the lower explosion energy series. This is likely due to the higher temperature rapidly disintegrating the iron into helium, especially in the lower mass models. Similar to Ledoux, the higher Schwarzschild mass models do produce some heavier elements, but minimal amounts of nickel.

4.2.2   Silicon Core

Table 7 shows that the mass of the silicon core does not scale at the same rate of the oxygen core or that of the total mass of the star. Figures 40 and 41 show the yields in the silicon core. For the silicon core, the abundances in the first zone are also included.
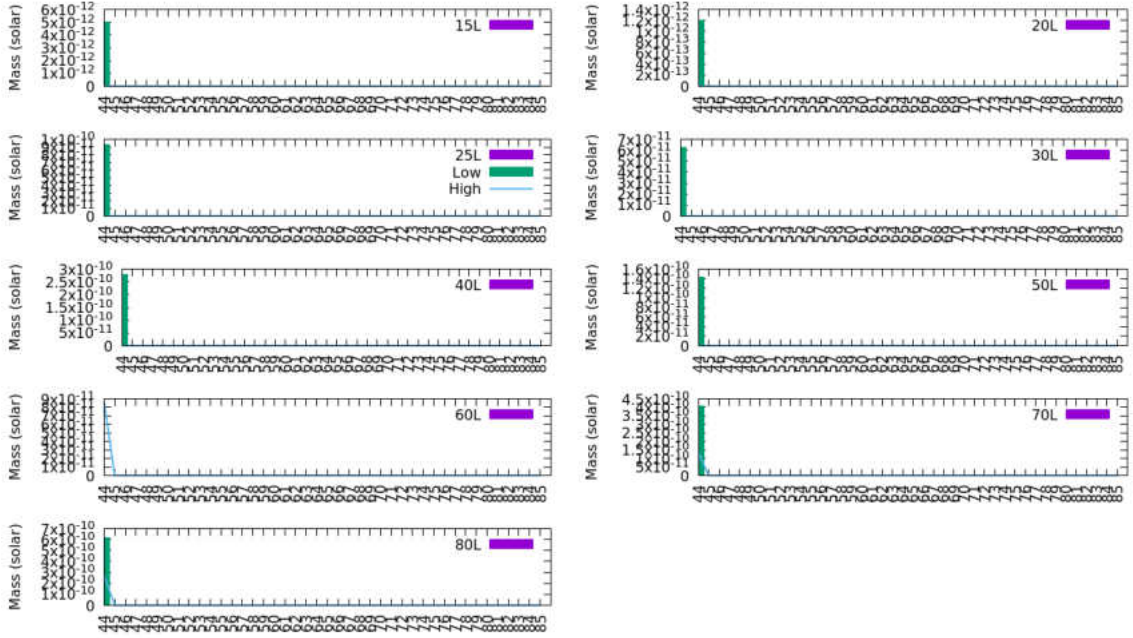

Figure 40. This is all nine Ledoux models exploded at the minimum and high explosion energy series shown in 3 and 4 for the silicon core. In all plots, the colors are represented by that in the 25L plot, such that the purple bar is the pre-supernovae, green is the low explosion energy and the teal line is the high explosion energy yields.

Figures 40 and 41 show that the silicon core is the primary source of the production of nickel for the both the high and low explosion energy series, excluding the 20 and 60 $M_\odot$ low explosion energy yields that show low to no nickel production. Examining the silicon and nickel values, it can be seen that as the silicon abundance decreases, the nickel yields increase. The low explosion energy series does not completely fuse the silicon core. The high energy does consume the entire silicon core, so following figure 34, the nickel production should increase. Looking at section 3.2 and comparing the

73

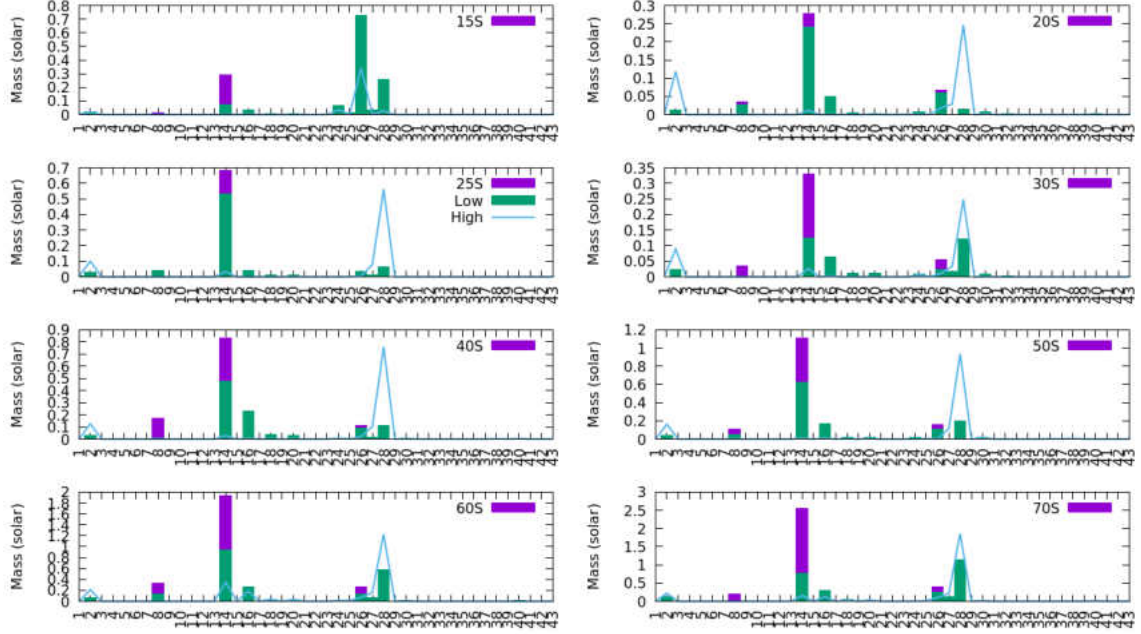Figure 41. This is all nine Ledoux models exploded at the minimum and high explosion energy series shown in 3 and 4 for the silicon core. In all plots, the colors are represented by that in the 25L plot, such that the purple bar is the pre-supernovae, green is the low explosion energy and the teal line is the high explosion energy yields.

high and low explosion energy abundances for individual stars, the abundances for other elements in the Si burning chain, such as S, Ca, and Ti, show increased yields. The high abundance of helium in this region is due to the inclusion of the first zone being included in the definition of the Si core.

Elements above $Z = 43$ show low yields in the $10^{-12} - 10^{-10} M_\odot$ range.

Figures 42 and 43 show again that the silicon core is the primary source of production of nickel for both the high and low explosion energy series. The silicon core shows a higher abundance of iron compared to the ledoux series, especially in the case of the 15 $M_\odot$ model. The initial abundance of iron is hidden by the green bar of the low energy yields. The 20 $M_\odot$ Ledoux and Schwarzschild with low explosion energy show low nickel yields and only a partially burned silicon core. In the high energy case, the silicon
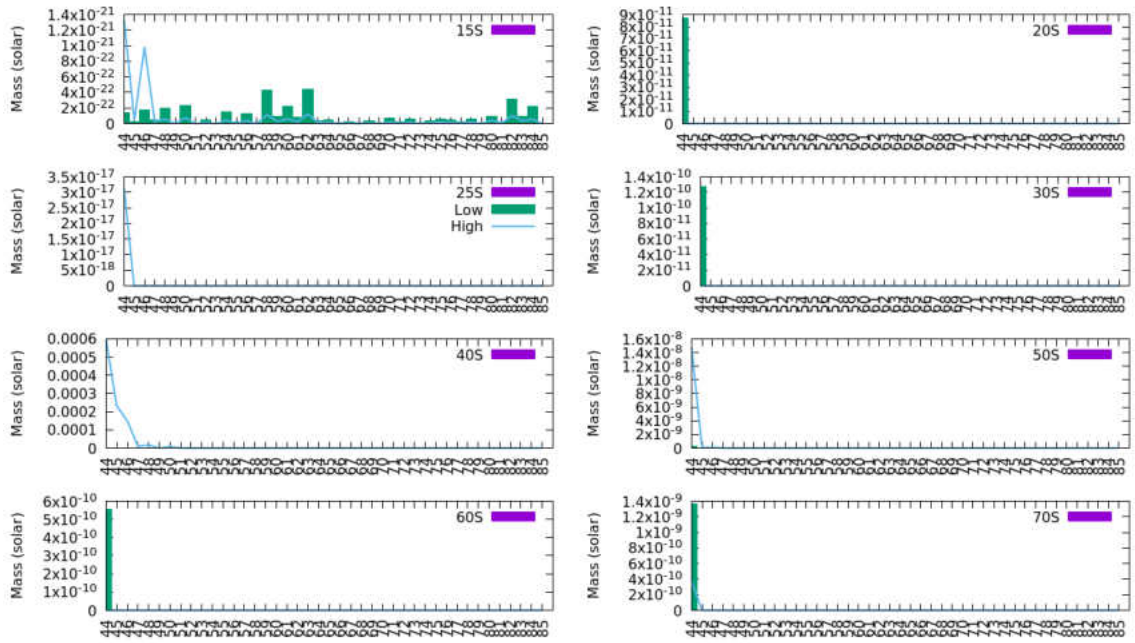
Figure 42. This is all eight Schwarzschild models exploded at the minimum and high explosion energy series shown in 3 and 4 for the silicon core. In all plots, the colors are represented by that in the 25S plot, such that the purple bar is the pre-supernovae, green is the low explosion energy and the teal line is the high explosion energy yields.

core is almost completely fused into nickel with a helium mass of approximately 0.1 $M_\odot$.

Elements above $Z = 43$ show low yields for the Ledoux models compared to those of the Schwarzschild yields.

4.2.3 Oxygen Core

Unlike the silicon core, the oxygen core grows in mass comparatively with that of the M_{ZAMS} of the model. For the larger mass stars, the mass and radius of the oxygen core would suggest that the entire oxygen core does not undergo explosive nucleosynthesis in the high or low explosion energy series due to the lower density and temperature further out from the core. The burning of oxygen requires 1.5 to 2.6 $\times 10^9$K and density ranges of 2.6 to 6.7 $\times 10^9$g/cm^3. Figure 44 shows that the mass closer to the silicon core maintains

Figure 43. This is all eight Schwarzschild exploded at the minimum and high explosion energy series shown in 3 and 4. In all plots, the colors are represented by that in the 25S plot, such that the purple bar is the pre-supernovae, green is the low explosion energy and the teal line is the high explosion energy yields.

temperatures required to burn the oxygen, but as the shock travels further out, it does not increase the local temperature high enough to explosively burn the oxygen.

Figures 45 and 46 show a key feature of the high energy explosion series is that the production of nickel extends into the oxygen core. The silicon core is defined when the mass fraction of silicon comprises 50 % of the zone, so there exists less than 50 % of silicon mass fraction in the first several oxygen core layers, allowing a high energy shock to burn silicon in the 2.7 to 3.5 $\times 10^9$K range. The higher mass models form a higher mass oxygen core during stellar evolution, leading to a higher percentage of the oxygen not burning, for either the high or the low explosion energy series.

In figures 46 and 48, there is spike in the $Z = 81$ to 84 range which corresponds to thallium, lead, bismuth, and polonium. Lead and bismuth are the two heaviest s-process
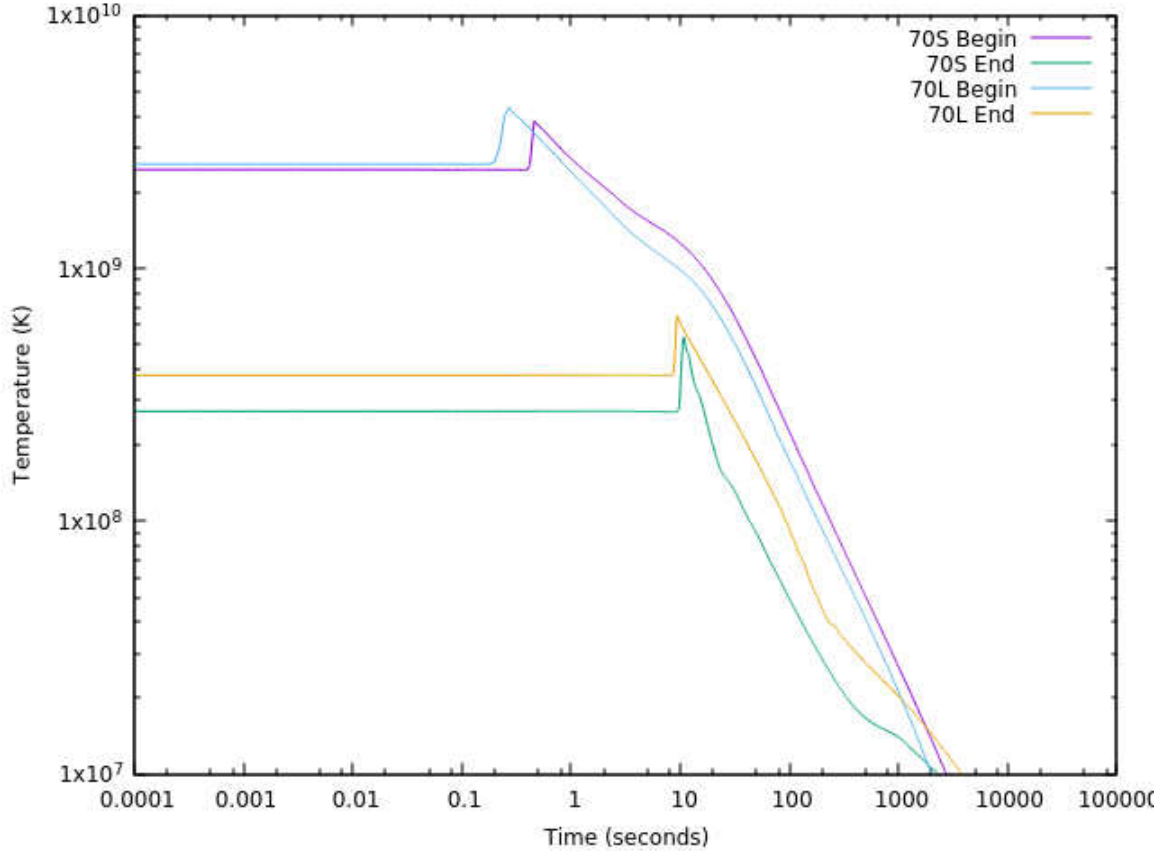
Figure 44. The temperature evolution of the 70 Ledoux and Schwarzschild models at the low energy explosion. Begin defines the first zone of the oxygen core while the end is the last zone of the oxygen core

products in nucleosynthesis (Roederer et al., 2009) but are also common end points for heavy radioactive elements. This range also is included in the decay chain of $Z = 85$, or Astatine. Astatine decays rapidly into radioactive isotopes of polonium, lead, bismuth, and thallium. While every isotope of polonium is unstable, there exists several isotopes with half-lives in the hundreds of years.

4.2.4   Remnant Masses

4.2.4.1   Nickel Mass Cut

Assuming that 0.07 $M_\odot$ of nickel is ejected, section 4.2.2 shows that this cut would only extend into the silicon core, ejecting the entire oxygen core. In table 7, the size of the Si

77
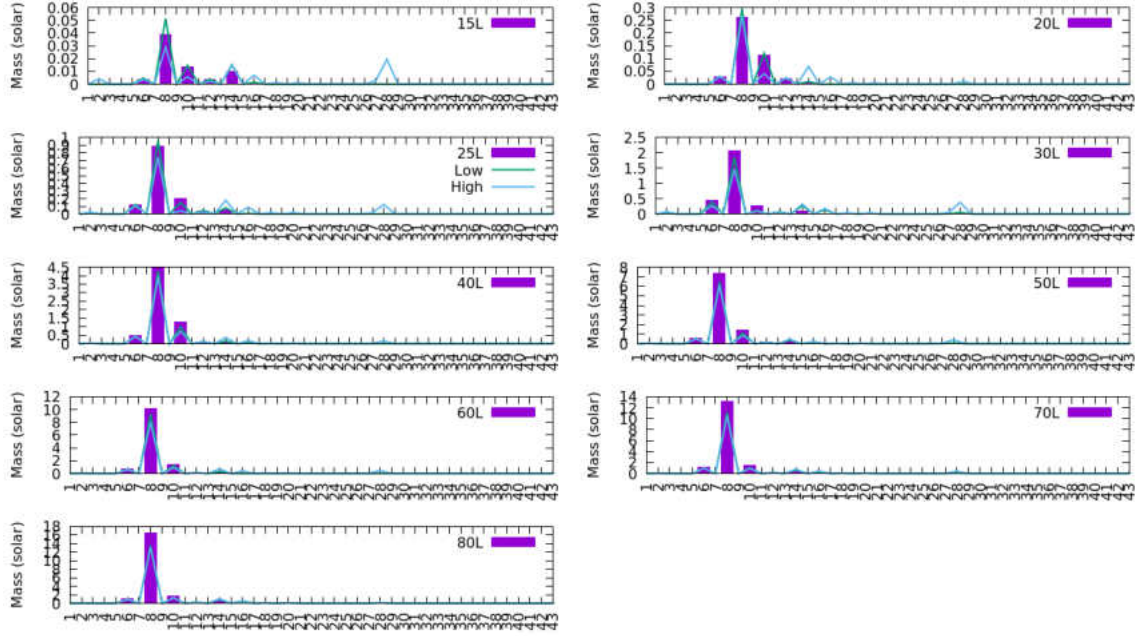
Figure 45. This is all nine Ledoux models exploded at the minimum and high explosion energy series shown in 3 and 4 for the oxygen core. In all plots, the colors are represented by that in the 25S plot, such that the purple bar is the pre-supernovae, green line is the low explosion energy and the teal line is the high explosion energy yields.

core ranged from 0.2 to 3.15 $M_\odot$ and in table 1, the central iron core ranged from 0.66 to 2.08 $M_\odot$. The Si core does not always fuse completely to nickel, especially in the case of the low energy explosions. In the high explosion energy series, the silicon in the oxygen layer also burns into nickel and the oxygen fusion that results into silicon, can supply an extra source of silicon for nickel fusion.

Figure 49 shows the nickel distribution for the 40 $M_\odot$ Schwarzschild model at high and low explosion energies. In general, the low explosion energy models produce less Ni and it is contained in a smaller region in the Si core. Whereas the higher explosion energy models produce more Ni and the Ni production often extends into the oxygen core. Assuming only that .07 $M_\odot$ of nickel is ejected, this means that on average, the yields of the silicon core are mostly ejected for the lower explosion energy series. The nickel cut
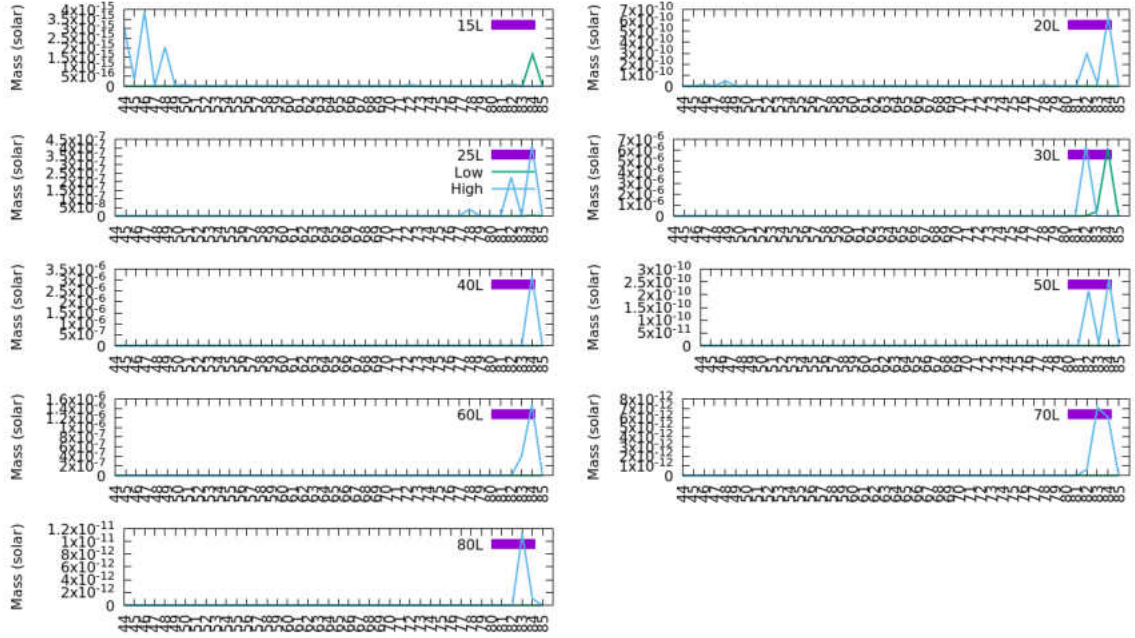
Figure 46. This is all nine Ledoux models exploded at the minimum and high explosion energy series shown in 3 and 4 for the oxygen core. In all plots, the colors are represented by that in the 25S plot, such that the purple bar is the pre-supernovae, green line is the low explosion energy and the teal line is the high explosion energy yields.

for the high energy explosion series extends into the inner layers of the oxygen core.

Removing the silicon core and the inner layers of the oxygen core would not eject Fe-peak

r-process elements but leaving the $Z > 50$ range unaffected.

4.2.4.2   Other Central Remnants

The assumption that only a 1.44 $M_\odot$ neutron star remnant is similar to that of the nickel

mass cut for the models with a degenerate iron core closer to 1.44 $M_\odot$ for the low

explosion energy series. The higher explosion energy series produces nickel further into

the oxygen core, but most 1.4 $M_\odot$ neutron star mass cuts remain in the silicon core.

In forming a large mass black hole, in the 5 $M_\odot$ range, would completely remove

the silicon core from all of the models and remove material further into the oxygen core
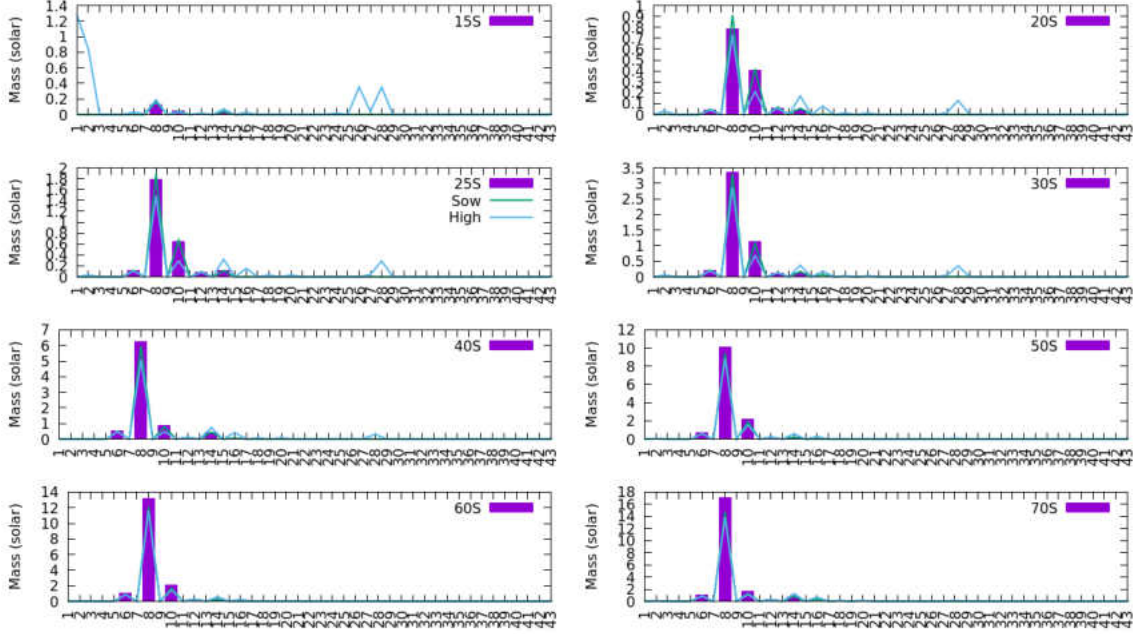
Figure 47. This is all eight Schwarzschild models exploded at the minimum and high explosion energy series shown in 3 and 4 for the oxygen core. In all plots, the colors are represented by that in the 25S plot, such that the purple bar is the pre-supernovae, green line is the low explosion energy and the teal line is the high explosion energy yields.

than the previous two cuts. This higher mass remnant would lower the abundances of high

Z elements drastically for the low energy explosion series but not for the higher explosion

energy series.

4.3   IMF

The initial mass fraction, or IMF, describes the distribution of the initial masses of stars

formed in a galaxy. Observationally, the IMF of the Milky Way tends to favor low mass

stars over high mass stars (Garmany, 1998). Low mass stars, specifically stars with M

$< 8M_\odot$, are not primary sources of enrichment of heavier elements. An analytic form that
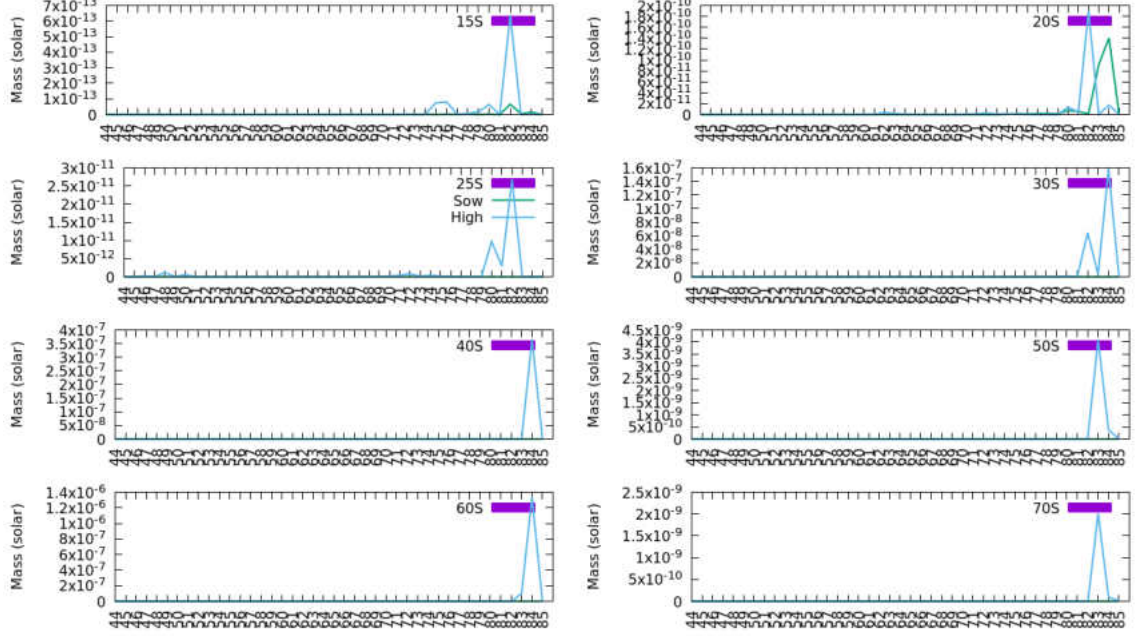
Figure 48. This is all eight Schwarzschild exploded at the minimum and high explosion energy series shown in 3 and 4. In all plots, the colors are represented by that in the 25S plot, such that the purple bar is the pre-supernovae, green line is the low explosion energy and the teal line is the high explosion energy yields.

matches well with observation is the Salpeter IMF (Salpeter, 1955) and is defined as

$$\xi(m)\Delta m = \xi_0 \left(\frac{m}{M_\odot}\right)^{-\alpha}\left(\frac{\Delta m}{M_\odot}\right) \qquad (4.4)$$

where α is a variable, usually defined as $\alpha = 2.35$ and ξ_0 is a constant related to local

stellar density or a scaling constant to achieve unity when integrated over the whole Δm

range. The Salpeter IMF is derived from the stellar populations in the Milky Way galaxy,

and may not represent the IMF of the early universe and population III stars, however it is

a good first approximation and is used here. Several groups, such as Bromm (2013)

,Cooke & Madau (2014), Greif et al. (2011), and Frebel & Norris (2015) have produced

several IMF's determined by the initial conditions used in cosmological

radiation-hydrodynamic simulations. These IMF's range from the bulk of stars being very
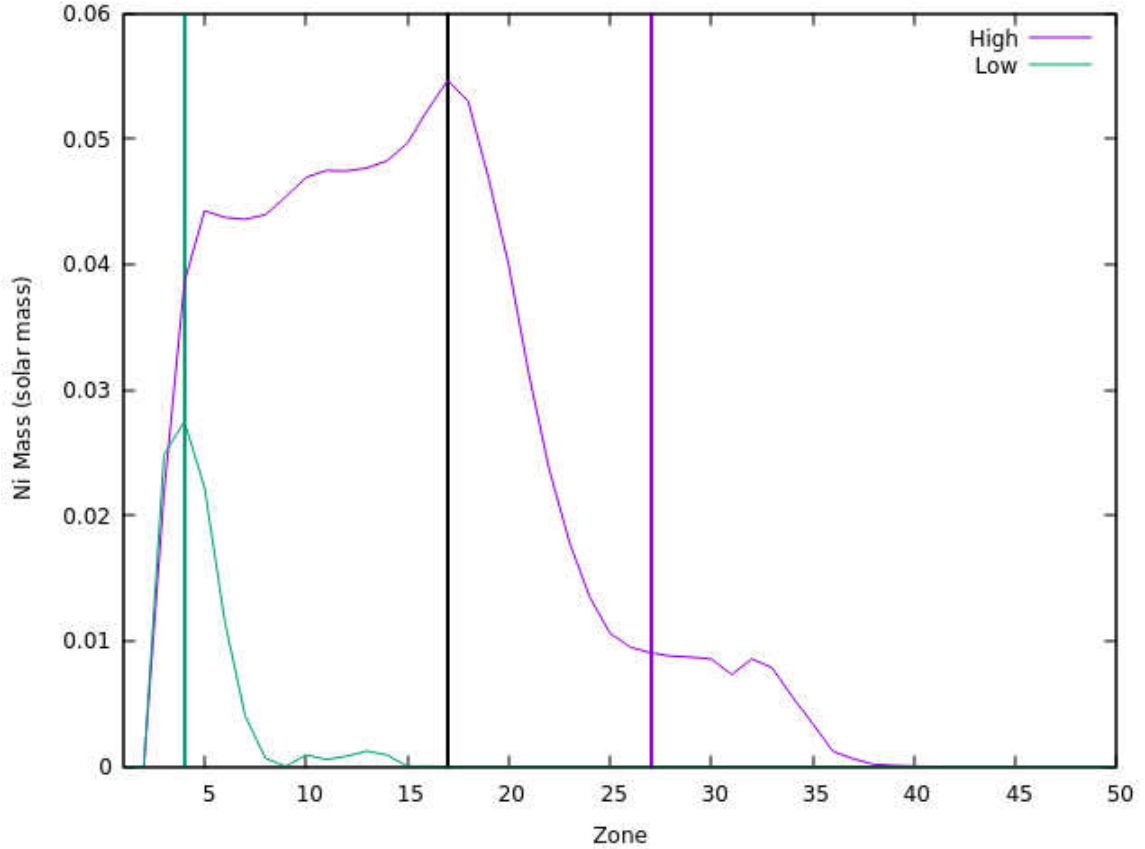
81

Figure 49. This is the 40 $M_\odot$ Schwarzschild high and low explosion energy series plotted with the Ni mass per zone. The vertical black line defines the edge of the Silicon core while the green and purple vertical lines represent the $M_{Ni} = .07M_\odot$ mass cut.

high mass, $M > 100M_\odot$ or a split between high mass and low mass. The models presented

here provide a unique distribution between the extremely low mass stars of masses M

$< 8M_\odot$ and the high mass stars.

To calculate the IMF, the Trapezoid Rule for numerical integration (Press et al.,

1993) for uneven intervals as shown in equation 4.5 is used. Several IMF's are integrated.

The first two will use a single convection criterion, either Ledoux or Schwarzschild, with

either high and low energy yields and the others will consider the remnant mass cuts. In

section 4.4, these IMF's will be compared to metal poor halo stars found in observational

databases.

$$\int_a^b f(x)dx \approx \sum_{k=1}^{N} \frac{f(x_{k-1}) + f(x_k)}{2} \Delta k \tag{4.5}$$

Following Tominaga et al. (2007), the IMF integrated elemental mass fraction is defined

by equation 4.6

$$X(A) = \frac{\int_{15M_\odot}^{80M_\odot} X_M(A)M_{ej}(M)\phi(M)dM}{\int_{15M_\odot}^{80M_\odot} M\phi(M)dM} \tag{4.6}$$

where X is defined as the mass fraction of element A, M_{ej} is the ejected mass, or

$M - M_{core}$, and ϕ is a simplified Salpeter IMF, where K is the normalization constant and

α is the same constant in the Salpeter IMF, in this case $\alpha = 1.35$ but the net exponent still

gives 2.35.

$$\phi(M) = KM^{-(1+\alpha)} \tag{4.7}$$

Equation 4.6 is integrated using equation 4.5 and results are shown in the following

sections.

4.3.1 Single Criteria IMF Yields

4.3.1.1 Ledoux IMF

Figures 50 and 51 show the integrated IMF's for the high and low energy explosions using

only the Ledoux convection criteria. The general yields of IMF's are similar with a few

noticeable changes discussed below. The higher energy IMF shows a peak in the Eu-Dy

range. These are well studied elements with regards to the r-process (Ishimaru & Wanajo,

1999). The Sr-Zr range are representative of light n-capture elements in which the exact

mechanism for their observed abundances are still not unknown (Burris et al., 2009).

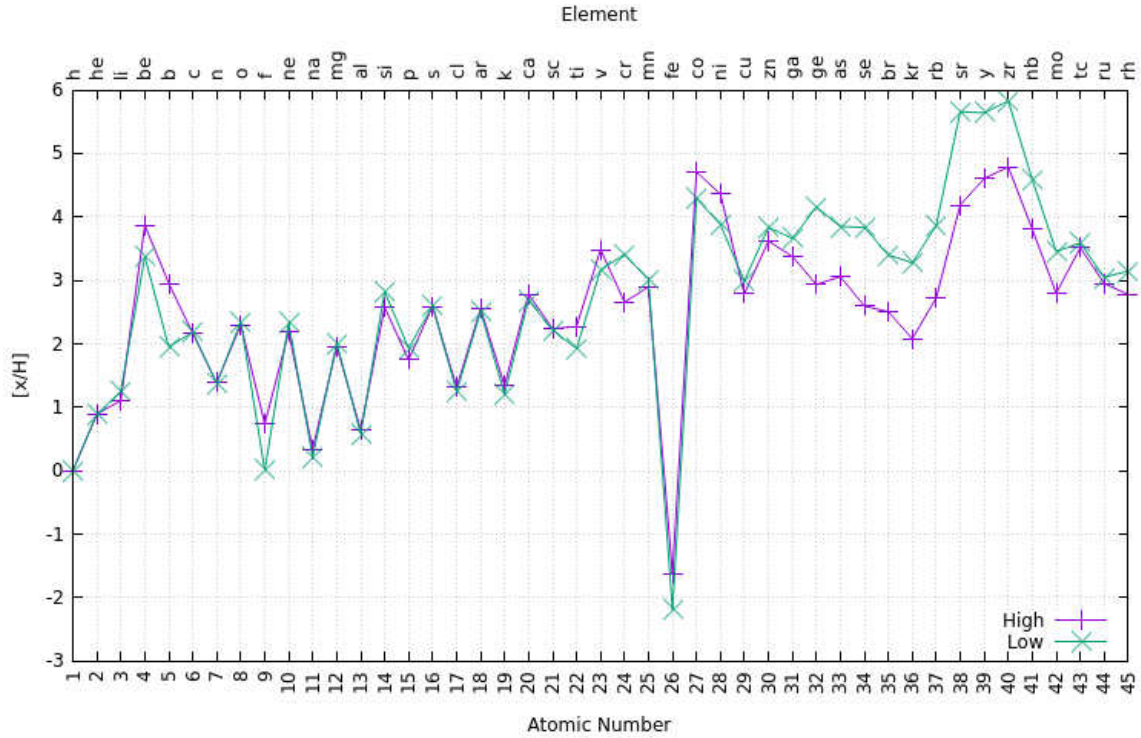Figures 52 and 53 show the integrated IMF's for three choices of remnant masses;

Figure 50. This is the full grid of Ledoux stars, in the 15 $M_\odot$ - $80 M_\odot$ mass range exploded at the high and low energy ranges for $1 \leq Z \leq 45$ plotted in terms of $[x/H]$.

the iron core, the neutron star, and the nickel mass cut. Figures 52 and 53 only include the

low explosion energy Ledoux model yields.

As the mass is increasingly removed from the inner layers, the range Si-Tc, or

$Z = 14 \text{to} Z = 43$, is generally reduced. Elements beyond $Z = 45$ remain unchanged. As

discussed previously in 4.2, using a neutron star or nickel mass cut as the remnant keeps

the remnant mass cut location usually in the silicon core, especially for the lower

explosion energy models. This does not alter the heavy elements, as they likely formed in

the outer edges of the silicon core and interior parts of the oxygen core. Assuming a

higher mass cut would likely significantly change the IMF yields as the degenerate iron

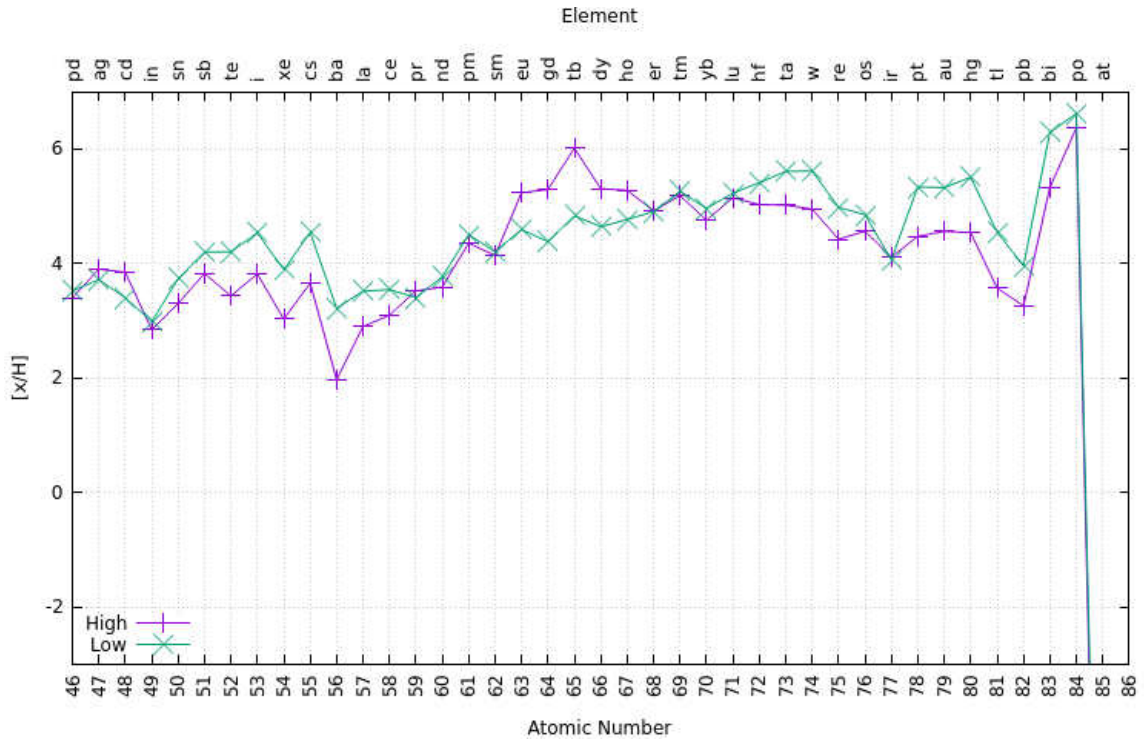core and the silicon core are close to 5 $M_\odot$ in total.

84

Figure 51. This is the full grid of Ledoux stars, in the 15 $M_\odot$ - $80M_\odot$ mass range exploded at the high and low energy ranges for $46 \leq Z \leq 86$ plotted in terms of $[x/H]$.

4.3.1.2 Schwarzschild IMF

Shown in 3.2, the general trends of the Schwarzschild models entailed a lack of high mass elements for the low energy models and only slightly higher abundances in the high energy models. In figures 54 and 55, the low energy abundances fall quickly after Zr, and stay below $[X/H] < -2$ until Bi. The high energy yields stay high with a significant dip at Ba and La but the abundances increase after maintaining an approximate $[X/H] \approx -2$.
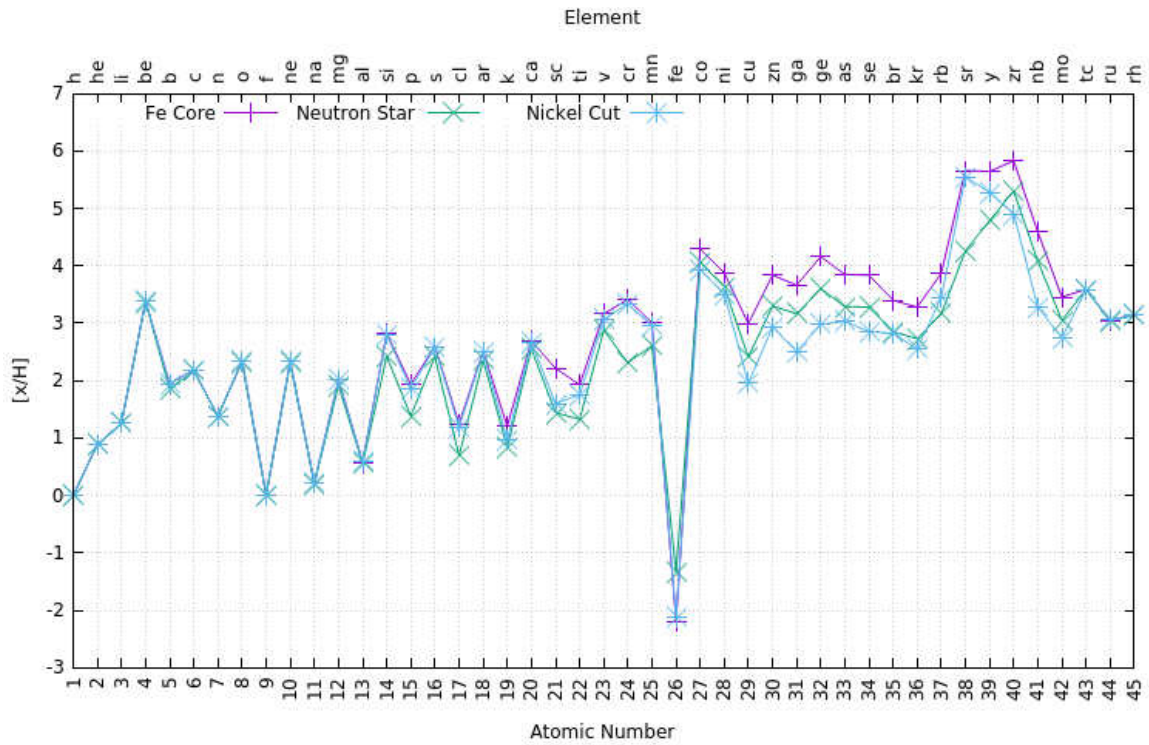
Figure 52. This is the full grid of Ledoux stars, in the 15 $M_\odot$ - $80M_\odot$ mass range exploded low energy ranges for $1 \leq Z \leq 45$ plotted in terms of $[x/H]$.

Similar to that of the Ledoux increasing the mass cut yields, only from Si to Ag is there alterations in the changes. Comparing the Fe to Neutron star core removal, the change in abundances is not significant above Cu, but shows the largest change near Cr. In a reverse correlation the Fe core stays high but the Ni and Neutron star cores correlate strongly. Beyond Ag, there is no change in the abundances.
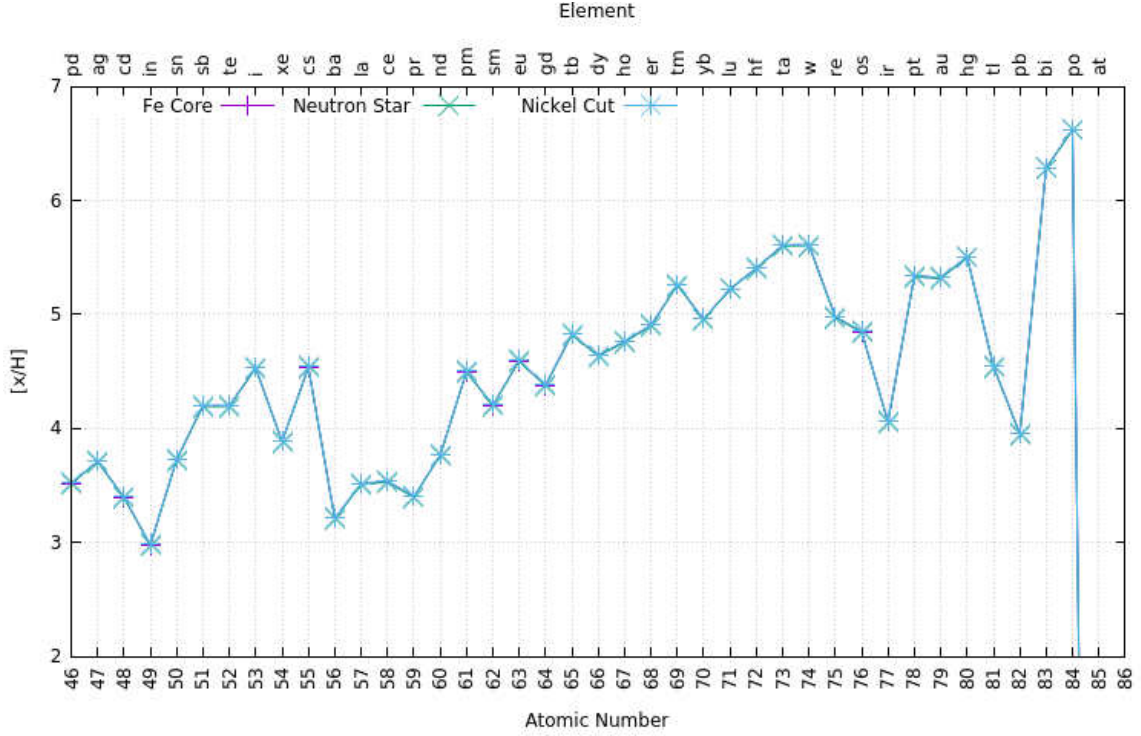
Figure 53. This is the full grid of Ledoux stars, in the 15 $M_\odot$ - $80M_\odot$ mass range exploded low energy ranges for $46 \leq Z \leq 86$ plotted in terms of $[x/H]$.

4.4 Observational Databases

The metallicity of a galaxy is enriched by the expelled gas from Type I and II SNe, likely from multiple sources (Mannucci & Cresci, 2012). Very old halo stars, or stars outside the plane of our Milky Way, were likely formed from possibly only one or two previous generations of stars if not a single star. As such, these stars are considered to be metal poor defined as $[Fe/H] \leq -3$ and are thought to be evolved stars in their giant phase.

Table 9 shows a set of 202 stars with calculated values for the abundances of 16 elements between $5 \leq A \leq 30$. These values are published by Ishigaki et al. (2018), but the abundances were calculated by the sources listed in table 9. These stars are all metal-poor halo stars, but not all stars have measurements for each element. These stars do not have measured abundances beyond the $A = 30$ range where the calculated abundances begin to

Figure 54. This is the full grid of Schwarzschild stars, in the 15 $M_\odot$ - $70M_\odot$ mass range exploded at the high and low energy ranges for $1 \leq Z \leq 45$ plotted in terms of $[x/H]$.

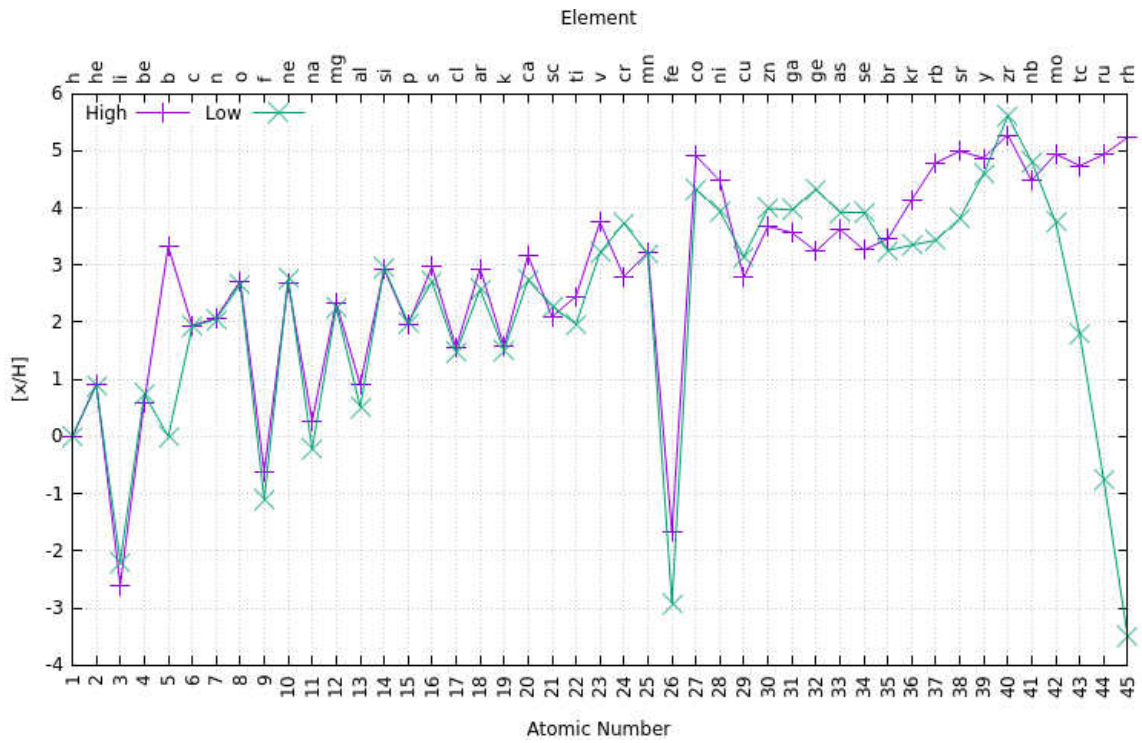show significant differences between the Ledoux and Schwarzschild convection criteria.
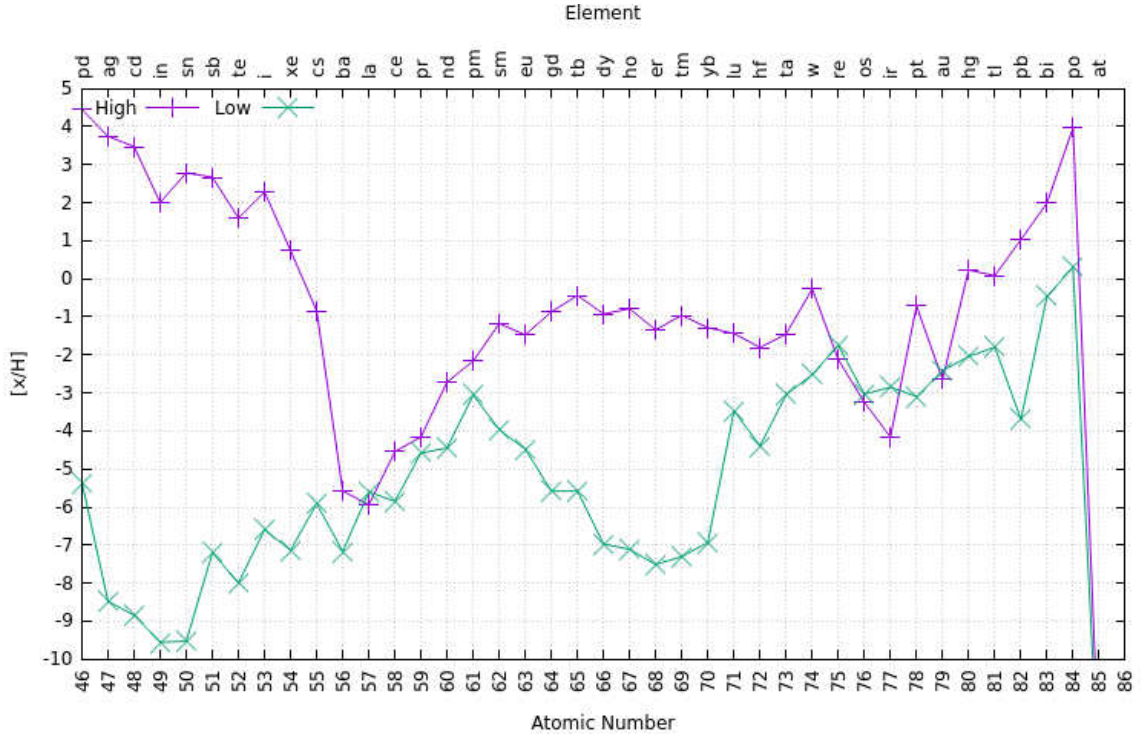
Figure 55. This is the full grid of Schwarzschild stars, in the 15 $M_\odot$ - $70M_\odot$ mass range exploded at the high and low energy ranges for $46 \leq Z \leq 86$ plotted in terms of $[x/H]$.

Figure 58, shows that the IMF's generated by this work appear does not fit beyond the Cr, or $A = 24$. The Fe, Co, and Ni abundance ranges are understood. The nucleosynthesis calculations are carried out to approximately 5 days to capture the peak Ni generation. The Ni decay chain, shown in equations 2.14 and 2.14, results into less abundant Ni and Co and more abundant Fe. This would result in the IMF ranges to shift further towards the observationally observed abundances by the reduction of Ni and Co and the increase in Fe. All of the IMF's in Figure 58 are shifted by a subtraction of 5 dex. A dex of 1 is equal to a reduction of 10^1 so a subtraction of 5 gives a reduction of 10^5 from the IMF's yields. This can be explained that the majority of the material mixes evenly throughout the star forming regions.

The yields of Si, Co, and Ni are all higher than the observational values shown
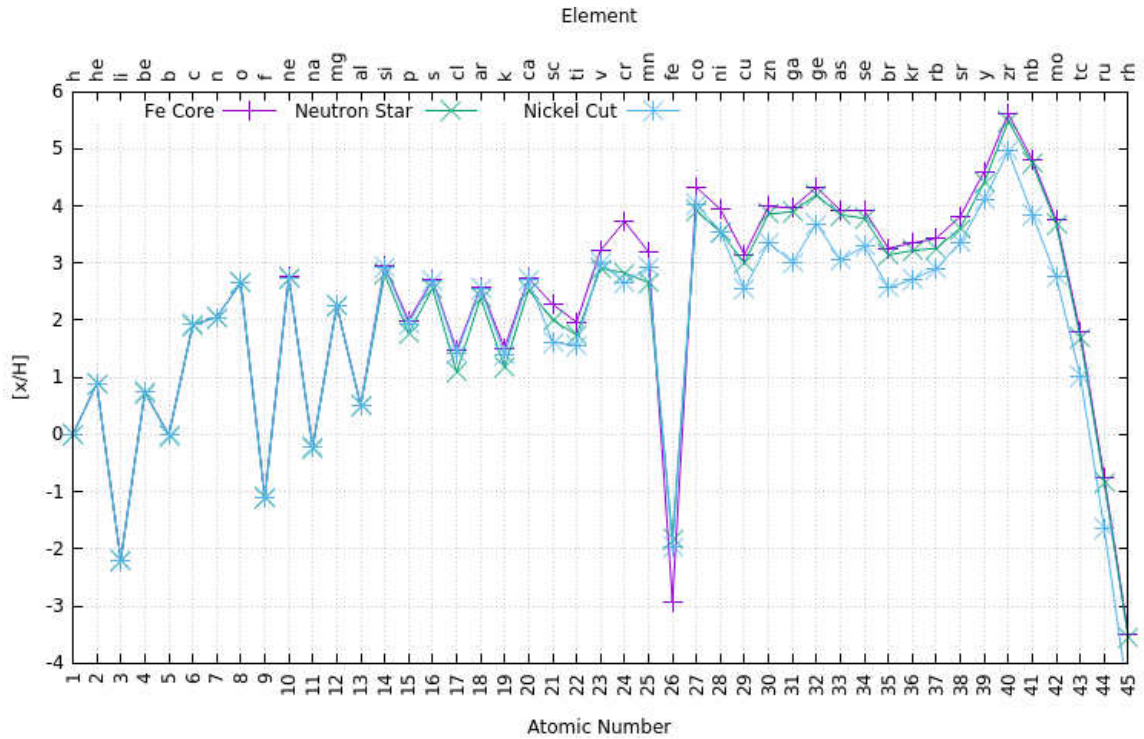
Figure 56. This is the full grid of Schwarzschild stars, in the 15 $M_\odot$ - $70 M_\odot$ mass range exploded at the high and low energy ranges for $1 \leq Z \leq 45$ plotted in terms of $[x/H]$.

where the lighter elements are a closer fit to that of the observed values. Section 4.2.2

showed that the Si core was the primary location for nucleosynthesis of Ni and Co in both

the low and high explosion energy models for both Ledoux and Schwarzschild models.

Section 4.2.4 discussed that the high explosion energy series fused nickel into the oxygen

core and requiring a 0.07 $M_\odot$ of nickel to be ejected can cut the silicon core from the

yields. Figure 59 shows the low explosion energy IMF's with the Ni and neutron star mass

cuts. Figures 60 and 61 show the individual high explosion energy star yields assuming
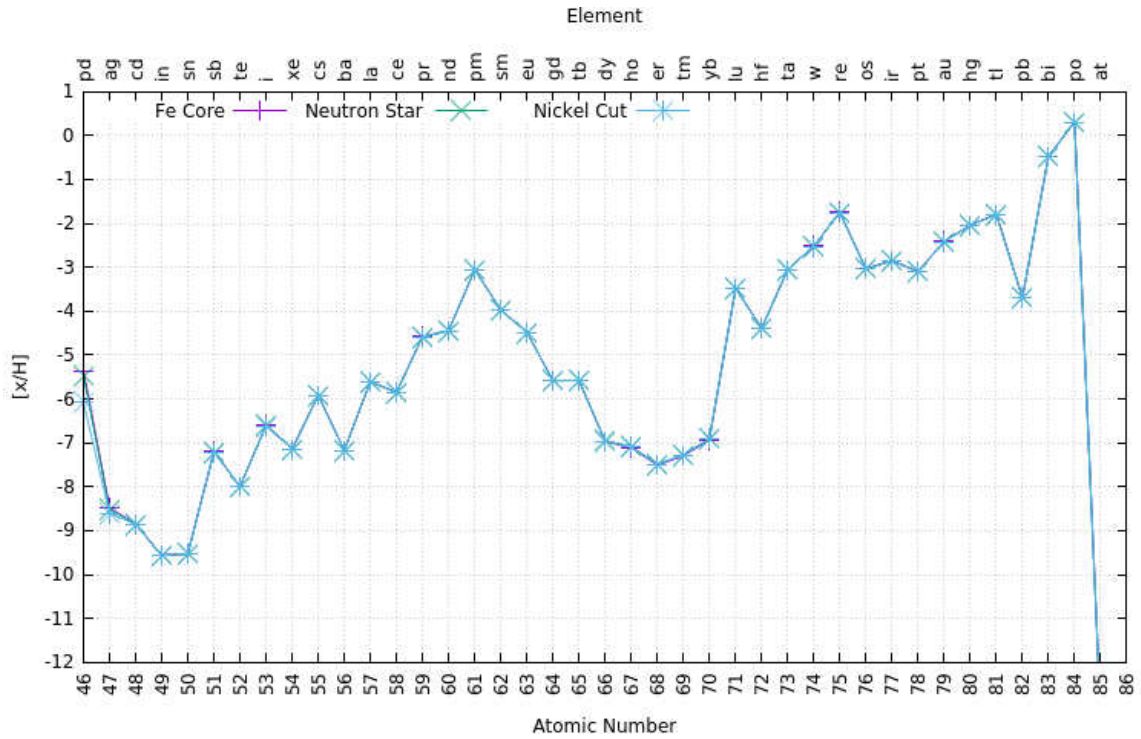
the Ni mass cut.

Figure 57. This is the full grid of Schwarzschild stars, in the 15 $M_\odot$ - $70M_\odot$ mass range exploded at the high and low energy ranges for $46 \leq Z \leq 86$ plotted in terms of $[x/H]$.

Looking at the individual stars, both Ledoux and Schwarzschild, the higher energy models with the Ni cuts fit much better than that of the lower energy IMF's. The Ni, Fe, and Co can still be explained by the discussion above. For the yields shown in figure 61, the Ledoux series does fit better, but still significant scatter and elements such as Mn are not in the range of any models. For the yields shown in figure 60, there is a lack of Zn in the models, but for the Ledoux and the Schwarzschild, it appears that only lower mass models have appreciable amounts of Zn ejected. The Schwarzschild series does have a better fit to N, only on the lower end so that Ca-Mn is closer to the observed values. There is less spread for the Schwarzschild series compared to that of the Ledoux.

Star	[Fe/H]	Reference	Star	[Fe/H]	Reference	Star	[Fe/H]	Reference
HE0020-1741	-4.05	9	CS22940-121	-3.14	3	HE1357-0123	-3.85	2
2MASSJ18082002-5104378	-4.07	8	CS22941-017	-3.11	3	HE1410-0004	-3.07	2
SDSSJ1313-0019	-5	7	CS22942-002	-3.61	3	HE1416-1032	-3.25	2
SDSSJ1322+0123	-3.64	6	CS22943-137	-3.64	3	HE1422-0818	-3.34	2
SDSSJ1204+1201	-4.34	6	CS22944-032	-3.22	3	HE1424-0241	-4.14	2
SMSSJ002148.06-471132.1	-3.17	4	CS22945-031	-3.29	3	HE1456+0230	-3.37	2
SMSSJ003327.36-491037.9	-3.36	4	CS22948-066	-3.5	3	HE1515-1055	-3.05	2
SMSSJ004037.56-515025.2	-3.83	4	CS22948-093	-3.32	3	HE2203-3723	-3.35	2
SMSSJ005953.98-594329.9	-3.93	4	CS22949-037	-4.38	3	HE2215-2548	-3.06	2
SMSSJ010332.63-534654.3	-3.03	4	CS22949-048	-3.55	3	HE2217-4053	-3.42	2
SMSSJ010651.91-524410.5	-3.79	4	CS22950-046	-4.12	3	HE2314-1554	-3.33	2
SMSSJ010839.58-285701.5	-3.02	4	CS22952-015	-3.87	3	HE2356-0410	-3.11	2
SMSSJ015941.53-781408.7	-3.11	4	CS22953-003	-3.13	3	HE2357-0701	-3.22	2
2MASSJ02031860-7930291	-3.03	4	CS22953-037	-3.21	3	BS16467-062	-3.51	2
SMSSJ022410.38-534659.9	-3.4	4	CS22955-174	-3.1	3	BS16545-089	-3.58	2
SMSSJ022423.27-573705.1	-3.97	4	CS22956-110	-3.15	3	BS16550-087	-3.44	2
SMSSJ023147.96-575341.7	-3.42	4	CS22957-013	-2.98	3	CS29527-015	-3.32	1
SMSSJ024643.28-352502.4	-3.37	4	CS22957-022	-3.28	3	HD4306	-3.04	1
SMSSJ024858.41-684306.4	-3.71	4	CS22958-083	-3.05	3	HE0049-3948	-3.68	1
SMSSJ031556.09-473442.1	-3.26	4	CS22960-010	-3.02	3	HE0102-1213	-3.28	1
SMSSJ032132.29-363123.6	-3.4	4	CS22960-048	-3.91	3	HE0130-2303	-3.02	1
SMSSJ033005.90-681352.5	-3.44	4	CS22960-053	-3.64	3	53327-2044-515	-4	1
SMSSJ040148.04-743537.3	-3.09	4	CS22963-004	-4.09	3	HE0146-1548	-3.46	1
SMSSJ051008.62-372019.8	-3.2	4	CS22968-014	-3.99	3	HE0218-2738	-3.57	1
SMSSJ063447.15-622355.0	-3.41	4	CS22968-029	-3.1	3	HE0231-6025	-3.1	1
SMSSJ065014.40-614328.0	-3.18	4	CS29498-043	-3.87	3	HE0242-0732	-3.3	1
SMSSJ085924.06-120104.9	-3.63	4	CS29502-092	-3.3	3	HE0253-1331	-3.01	1
SMSSJ093209.41-003435.8	-3.11	4	CS29506-090	-3.21	3	CS22172-002	-3.77	1
SMSSJ094029.05-060935.0	-3.18	4	CS30312-044	-3.22	3	CS22186-025	-3.07	1
2MASSJ10242264-2904203	-3.13	4	CS30312-059	-3.41	3	HE0557-4840	-4.81	1
SMSSJ123246.06-054559.1	-3.03	4	CS30314-067	-3.31	3	BS16469-075	-3.25	1
SMSSJ125804.65-335045.1	-3.44	4	CS30339-069	-3.5	3	HE1201-1512	-3.86	1
SMSSJ143511.34-420326.5	-3.15	4	CS30339-073	-3.93	3	BS16920-017	-3.4	1
SMSSJ173823.36-145701.0	-3.58	4	CS30492-016	-3.3	3	BS16085-050	-3.16	1
SMSSJ184226.25-272602.7	-3.89	4	CS30492-110	-3.27	3	BS16076-006	-3.51	1
SMSSJ184825.29-305929.7	-3.65	4	CS31082-001	-3.09	3	HE1300+0157	-3.75	1
SMSSJ190549.33-214945.0	-3.11	4	BD-206008	-3	3	BS16929-005	-3.34	1
SMSSJ190931.13-214053.9	-3.33	4	BD-185550	-3.2	3	HE1320-2952	-3.69	1
SMSSJ193528.46-462129.6	-3.39	4	BD+44493	-4.28	3	HE1402-0523	-3.17	1
SMSSJ200228.85-533114.4	-3.22	4	CD-38245	-4.59	3	BS16477-003	-3.39	1
SMSSJ200654.42-321157.7	-3.25	4	CD-30298	-3.77	3	CS30325-094	-3.35	1
SMSSJ202057.49-522417.2	-3.12	4	CD-241782	-3.05	3	HE1506-0113	-3.54	1
SMSSJ215805.81-651327.2	-3.41	4	G064-012	-3.58	3	BS16084-160	-3.2	1
SMSSJ225851.25-265434.9	-3.48	4	G190-015	-3.12	3	BS16080-093	-3.23	1
SMSSJ230013.16-263511.0	-3.35	4	G206-034	-3.17	3	CS30336-049	-4.1	1
CS22166-016	-3.22	3	HD88609	-3.29	3	HE2047-5612	-3.14	1
CS22169-035	-3.31	3	HD126587	-3.29	3	HE2135-1924	-3.31	1
CS22171-037	-3.63	3	HD200654	-3.13	3	HE2139-5432	-4.02	1
CS22174-020	-3.29	3	HD237846	-3.21	3	CS22965-054	-3.1	1
CS22177-009	-3.42	3	HE0454-4758	-3.38	3	CS29502-042	-3.27	1
CS22183-031	-3.57	3	HE1124-2335	-3.36	3	CS29516-024	-3.05	1
CS22185-007	-3.06	3	HE0134-1519	-3.98	5	CS29491-053	-3.03	1
CS22189-009	-3.92	3	HE1310-0536	-4.15	5	CD-2417504	-3.38	1
CS22873-128	-3.32	3	HE2239-5019	-4.15	5	CS22966-011	-3.02	1
CS22877-001	-3.31	3	HE0009-6039	-3.34	2			
CS22877-011	-3.23	3	HE0017-4346	-3.12	2			
CS22878-002	-2.97	3	HE0037-0348	-3.2	2			
CS22878-101	-3.53	3	HE0039-4154	-3.23	2			
CS22880-067	-3.23	3	HE0102-0633	-3.15	2			
CS22880-086	-3.28	3	HE0103-0357	-3.2	2			
CS22881-032	-3.55	3	HE0130-1749	-3.39	2			
CS22882-030	-3.47	3	HE0132-2429	-3.6	2			
CS22884-108	-3.1	3	HE0251-3216	-3.2	2			
CS22885-096	-4.41	3	HE0312-5200	-3.16	2			
CS22888-031	-3.71	3	HE0344-0243	-3.4	2			
CS22890-064	-3.12	3	HE0401-3835	-3.1	2			
CS22891-200	-4.06	3	HE0411-5725	-3.13	2			
CS22891-209	-3.49	3	HE0926-0546	-3.78	2			
CS22891-221	-3.23	3	HE1012-1540	-3.56	2			
CS22892-052	-3.24	3	HE1300+0157	-3.54	2			
CS22894-019	-2.98	3	HE1338-0052	-3.06	2			
CS22897-008	-3.83	3	HE1346-0427	-3.44	2			
CS22898-047	-3.51	3	HE1347-1025	-3.53	2			
CS22940-077	-3.1	3	HE1356-0622	-3.53	2			

Table 9. Plotted are the stars used, the metallicity of each star and the reference in which found the abundances are calculated. Citations are as follows 9:(Placco et al., 2016),8:(Meléndez et al., 2016),7:(Frebel et al., 2015),6:(Placco et al., 2015),5:(Hansen et al., 2014),4:(Jacobson et al., 2015),3:(Roederer et al., 2014),2:(Cohen et al., 2013),1:(Yong et al., 2013),
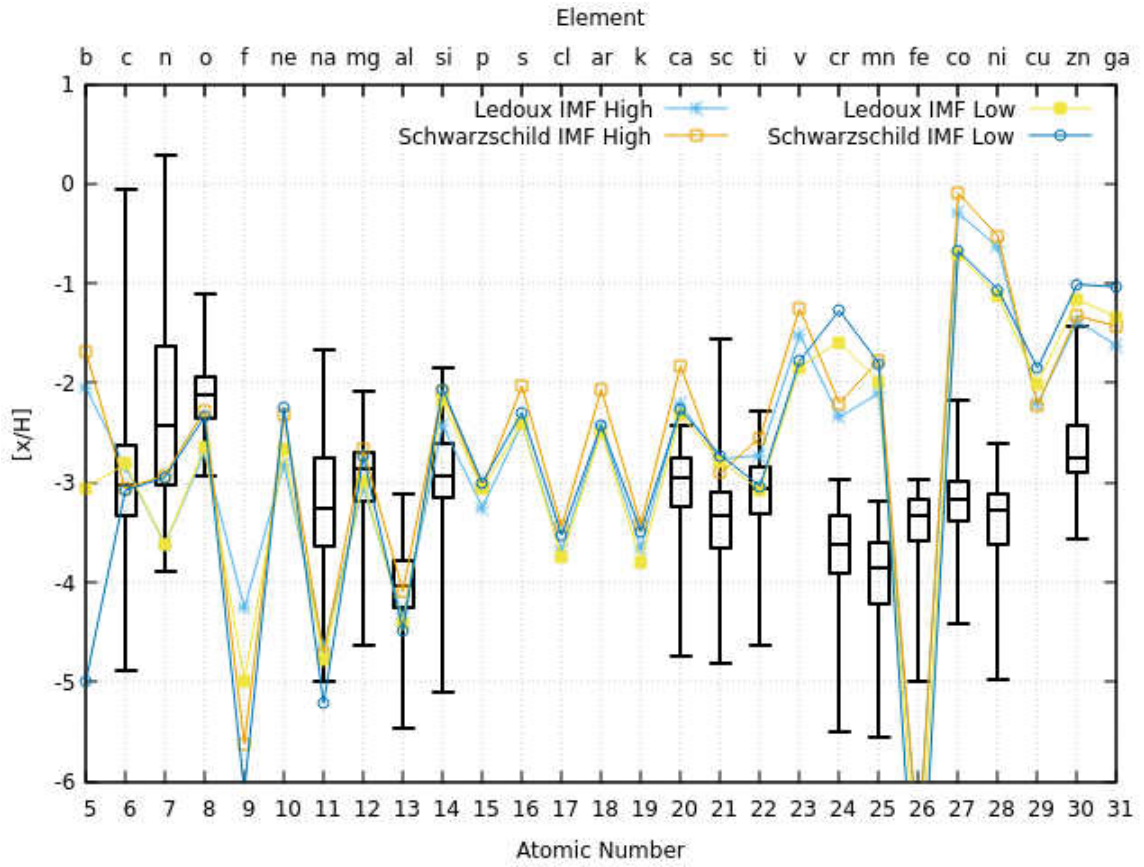
Figure 58. Plotted are the box and whisker plots for the stars as seen in table 9 with four IMF's plotted above with an approximate fitting.
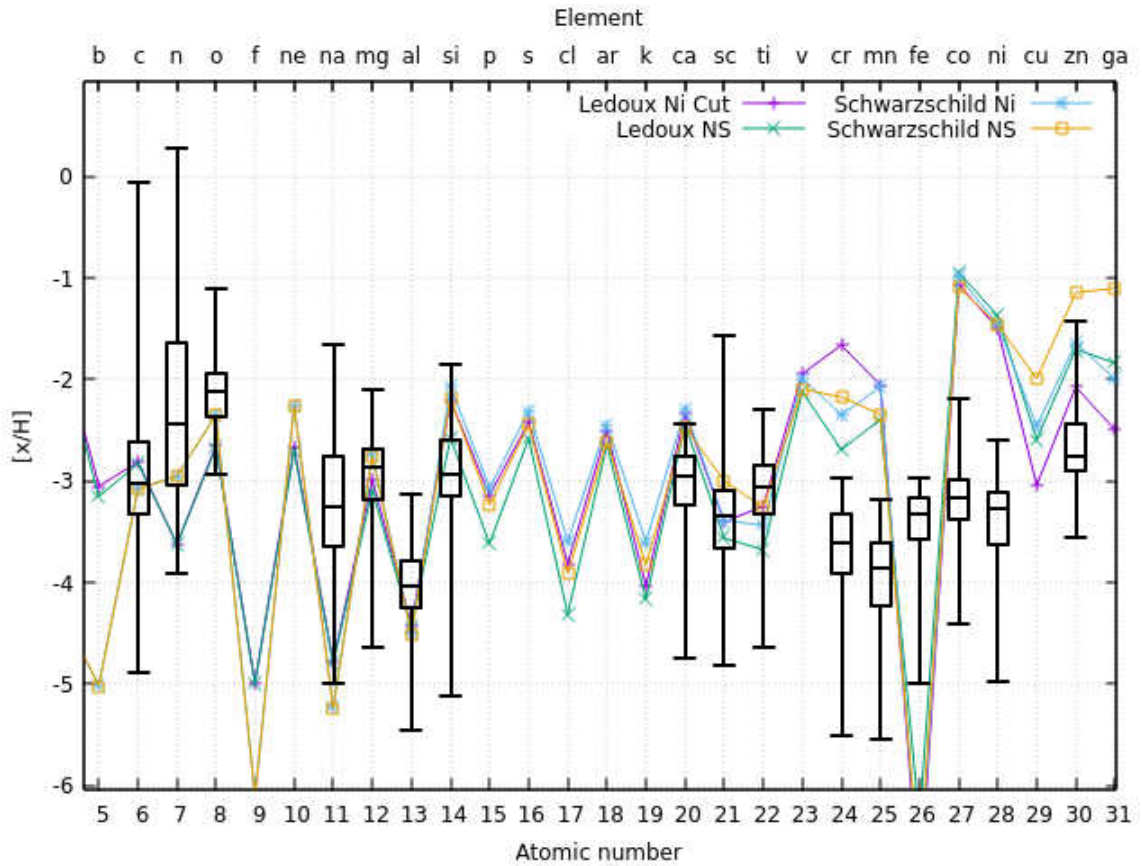
Figure 59. Plotted are the box and whisker plots for the stars as seen in table 9 with the low explosion energy Ledoux and Schwarzschild with the neutron star and nickel mass remnants as discussed in 4.2.4 plotted above with an approximate fitting.
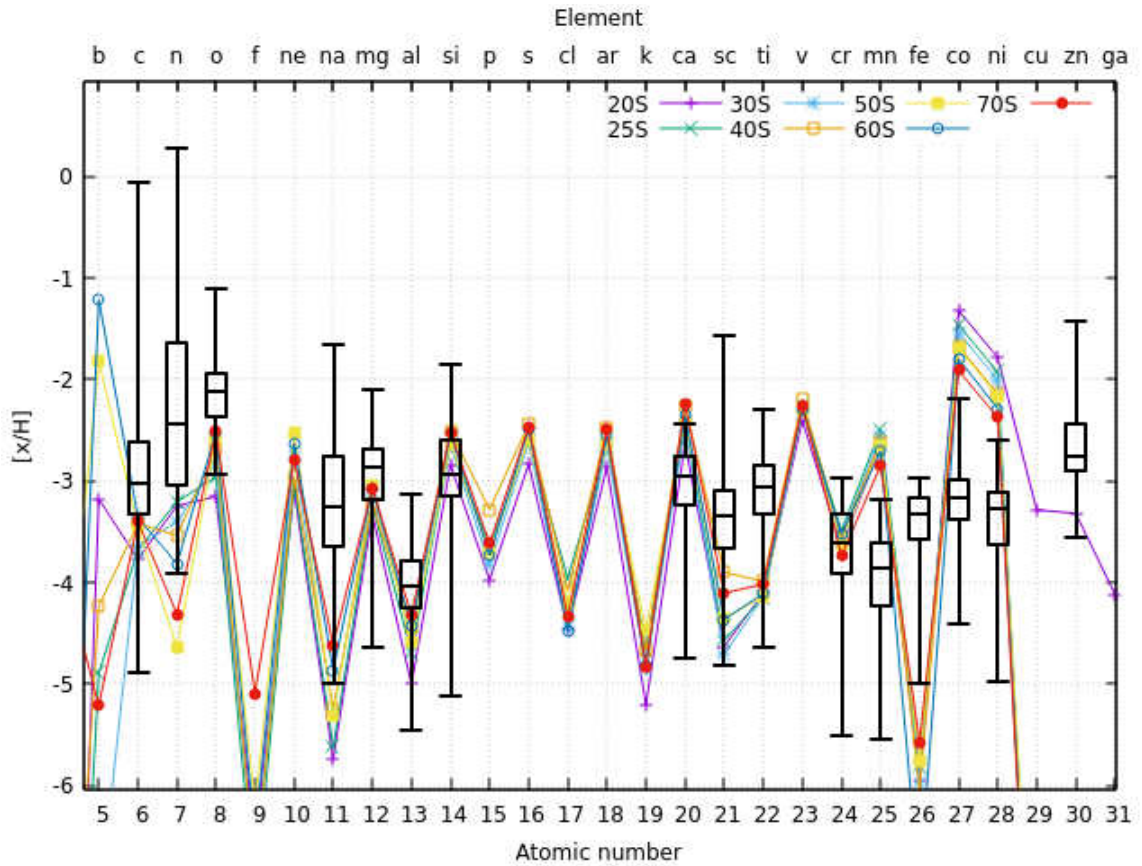
Figure 60. Plotted are the box and whisker plots for the stars as seen in table 9 with the low explosion energy Ledoux and Schwarzschild with the neutron star and nickel mass remnants as discussed in 4.2.4 plotted above with an approximate fitting.
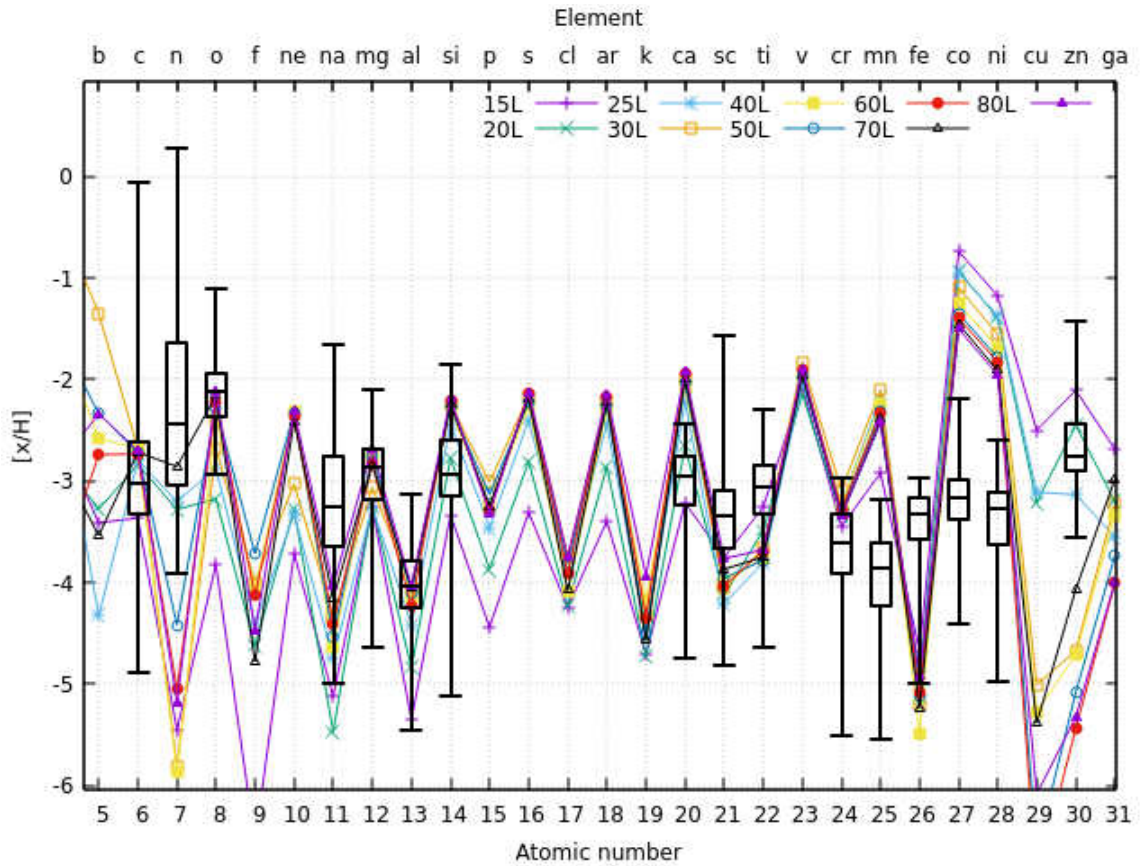
Figure 61. Plotted are the box and whisker plots for the stars as seen in table 9 with the low explosion energy Ledoux and Schwarzschild with the neutron star and nickel mass remnants as discussed in 4.2.4 plotted above with an approximate fitting.

CHAPTER 5

Summary and Conclusions

5.1 Convection Criteria

The use of the Schwarzschild and Ledoux convection criteria produced two unique series

of stellar models that can be thought to represent two end points of stellar evolution; the

large red supergiants resulting from the Schwarzschild criteria and compact blue

supergiants resulting from the Ledoux criteria.

5.1.1 Supernovae and Progenitors

The supernovae generated from the Schwarzschild and Ledoux convection criteria produce

observationally distinct features. This has broader implications beyond that of population

III CCSNe. When observers fit supernovae progenitor stars and stellar evolution models,

they find that the masses determined using their methods suggest an upper limit for red

supergiant progenitors is around 17 $M_\odot$ (Smartt, 2009). Unfortunately, computational

CCSNe are not able to replicate light curves with such low mass, instead requiring masses

closer to 25-30 $M_\odot$. This could imply that the choice of stellar convection could lead to a

progenitor that better matches stellar evolution and the supernova explosion. In the case of

SN1987a, which was later determined to be a blue supergiant, single-component stars, or

stars with the original envelope and core, had difficulty initially matching the data as seen

in table 8. But, an important fact is that convection criteria is a not a free parameter and

should be physically motivated when possible.

There is no definite consensus on the use of convection criteria for stellar evolution (Vanbeveren et al., 2012). Stothers & Chin (1992) have suggested, based on observations of metal poor clusters, that the Ledoux Criteria is likely to be the most accurate. Later, Stothers & Chin (2000), found that the criteria may depend on the mass of the star as they found that the Ledoux criteria could not account for the hydrogen abundances found in hydrogen-poor Wolf-Rayet stars. Newer methods used in the stellar evolution such as removing the mixing-length parameter (Clayton, 1968) which is important for determining the depth of convection, shows some promise. Currently, these newer methods of convection are only implemented for matching solar models. (Pasetto et al., 2014)

Compared to the grid of stellar models published by Heger et al. (2003), the models in this work that have similar M_{ZAMS} often have radii that fit between our two convection criteria models.

5.1.1.1 Observation

In this work, the detection of supernovae in the redshift range of $z = 5 - 15$ favors large radii progenitors using Schwarzschild convection criteria. This is under the set of assumptions that an observation captures the SN early. Recent observations have detected stars and SNe under lensing conditions at a redshift of $z = 1.49$ (Kelly et al., 2015, 2018). While still not nearly as distant as $z = 5$, this gives evidence that capturing these events is a viable method. Goldstein & Nugent (2017) suggest that detections can be be upwards of several a year using high cadence wide field surveys, such as the Large Synoptic Survey Telescope (LSST Science Collaboration et al., 2009) and the Zwicky Transient Factory (Bellm, 2014).

While not high cadence, the deep observations in the infrared offered by the James

Web Space Telescope (Gardner et al., 2006) also contains a spectrometer. While this work does not present synthesized spectra, the presence of spectra can help determine the type of the supernovae. The work here concentrates on the photometric light curves and can give insights to the progenitor star.

5.1.2 Nickel

The high abundances of nickel produced by both the low and high explosion energy series in both Ledoux and Schwarzschild models is a small source of concern. Only SLSNe or pair-instability supernovae are expected to produce such high quantities of nickel during its explosion.

Figure 9 shows the Ledoux series at a low energy wth .07 $M_\odot$ of nickel mixed out to the edge of the helium core. The result of the mixing of nickel and nickel mass amount shows that the secondary peak, powered by nickel, has brightness close to that of the small plateau feature of the Ledoux series. The nickel yields of the high and low explosion energy series are much higher than .07 $M_\odot$ so this high quantity of nickel would likely make a secondary peak much brighter than the earlier light curve peak making the Ledoux supernovae detectable in the range of 20-50 days post shock-breakout. Observation selection effects would lead to measurements of this supernovae to be purely powered by nickel, similar to that of the Type Ia's. The presence of hydrogen would prevent the classification of a Type Ia but would become a peculiar supernovae.

This is not the case for the Schwarzschild series, in which case they are already bright in luminosity and the inclusion of high quantities of nickel would not have the same affect. The plateau phase of the Schwarzschild series are already bright and long in duration and the nickel would only contribute to the post plateau features.

99

5.1.3   Remnants

This work focused on assessing the yields of explosive nucleosyntheis assuming the degenerate iron core as the compact remnant. The mass of this object ranged as seen in table 1. These masses are approximately close to that of the 1.4 $M_\odot$, but not uniform across the masses and criteria. Higher mass remnants are explored by means of a post-processed mass cut through neutron star or nickel mass based cut. These mass cuts were not high, with none being higher then 4 $M_\odot$. This mass cut is smaller then average observed black holes, usually higher then 5 $M_\odot$.

The removal of mass post-hydrodynamics can introduce some issues. As seen in section 4.2.1, the energy in the first zone creates some Fe-peak elements and helium. While this affect is predominately due to the abundance of iron, by removing a higher mass core prior to the hydrodynamics, the energy placed into some silicon or oxygen rich zone could produce higher quantities of nickel or possibly fusing all the way to iron and then go through photodisintegration.

The neutron star and the requirement that only 0.07 $M_\odot$ of nickel is ejected do not produce large remnants and by removing this mass, only removes some of the Fe peak elements and nickel for the low energy. Section 4.2.3 shows that for the high energy, the production of nickel extend into the oxygen core, indicating that the temperature was high enough to fuse oxygen to silicon and then to nickel, reducing the chances of producing other elements in this region. The 0.07 $M_\odot$ ejected nickel mass requirement for the high energy leads to a higher mass remnant, likely the largest of those studied.

When fitting the abundances of the high and low explosion energy series, the yields generated in the Si core were high compared to that in the observed metal poor

stars. As discussed, the silicon core was primarily the source of nickel and cobalt, which were significantly more abundant when compared to observed values. In section 4.4, the explanation for the Fe,Co, and Ni divergences were explained due to the time limit of the calculation not allowing the complete decay of Ni and Co to Fe. But the extra abundance of silicon can be explained in two ways. The first is that the assumed degenerate iron core remnant is too small and the second is that the low explosion energy is not high enough to completely burn the silicon layers. The first produces two outcomes; a higher remnant mass, such as cutting out the silicon core or the inner layers of the oxygen core, would lower the possible Ni yields as well as lower the silicon and other heavier then oxygen abundances. The second is that for a higher explosion energy, there needs to be an energy source which is often linked to the gravitational collapse of the remnant mass. It is likely that the higher explosion energy models already require higher mass remnants, thus reducing the mass of silicon.

5.1.3.1   Energy Source

The usage of a thermal bomb forces a high temperature for a longer time period than that of the incoming and exiting shock, as shown in figure 37. This prolonged exposure completely photodisintegrates the innermost layer for both low and high explosion energy as shown in section 4.2.1. This is primarily due to the instantaneous injection of energy in our method into a single layer. If the likely source of shock formation and revival is neutrino interaction, then it is likely the deposition of energy would be further into the star beyond that of the first zone. The low rate of interaction by neutrinos means the neutrinos likely deposit energy in the first several zones. Numerically, this could be applied by an exponential or Ax^2 type distribution. Having the thermal deposition spread over several

numerical zones, lessens the high temperature photodisintegration effects in the first zone but still results in the same final explosion energy.

5.2   Nucleosynthesis

For both convection criterias, the increase in total explosion energy greatly increase the yields of nickel. High yields of nickel are often thought of as a possible source of super luminous SNe, such as 6 $M_\odot$ of nickel as suggested by the modelling of SN PTF12dam (Baklanov et al., 2015). The modeling requires 32×10^{51} ergs, much higher then our 10 $\times 10^{51}$ergs explosions. In sections 4.2.2 and 4.2.3, the higher explosion energy forms higher nickel masses in both the silicon core and the inner layers of the oxygen core. As shown in section 4.1.1, the oyxgen core grows approximately proportionally with the mass of the model, the silicon core does not increase at the same rate, and stays relatively small.

The low explosion energy Ledoux series averaged in the 2-4 $\times 10^{51}$ ergs, higher than the low explosion energy Scwarzschild series. This average energy could imply that the remnant is undersized if a typical energy for a CCSNe is 1.2×10^{51} ergs. By increasing the size of the central remnant prior to the SNe simulation, two issues come to play. The larger remnant mass would extend into the silicon core or into the oxygen core, lessening the nickel yields. The larger remnant mass implies that the shock has less material to eject so the energy required would be less. The lower energy explosion would give a lower shock temperature, lowering the explosive nucleosynthesis yields. These two causes would likely prevent detectability of these SNe for the low energy series. But if these models are likely to produce high quantities of nickel, then these models may approach the SLSNe luminosity, giving a higher chance of detection.

The yields of the Ledoux series were less affected as the energy changed from the

low and high explosion series. The energy difference was separated by 5-8 $\times 10^{51}$ ergs instead of closer to 9 $\times 10^{51}$ for the Schwarzschild series. This lower difference in energy meant the initial input energy difference was not as large, leading to a similar shock structure. The higher explosion energy Ledoux has a higher abundance of Eu and the elements around it, all strong r-process elements, with a lower abundance in the lighter r-capture elements of Sr, Y and Zr.

The Schwarzschild models do show significant changes as the energy is increased with higher abundances beyond $Z = 42$, with the exclusion of a few elements in which lower explosion series is slightly higher. These abundances are still lower than that of the Ledoux series, but the higher energy explosion series begins to bridge the gap with higher s- and r- process abundances.

5.2.1   IMF

Section 4.3 shows that in general the integrated Ledoux IMF produces higher quantities of heavier elements compared to that of the integrated Schwarzschild IMF's. The high explosion energy Schwarzschild series still does not approach that of the Ledoux series. The 80 $M_\odot$ Schwarzschild model is not included in the Schwarzschild IMF due to the pair instability preventing the formation of the iron core. Its unlikely that the inclusion of this model would increase the yields to match that of the Ledoux IMF's. The individual star yields show that while the yields of the high mass stars are higher in the high energy, this is not a uniform result. For the Ledoux yields, the removal of the 80 $M_\odot$ star from the IMF would likely not change the behavior since the highest yields in the individual Ledoux stars are in the 40 and 70 $M_\odot$ stars.

5.2.2   Observed Metal Poor Stars

Section 4.4 shows that the observed metal poor stars do not follow the trends by either the high or low explosion energy Ledoux or Schwarzschild IMF's. The nickel and Fe peak yields are explainable, but the elements at lower Z do not show a likely convection criteria or explosion energy to assume for Population III CCSNe. The differences in the Schwarzschild and Ledoux become more apparent beyond the Fe-peak however the observed abundances do not extend to that region.

The use of the Salpeter IMF for these population III stars may also contribute to this result. The variety of proposed IMF's for population III stars tends to include stars in the very high mass range of M $> 100 M_\odot$, which is not available for this work. With a larger grid, this region can be explored and a variety of IMF's could be generated to fit these observed values.

Both the core-removed IMF's and the Ni mass cut high explosion energy series for both Ledoux and Schwarzschild fit the observed values. This is explained in section 5.1.3

CHAPTER 6

Future Work

6.1 Stellar Models

Recently, the stellar evolution code MESA has used a new treatment to find the convective boundary during the stellar evolution (Paxton et al., 2018). This implementation allows the identification of the convective boundary to be similar between the Schwarzschild and the Ledoux criterion. In simulations here, the convective boundary was different through out the evolution. In the future, using MESA to evolve the same grid, using as many of the same initial conditions as used in BRAHMA, and using the Woosley & Heger (2007) grid of models gives us three separate sources of Population III stars. Generating the CCSNe and nucleosynthesis of the new grids, we can use these new data as an extra degree of freedom when fitting the IMF integrated yields to that of observable extremely metal poor stars.

In addition, the grid of models used for this work was coarse with only nine models per convection criteria from 15-80 $M_\odot$. Expanding this to a wide grid of 8-120 $M_\odot$ with an incremental ΔM of 0.2 to 5 $M_\odot$ would allow a much finer integration and a deeper investigation of possible Population III CCSNe. This also allows us to explore the compactness parameter discussed in section 4.1.3 in a much finer detail.

Other considerations would be the implementation of rotation in the evolution or the addition of a stellar binary component (Saigo et al., 2004). These binary systems could through interaction, expel the hydrogen envelope, leading towards Type Ib or Ic

supernovae. In the case of our Schwarzschild models, the extended envelope could easily

fill the Roche lobe of a nearby companion star. If the material does not completely eject

and instead forms a disk like feature, the interaction of the SNe with this disk may be

complex , but depending on viewing angle, could lead to a multiple classifications or an

inherently brighter event. (McDowell et al., 2018). With mass loss being dependent on

metallicity, the only way a population III SNe could be a hydrogen free or helium free

SNe would be through interaction or violent outburst, but this is only likely for extremely

high mass progenitors (Marigo, P. et al., 2003).

6.2   Supernovae

As discussed in Chapter 1.2, the simulation of CCSNe can be done in multiple

dimensions, time scales, length scales, and by using other physics, such as relativistic

affects or radiative transfer. Usually, the 3-D simulations are used when the study is

focused on effects such as turbulent mixing or non-symmetric physics, such as jet driven

CCSNe or magnetic fields. Due to the time and computational resources required, using a

3-D code to track the nucleosynthesis, which is not computed for the full 400 days is often

not viable, especially considering a 3000 isotope calculation. If we consider the

Schwarzschild models, which do not have significant yields above $Z = 40$, a fully 3-D

calculation might be viable with less isotopes.

6.2.1   Hydrodynamic Fallback

As suggested by Heger et al. (2003) and Sukhbold et al. (2016), the central remnant is

likely to be dependent on the mass of the progenitor star. The primary method of having

only a degenerate iron core mass as the central remnant might be under measuring the

mass and therefor over representing the material ejected during the supernovae. The hydrodynamical method of fallback is currently not implementable in BOOM. The basic method, as described by Woosley et al. (2002), allows the first hydrodynamic zone to fall inward towards a specified radius, approximately 500 km, in a specified time. At this point, the velocity is then reversed and increased rapidly towards a chosen velocity, defined to give a specific final energy. After another period of time before coasting to a stop at another final radii, where this new location is locked in place and given a velocity of $v_1 = 0 cm/s$. So as material falls back to this layer, it can be removed from the hydrodynamic grid, leading to the growth of the central remnant. Future work would implement this into BOOM.

6.2.2   Explosion Mechanism

As described above, this fallback method also employs the use of the 'piston' as an explosion mechanism. In the thermal bomb, the temperature and energy of that first zone increases rapidly as the material compresses outward compared to the flat thermal structure shown in figure 37. This could affect the yields produced in this zone, but should be investigated.

Other sources could be the inclusion of a rapidly spinning neutron star (Kasen & Bildsten, 2010) and the energy radiated from this as an addition energy source. This time dependent source radiates energy as it spins down from its rapid formation. This additional time dependent energy source would reduce the initial temperature raised in the thermal bomb method.

A time-dependent thermal bomb could also be used as a more realistic explosion mechanism.

6.2.3 Pair-Instability Supernovae

In chapter 3, the 80 $M_\odot$ Schwarzschild model was not used due to the formation of pair-production, or the production of a particle and its anti-particle in the silicon core. This is an interesting result as its thought that Pair-instability supernovae are the results of massive stars with masses of 150 $M_\odot$ to 250 $M_\odot$, shown in figure 6. While it is thought that at around 100 $M_\odot$ the pair-production can start, it may not strong enough to produce a pair-instable supernova. If these are possible to explode at in the 80-100 $M_\odot$ mass range, these types of supernovae have very high energy shocks, producing high quantities nickel, and likely produce a high amount of r-process elements as the extremely hot shock traverses the large oxygen core. In the yields shown in chapter 3, the Schwarzschild yields were lower beyond the Fe-peak compared to that in the Ledoux series. Having a set of possibly pair-instable high explosion energy supernovae would give value to the split IMF idea in which theres a non-Salpter IMF distribution.

6.3   Nucleosynthesis

The nucleosynthesis calculations were post-processed with a fixed number of isotopes. Recent work, such as that done by Sukhbold et al. (2016), uses an adaptive grid of isotopes with the hydrodynamics to calculate the nucleosynthesis. This lessens the computational cost of the full model, especially in zones or regions unlikely to reach temperatures, densities, or have the needed free neutrons to produce heavy, or high Z, elements. Linking the hydrodynamics to the nuclear reactions allows the absorption and release of energy during the full execution of the hydrodynamics, which could give more accurate results to the net yields.

6.3.1   IMF's

As cited in section 4.3, there exists a wide variety of cosmological scale hydrodynamic simulations that produce a mixture of population III IMF's. (Bromm, 2013; Cooke & Madau, 2014; Greif et al., 2011; Frebel & Norris, 2015)

6.3.2   IMF from Yields

In section 4.3, model yields were integrated with the Salpeter IMF and used to compare to the observed abundances in extremely metal poor stars. Ishigaki et al. (2018) fitted observed abundances with individual model yields and from the grid of fits and produced a model population III IMF as shown in figure 62.
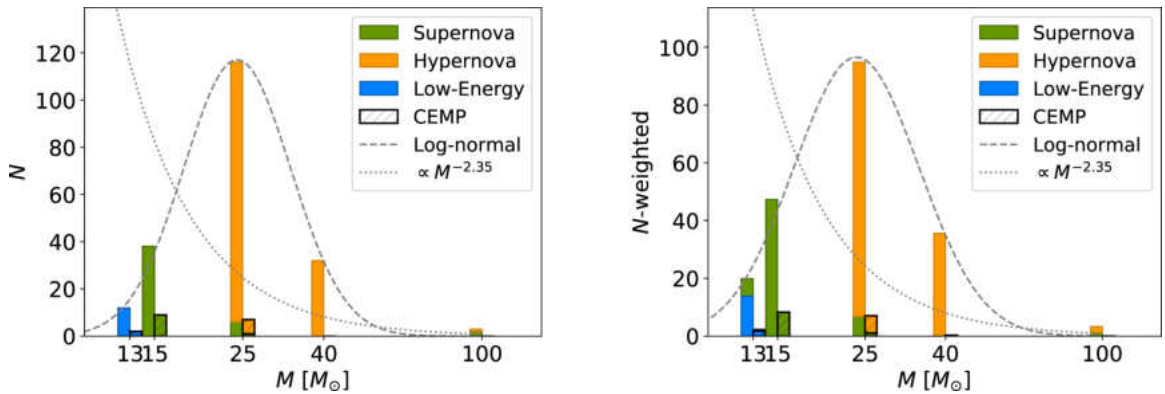

Figure 62. Reproduced from Ishigaki et al. (2018) shows two fitted IMFs in their work using only the shown set of models.

This method requires a high number of observed abundances from extremely metal poor stars. The approximation that these stars are enriched from one or two generations of stars may or may not be likely, so including other sources, such as Type Ia, might significantly change the integrated IMF's.

6.3.3   IMF Evolution

A unique analysis is using the yields and assume some initial IMF, find an average

metallicity from the IMF integrated yields, and then use this metallicity, or some fraction,

to generate a second generation of stars. With this second generation of stars, re-run the

SNe and nucleosynthesis to generate a second set of yields and repeat. It is assumed that

there are three primary populations of stars (Carroll & Ostlie, 2007), but this may not

equate to exactly three generations of stars. The purpose of this idea would be to build

successive generations of stars until 'current' or 'solar' values are reached. This would be

a first approximation as there are significant factors not taken into account, such as

neutron star mergers, Type Ia, or galaxy type.

6.3.4   n-capture Elements

The lighter n-capture elements such as Sr, Y, and Zr, are often studied by nucleosynthesis

groups (Burris et al., 2009). These elements when compared over a wide range of

metallicities show that at low metallicity, behave similar to that of r-process neutron

capture. As the metallicity increases, the elements behave more similar to that of the

s-process elements. In future work, if the grid of models is refined as discussed in section

6.1, then there would be a high range of extremely metal poor models to determine which

model or models are responsible for observed yields. As shown, the yields are dependent

on the explosion energy, the mass of the star, and the convection criteria. A fine grid of

models with both criteria would produce a more refined analysis to explain the observed

abundances.

BIBLIOGRAPHY

Anders, E., & Grevesse, N. 1989, Geochimica Cosmochimica Acta, 53, 197

Arnett, D. 1996, Supernovae and Nucleosynthesis: An Investigation of the History of Matter from the Big Bang to the Present

Arnett, W. D. 1980, Astrophysics Journal, 237, 541

Arnett, W. D., Bahcall, J. N., Kirshner, R. P., & Woosley, S. E. 1989, Annual Review of Astronomy and Astrophysics, 27, 629

Arnett, W. D., & Fu, A. 1989, Astrophysics Journal, 340, 396

Asplund, M., Grevesse, N., Sauval, A. J., & Scott, P. 2009, Atomic Data and Nuclear Data Tables, 47, 481

Baklanov, P. V., Sorokina, E. I., & Blinnikov, S. I. 2015, Astronomy Letters, 41, 95

Bellm, E. 2014, in The Third Hot-wiring the Transient Universe Workshop, ed. P. R. Wozniak, M. J. Graham, A. A. Mahabal, & R. Seaman, 27–33

Bessell, M. S., Collet, R., Keller, S. C., et al. 2015, Astrophysical Journal Letters, 806, L16

Blinnikov, S., Lundqvist, P., Bartunov, O., Nomoto, K., & Iwamoto, K. 2000, Astrophysics Journal, 532, 1132

Bromm, V. 2013, Reports on Progress in Physics, 76, 112901

Burris, D., Lusk, J., & Jones, E. M. 2009, Publications of the Astronomical Society of the Pacific, 121, 111

Burrows, A. 2013, Rev. Mod. Phys., 85, 245

Burrows, A., Vartanyan, D., Dolence, J. C., Skinner, M. A., & Radice, D. 2018, Space Science Reviews, 214, 33

Caramana, E., Shashkov, M., & Whalen, P. 1998, Journal of Computational Physics, 144, 70

Carroll, B. W., & Ostlie, D. A. 2007, An Introduction to Modern Astrophysics, 2nd edn., ed. S. F. P. Addison-Wesley

Catchpole, R. M., Menzies, J. W., Monk, A. S., et al. 1987, Monthly Notices of the Royal Astronomical Society, 229, 15P

Chatzopoulos, E., Wheeler, J. C., & Vinko, J. 2012, Astrophysics Journal, 746, 121

Chen, K.-J., Heger, A., Whalen, D. J., et al. 2017, Monthly Notices of the Royal Astronomical Society, 467, 4731

Chiaki, G., Schneider, R., Nozawa, T., et al. 2014, Monthly Notices of the Royal Astronomical Society, 439, 3121

Chruslinska, M., Belczynski, K., Klencki, J., & Benacquista, M. 2018, Monthly Notices of the Royal Astronomical Society, 474, 2937

Ciardi, B., Ferrara, A., & Abel, T. 2000, The Astrophysical Journal, 533, 594

Clayton, D. 1968, Principles of stellar evolution and nucleosynthesis: with a new preface (University of Chicago Press)

Cohen, J. G., Christlieb, N., Thompson, I., et al. 2013, Astrophysics Journal, 778, 56

Cooke, R. J., & Madau, P. 2014, Astrophysical Journal, 791, 116

Couch, S. M., & O'Connor, E. P. 2014, The Astrophysical Journal, 785, 123

Deng, L.-C., & Xiong, D.-R. 2001, Chinese Journal of Astronomy and Astrophysics, 1, 50

Dessart, Luc, & Audit, Edouard. 2018, A&A, 613, A5

Eggleton, P. P. 1971, Monthly Notices of the Royal Astronomical Society, 151, 351

Faran, T., Nakar, E., & Poznanski, D. 2018, Monthly Notices of the Royal Astronomical Society, 473, 513

Ferguson, J. W., Alexander, D. R., Allard, F., et al. 2005, Astrophysics Journal, 623, 585

Ferrara, A. 1998, The Astrophysical Journal Letters, 499, L17

Filippenko, A. V. 1997, Annual Review of Astronomy and Astrophysics, 35, 309

Frebel, A., Chiti, A., Ji, A. P., Jacobson, H. R., & Placco, V. M. 2015, Astrophysics Journal Letters, 810, L27

Frebel, A., & Norris, J. E. 2015, Astronomy and Astrophysics, 53, 631

Gaia Collaboration, Prusti, T., de Bruijne, J. H. J., et al. 2016, A&A, 595, A1

Gardner, J. P., Mather, J. C., Clampin, M., et al. 2006, Space Science Reviews, 123, 485

Garmany, C. D. 1998, in Astronomical Society of the Pacific Conference Series, Vol. 148, Origins, ed. C. E. Woodward, J. M. Shull, & H. A. Thronson, Jr., 184

Goldstein, D. A., & Nugent, P. E. 2017, The Astrophysical Journal Letters, 834, L5

Greif, T. H., Springel, V., White, S. D. M., et al. 2011, Astrophysical Journal, 737, 75

Hansen, T., Hansen, C. J., Christlieb, N., et al. 2014, Astrophysics Journal, 787, 162

Harwit, M., & Spaans, M. 2003, The Astrophysical Journal, 589, 53

Heger, A., Fryer, C. L., Woosley, S. E., Langer, N., & Hartmann, D. H. 2003, The Astrophysical Journal, 591, 288

Heger, A., Fryer, C. L., Woosley, S. E., Langer, N., & Hartmann, D. H. 2003, Astrophysics Journal, 591, 288

Hopkins, P. F., & Conroy, C. 2017, The Astrophysical Journal, 835, 154

Hubber, D. A., Walch, S., & Whitworth, A. P. 2013, Monthly Notices of the Royal Astronomical Society, 430, 3261

Hughes, J. P., Rafelski, M., Warren, J. S., et al. 2006, The Astrophysical Journal Letters, 645, L117

Iglesias, C. A., & Rogers, F. J. 1996, The Astrophysical Journal, 464, 943

Ishigaki, M. N., Tominaga, N., Kobayashi, C., & Nomoto, K. 2018, The Astrophysical Journal, 857, 46

Ishimaru, Y., & Wanajo, S. 1999, The Astrophysical Journal Letters, 511, L33

Jacobson, H. R., Keller, S., Frebel, A., et al. 2015, Astrophysics Journal, 807, 171

Janka, H.-T. 2017, Neutrino Emission from Supernovae (Cham: Springer International Publishing), 1575–1604

Janka, H.-Th. 2001, A&A, 368, 527

Kasen, D., & Bildsten, L. 2010, Astrophysics Journal, 717, 245

Kasen, D., & Woosley, S. E. 2009, The Astrophysical Journal, 703, 2205

Kashiwa, B., & Lee, W. H. 1991, in Advances in the Free-Lagrange Method Including Contributions on Adaptive Gridding and the Smooth Particle Hydrodynamics Method, ed. H. E. Trease, M. F. Fritts, & W. P. Crowley (Berlin, Heidelberg: Springer Berlin Heidelberg), 277–288

Kelly, P. L., Rodney, S. A., Treu, T., et al. 2015, Science, 347, 1123

Kelly, P. L., Diego, J. M., Rodney, S., et al. 2018, Nature Astronomy, 2, 334

Kim, A., Goobar, A., & Perlmutter, S. 1996, Publications of the Astronomical Society of the Pacific, 108, 190

Lattimer, J. M. 2012, Annual Review of Nuclear and Particle Science, 62, 485

Lawlor, T. M., & MacDonald, J. 2006, Monthly Notices of the Royal Astronomical Society, 371, 263

Lawlor, T. M., Young, T. R., Teffs, J., & MacDonald, J. 2015, Monthly Notices of the Royal Astronomical Society, 450, 1618

LSST Science Collaboration, Abell, P. A., Allison, J., et al. 2009, ArXiv e-prints, arXiv:0912.0201

Mannucci, F., & Cresci, G. 2012, Memorie della Societa Astronomica Italiana Supplementi, 19, 214

Marigo, P., Chiosi, C., & Kudritzki, R.-P. 2003, A&A, 399, 617

McDowell, A. T., Duffell, P. C., & Kasen, D. 2018, The Astrophysical Journal, 856, 29

Meléndez, J., Placco, V. M., Tucci-Maia, M., et al. 2016, Astronomy and Astrophysics, 585, L5

Messer, O. E. B., Mezzacappa, A., Bruenn, S. W., & Guidry, M. W. 1998, The Astrophysical Journal, 507, 353

Mezzacappa, A., & Messer, O. 1999, Journal of Computational and Applied Mathematics, 109, 281

Mihalas, D. 1978, Stellar Atmospheres, Astronomy and Astrophysics Series (W. H. Freeman)

Mihalas, D., & Mihalas, B. W. 1984, Foundations of radiation hydrodynamics

Morozova, V., Piro, A. L., Renzo, M., et al. 2015, Astrophysics Journal, 814, 63

Mller, T., Prieto, J. L., Pejcha, O., & Clocchiatti, A. 2017, The Astrophysical Journal, 841, 127

Nadyozhin, D. K. 2003, Monthly Notice of the Royal Astronomical Society, 346, 97

Nagy, A. P., Ordasi, A., Vinkó, J., & Wheeler, J. C. 2014, Astronomy and Astrophysics, 571, A77

Nagy, A. P., & Vinkó, J. 2016, Astronomy and Astrophysics, 589, A53

Nakamura, F., & Umemura, M. 2001, The Astrophysical Journal, 548, 19

Nicholl, M., Smartt, S. J., Jerkstrand, A., et al. 2014, Monthly Notices of the Royal Astronomical Society, 444, 2096

Norman, M. L. 2008, AIP Conference Proceedings, 990, 3

O'Connor, E., & Ott, C. D. 2011, The Astrophysical Journal, 730, 70

Ohkubo, T., Nomoto, K., Umeda, H., Yoshida, N., & Tsuruta, S. 2009, The Astrophysical Journal, 706, 1184

Omukai, K., Tsuribe, T., Schneider, R., & Ferrara, A. 2005, Astrophysical Journal, 626, 627

Pasetto, S., Chiosi, C., Cropper, M., & Grebel, E. K. 2014, Monthly Notices of the Royal Astronomical Society, 445, 3592

Paxton, B., Bildsten, L., Dotter, A., et al. 2011, Astrophysical Journal Supplment, 192, 3

Paxton, B., Schwab, J., Bauer, E. B., et al. 2018, The Astrophysical Journal Supplement Series, 234, 34

Phillips, M. M., Heathcote, S. R., Hamuy, M., & Navarrete, M. 1988, Astrophysical Journal, 95, 1087

Placco, V. M., Frebel, A., Lee, Y. S., et al. 2015, Astrophysical Journal, 809, 136

Placco, V. M., Frebel, A., Beers, T. C., et al. 2016, Astrophysics Journal, 833, 21

Press, W. H., Teukolsky, S. A., Vetterling, W. T., & Flannery, B. P. 1993, Numerical Recipes in FORTRAN; The Art of Scientific Computing, 2nd edn. (New York, NY, USA: Cambridge University Press)

Pretorius, F., & Lehner, L. 2004, Journal of Computational Physics, 198, 10

Radice, D., Abdikamalov, E., Ott, C. D., et al. 2018, Journal of Physics G: Nuclear and Particle Physics, 45, 053003

Roederer, I. U., Kratz, K.-L., Frebel, A., et al. 2009, The Astrophysical Journal, 698, 1963

Roederer, I. U., Preston, G. W., Thompson, I. B., et al. 2014, Astronomical Journal, 147, 136

Roy, R. 2013, in Astronomical Society of India Conference Series, Vol. 8, Astronomical Society of India Conference Series, ed. S. Das, A. Nandi, & I. Chattopadhyay, 135–138

Saigo, K., Matsumoto, T., & Umemura, M. 2004, The Astrophysical Journal Letters, 615, L65

Salpeter, E. E. 1955, Astrophysical Journal, 121, 161

Schneider, R., Ferrara, A., Salvaterra, R., Omukai, K., & Bromm, V. 2003, Nature, 422, 869

Shigeyama, T., & Nomoto, K. 1990, Astrophysical Journal, 360, 242

Smartt, S. J. 2009, Astronomy and Astrophysics Annals, 47, 63

Smith, M. S., & Rehm, K. E. 2001, Annual Review of Nuclear and Particle Science, 51, 91

Stacy, A., & Bromm, V. 2014, The Astrophysical Journal, 785, 73

Stacy, A., Bromm, V., & Lee, A. T. 2016, Monthly Notices of the Royal Astronomical Society, 462, 1307

Stothers, R. 1977, Isis, 68, 443

Stothers, R. B., & Chin, C.-W. 1992, Astrophysics Journal Letters, 390, L33

Stothers, R. B., & Chin, C.-W. 2000, Astrophys. J., 540, 1041

Sukhbold, T., Ertl, T., Woosley, S. E., Brown, J. M., & Janka, H.-T. 2016, The Astrophysical Journal, 821, 38

Sutherland, P. G., & Wheeler, J. C. 1984, The Astrophysics Journal, 280, 282

Thielemann, F.-K., Eichler, M., Panov, I., & Wehmeyer, B. 2017, Annual Review of Nuclear and Particle Science, 67, 253

Timmes, F. X. 1999, The Astrophysical Journal Supplement Series, 124, 241

Timmes, F. X., Hoffman, R. D., & Woosley, S. E. 2000, The Astrophysical Journal Supplement Series, 129, 377

Tominaga, N., Umeda, H., & Nomoto, K. 2007, The Astrophysical Journal, 660, 516

Vanbeveren, D., van Rensbergen, W., & de Loore, C. 2012, Evolution of Massive Stars: A Confrontation between Theory and Observation (Springer Netherlands)

Viallet, M., Baraffe, I., & Walder, R. 2011, A&A, 531, A86

von Steinkirch, M. 2012

Weaver, T. A., Zimmerman, G. B., & Woosley, S. E. 2017, KEPLER: General purpose 1D multizone hydrodynamics code, Astrophysics Source Code Library, ascl:1702.007

Wiktorowicz, G., Belczynski, K., & Maccarone, T. 2014, in Binary Systems, their Evolution and Environments, 37

Woosley, S. E., Arnett, W. D., & Clayton, D. D. 1973, Astrophysical Journal, 26, 231

Woosley, S. E., & Heger, A. 2007, Physics Reports, 442, 269

Woosley, S. E., Heger, A., & Weaver, T. A. 2002, Reviews of Modern Physics, 74, 1015

Woosley, S. E., Heger, A., Weaver, T. A., & Langer, N. 1997, ArXiv Astrophysics e-prints, astro-ph/9705146

Woosley, S. E., Pinto, P. A., & Ensman, L. 1988, Astrophysical Journal, 324, 466

Yong, D., Norris, J. E., Bessell, M. S., et al. 2013, Astrophysical Journal, 762, 26

Young, T. R. 2004, Astrophysical Journal, 617, 1233

Zel'dovich, I., & Raizer, Y. 2002, Physics of Shock Waves and High-Temperature Hydrodynamic Phenomena, Dover Books on Physics (Dover Publications)

Zhang, Y., & Zhao, Y. 2015, Data Science Journal, 14, 11